

DISSERTATION

Extremely short light pulses: generation, diagnostics,
and application in attosecond spectroscopy

ausgeführt zum Zwecke der Erlangung des akademischen Grades
eines Doktors der technischen Wissenschaften unter der Leitung

von

Univ. Doz. Dr. Armin Scrinzi

387

Institut für Photonik

eingereicht an der Technischen Universität Wien
Fakultät für Elektrotechnik und Informationstechnik

von

Dipl. Ing. Vladislav S. Yakovlev

0126161

Gußhausstrasse 27/387, 1040 Wien

Wien, im Juni 2003

Extrem kurze Lichtimpulse: Erzeugung, Diagnostik und Anwendung in der Attosekunden-Spektroskopie

– Kurzfassung –

Diese Dissertation befasst sich mit dem Design gechirpter Spiegel, mit der Erzeugung hoher Harmonischer und mit dem Auger Zerfall in Gegenwart äußerer Felder. Allen drei Punkten gemeinsam sind der Gebrauch ultrakurzer Lichtpulse und physikalische Prozesse, die auf der femtosekunden Zeitskala stattfinden. Die wichtigste Ergebnisse der Arbeit sind folgende:

- Es wurde gezeigt, dass effiziente globale Optimierung gechirpter Spiegel mit einer adaptierten Version des memetischen Algorithmus möglich ist (der Algorithmus ist auch als “hybrid genetic algorithm” bekannt).
- Das elektrische Feld ultrakurzer Lichtpulse im Nahbereich der Spitze der Einhüllende kann mittels einer Analyse von hohen harmonischen Strahlungsspektren rekonstruiert werden.
- Eine Quantentheorie der zeitaufgelösten Auger Spektroskopie wurde entwickelt. Anhand der Methode der “essential states” wurden Ausdrücke für die Wahrscheinlichkeitsamplituden in geschlossener analytischer Form hergeleitet. Die Theorie bildet die Grundlage für die Interpretation von Experimenten, die die Bewegung von Elektronen während Anregung, Abregung und Ionisation von Atomen untersuchen.

Contents

Introduction	5
1 Novel techniques for the optimisation of chirped mirrors	8
1.1 An advanced global optimisation algorithm	12
1.1.1 Challenges	12
1.1.2 The memetic algorithm and the optimisation of multilayer interference coatings	14
1.1.3 Advantages of the memetic algorithm	17
1.2 Extremely broadband chirped mirrors	21
1.2.1 A merit function based on simulation of pulse reflection .	24
1.3 Sensitivity to perturbations of layer thicknesses	28
1.3.1 Stochastic quasigradient algorithm	33
2 High harmonic imaging of few-cycle laser pulses	38
2.1 Simulation of generation and propagation of high-order harmonics	40
2.1.1 The recollision model of high-harmonic generation	41
2.1.2 Photon energies	44
2.1.3 Simulated harmonic spectra	47
2.1.4 Time-frequency analysis	50
2.2 Advanced analysis of high-harmonic spectra	52
2.2.1 High-harmonic imaging of chirped laser pulses	56
2.2.2 Applicability of the method	59

3	Quantum theory of time-resolved Auger measurement	61
3.1	Time-resolved measurement of Auger decay in krypton	62
3.2	Derivation of basic equations	64
3.2.1	Essential states method	64
3.2.2	Equations for the probability amplitudes c_h and c_f	67
3.2.3	An analytical expression for c_h	72
3.2.4	Analytical expressions for c_f	73
3.3	Numerical simulations	76
3.3.1	The matrix elements	77
3.3.2	Solution of the integro-differential equation for c_h	80
3.3.3	Solution of the differential equation for c_h	82
3.3.4	Auger spectra	84
	Conclusions	88
A.1	The transfer matrix formalism	90
A.2	Numerical solution of the pulse propagation equations	91
A.3	Optimal focusing of the laser beam for high-harmonic imaging	96
A.4	Integration of rapidly oscillating functions	98
	Acknowledgements	110

Introduction

Since the invention of the laser a lot of scientific effort was put into the generation of shorter and shorter light pulses. Nowadays state-of-the art mode-locked lasers can produce pulses as short as a few femtoseconds. These ultrashort pulses have found a wide range of applications in fundamental science as well as in industry: they are used to study ultrafast processes in semiconductors, to trace and control chemical reactions, to explore light-matter interactions at very high intensity levels, as well as for precision processing of materials, for precise frequency measurements, and even for early diagnosis and treatment of eye diseases.

Although the duration of pulses emitted from an oscillator can be decreased by external compression, the pulses cannot be made shorter than one optical cycle, which is approximately three femtoseconds for a Ti:sapphire oscillator, for which the centre of the luminescence region lies at 800 nanometres. Breaking the limit of 1-fs duration requires shorter-wavelength radiation. At the present time we know two approaches to generation of sub-femtosecond pulses: stimulated Raman scattering [1] and high-order harmonic generation [2, 3]. Both methods were intensively studied theoretically and experimentally, but so far generation of isolated sub-femtosecond pulses was only demonstrated by using the high-harmonic generation process [4]. In these experiments soft X-ray pulses shorter than one femtosecond were obtained by irradiating neon atoms with intense few-femtosecond laser pulses. The duration of the sub-femtosecond X-ray pulses reached thus the time scale of electronic processes in atoms, making for the first time attosecond¹ spectroscopy possible.

¹1 attosecond = 10^{-18} seconds

In my thesis I cover important aspects of the generation of few-cycle laser pulses, diagnostics of their electric field, and their application in attosecond spectroscopy. The first chapter of my thesis reports on my contribution to the technology of few-cycle laser pulse generation by the design of “chirped mirrors”. Since the invention of the Kerr-lens mode-locking in Ti:sapphire the main obstacle to approaching the theoretical limit of pulse duration remains the necessity of accurate dispersion control over a broad wavelength range. An indispensable tool for this purpose is provided by chirped mirrors: multilayer dielectric mirrors, where the thickness of each layer is carefully chosen so that the whole system has special dispersion properties. Design of chirped mirrors relies on computer optimisation of layer thicknesses. In my work I developed new optimisation algorithms specially adapted for dispersive multilayer coatings. The achievements I have made in this direction significantly facilitate design of high-quality chirped mirrors, especially if an extremely broad bandwidth is required.

The second chapter is concerned with the diagnostics of few-cycle pulses. Different from longer laser pulses, a complete characterisation of few-cycle pulses requires the determination of the so-called carrier-envelope phase of the laser pulse in addition to pulse envelope and chirp. High harmonic radiation generated the pulse passes through a gas volume can be used to determine his parameter.

Finally, the third chapter of my thesis is devoted to the theoretical analysis of a first application of few-cycle pulses and high-harmonic generation in sub-femtosecond time-resolved spectroscopy. The investigations were triggered by the first experimental demonstration of feasibility of time-resolved spectroscopy with an attosecond resolution [A2]. In this experiment Drescher *et. al.* performed a pump-probe observation of the Auger decay in krypton, where the pump pulse was a sub-femtosecond extreme-ultraviolet pulse, and the probe pulse was a few-cycle laser pulse. In this experiment the energy distribution of Auger electrons was measured in dependence on the delay between the two pulses. In order to fully interpret these measurements, a detailed theory of the Auger decay dressed by laser field is necessary, which didn't exist at the moment, when the experiment was

done. Development of a quantum-mechanical description of the process started immediately after the experimental breakthrough, and the results of this work are presented in the last chapter of my thesis.

Chapter 1

Novel techniques for the optimisation of chirped mirrors

Dispersive dielectric multilayer mirrors [5] [henceforth chirped mirrors (CMs)] have contributed significantly to enhancement of the performance, compactness and reliability of femtosecond laser sources. The generation of sub-10-fs pulses directly from oscillators requires accurate, broadband, higher-order dispersion control [6], which can now be achieved routinely with CM dispersion-controlled oscillators. Progress in CM-design and manufacturing in conjunction with advanced oscillator architectures has permitted the direct generation of sub-6-fs pulses [7, 8, 9]. Novel spectral broadening techniques [10, 11, 12] allow spectra to be produced that can extend over more than one optical octave¹; subsequent compression with CMs led to pulses shorter than 5 fs [10, 13, 14, 15].

The underlying physical principle of CMs is the same as in all other kinds of interference optical coatings: interference of light waves reflected from different plane-parallel interfaces results in a certain frequency-dependent reflectance $R(\lambda)$ and phase shift $\varphi(\lambda)$ of the incident light, where $\varphi(\lambda)$ is directly connected to the

¹one octave is a frequency range, where the biggest frequency is two times larger than the lowest one

group delay (GD) and the group-delay dispersion (GDD) introduced by the mirror:

$$\text{GD}(\omega) = -\phi'(\omega), \text{ and} \quad (1.1)$$

$$\text{GDD}(\omega) = -\phi''(\omega). \quad (1.2)$$

The same principle works, for example, in a Bragg reflector: a stack of layers with a fixed optical thickness equal to $\lambda_0/4$ that has a high reflectance for wavelengths close to λ_0 . However, CMs possess another very important property: they can be designed in such a way that the frequency-dependent phase shift $\phi(\lambda)$ matches dispersion properties of materials common in laser systems (e.g. fused silica or Ti:sapphire), which is essential for the generation of ultrashort pulses. This property can be explained by the frequency-dependent penetration depth: although each frequency component is partially reflected from each boundary between two layers with different refractive indexes, in CMs a certain penetration depth is associated with every frequency component, at which most of reflection takes place. In the first approximation the frequency-dependent group delay is twice the time of light propagation from the front interface to the penetration depth of the corresponding frequency component (Fig. 1.1). Thus, a desirable dispersion can be achieved if optical layer thicknesses gradually change along the coating, so that a component with wavelength λ is reflected from the part of the stack, where the optical thickness of layers is close to $\lambda/4$. This gradual change of optical layer thicknesses is referred to as “chirping”, hence the name “chirped mirrors”. Unfortunately, simple chirping of layer thicknesses is not sufficient to obtain CMs with satisfactory dispersion characteristics: Reflections other than the ones at the expected penetration depths lead to parasitic interferences, which cause large GDD oscillations [5]. Computer optimisation was recognised as an indispensable tool for tuning layer thicknesses of CMs.

The first CM designs were obtained by computer optimisation of “chirped” Bragg reflectors. Ref. [5] reports a design consisting of 42 alternating layers of SiO_2 and TiO_2 , which had a bandwidth of 200 nm at the central wavelength of 800 nm. Several predesign methods were proposed for the calculation of start-

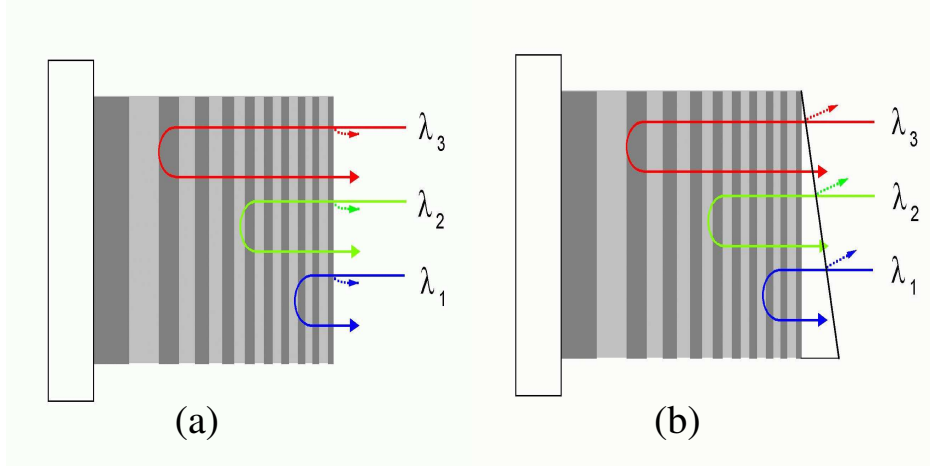


Figure 1.1: Schematic representation of a standard CM **(a)** and of a TFI CM **(b)**. In order to achieve negative GDD upon reflection, the inequality $\lambda_1 < \lambda_2 < \lambda_3$ must be fulfilled. Rays reflected at the front interface (represented by dots) can interfere with rays reflected within the multilayer (full lines) giving rise to GDD oscillations in the case of the standard CM. The wedge attached to the TFI mirror prevents this effect.

ing structures that, after limited computer optimisation, converged to designs with enhanced performance [16, 17, 18, 19]. Of particular interest are the so-called “double-chirped” mirrors [16, 20, 21]: an analytical approach based on the coupled-mode theory for multilayer interference coatings [22]. In this approach a chirped mirror is composed of Bragg cells, where each cell is characterised by a corresponding Bragg wavelength and the thickness of the high-refractive-index layer. Both these parameters are chirped in order to achieve a smooth increase of the coupling coefficient, which was recognised as a prerequisite for suppression of GDD oscillations.

Although the proposed design methods are substantially different from one another, the final designs perform comparably, as all the designs suffer from a fundamental limitation: to obtain a smooth dispersion curve on reflection, one must suppress the interference between the light reflected from the front interface and the light reflected within the multilayer structure. This problem is sometimes

referred to as the problem of impedance matching, because of the close analogy between chirped mirrors and inhomogeneous electric transmission lines that was recognised in Ref. [16]. Recently proposed implementations of CMs solve this problem by separating the two beams in space, achieving thus the ideal impedance matching [23, 24]. Drawing on this concept, mirrors that provide high reflectance and accurate dispersion control over a full optical octave were demonstrated [25, A3]. Mirrors of this kind manufactured by optically attaching a thin glass wedge on top of a multilayer structure (Fig. 1.1) were called tilted-front-interface (TFI) chirped mirrors [A3]. Similar to them back-side-coated (BASIC) chirped mirrors [25], which were proposed simultaneously with the TFI mirrors, are manufactured by growing a coating on a thin wedged substrate.

Although the recently found improved implementations and the analytical pre-design methods were essential for enhancing the performance of CMs, they did not obviate the need for efficient computer optimisation techniques. On the one hand, the quest for mirror designs with even larger bandwidth, which would permit the generation of nearly single-cycle pulses for scientific applications, makes requirements to chirped mirrors so extreme that even small improvements may play a crucial role. On the other hand, the high production cost of chirped mirrors demands designs with reduced sensitivity to small discrepancies between the layer thicknesses of a calculated design and those of the manufactured mirror, especially if the mirror is designed for a broad spectral range.

The following part of this chapter is organised as follows. In section 1.1 an efficient global optimisation algorithm is described, which has been found to be very successful for CM design. The subject of section 1.2 is the design of broadband chirped mirrors, the bandwidth of which approaches or even exceeds one optical octave. Such an extreme bandwidth poses additional problems and requires special approaches. In particular, it is beneficial to use specialised merit functions described in 1.2.1. The inherently high sensitivity of CM characteristics to manufacturing errors is discussed in section 1.3. In section 1.3.1 an optimisation algorithm is proposed which can be used to make designs more robust against

small random errors in layer thicknesses.

1.1 An advanced global optimisation algorithm

1.1.1 Challenges

Design of multilayer dielectric coatings usually consists of two parts: construction of a starting design, where available knowledge about physics of multilayer coatings can be exploited, and computer optimisation of the starting design, where layer thicknesses are considered as optimisation parameters, and the optimisation routine varies the thicknesses in order to minimise the value of a specially constructed *merit function*² $f(x_1, x_2, \dots, x_n)$. It was recognised long time ago that the main problem with computer optimisation of multilayer dielectric coatings is that the merit function of a multilayer coating has many local extrema if the number of layers is large (see, for example, [26]). This problem is illustrated by Fig. 1.2, where the merit function is plotted as a function of thicknesses of two layers of a broadband TFI chirped mirror. The surface shown in this plot has one relatively deep minimum and many local extrema close to it. Optimising such a mirror, we usually have to optimise all the layers simultaneously. It means that we have to search for a minimum in a space, the dimension of which is equal to the number of optimisation parameters. For example, the mirror used to make Fig. 1.2 consisted of 70 layers. Searching for a minimum of a function in the 70-dimensional space may become a challenging problem. In the rare occasion, when there is a downhill route from the starting design to the global minimum, a local optimisation routine would lead us to the best possible design. Otherwise there is always a risk that the local optimisation will get stuck far away from the global minimum.

Global optimisation was recognised long ago as a solution to this problem. Unlike local optimisation, which is usually a deterministic procedure that attempts

²It is a matter of convention, whether the merit function should be maximised or minimised in order to improve design performance. Throughout this thesis merit functions are considered to be constructed such that lower values correspond to better designs.

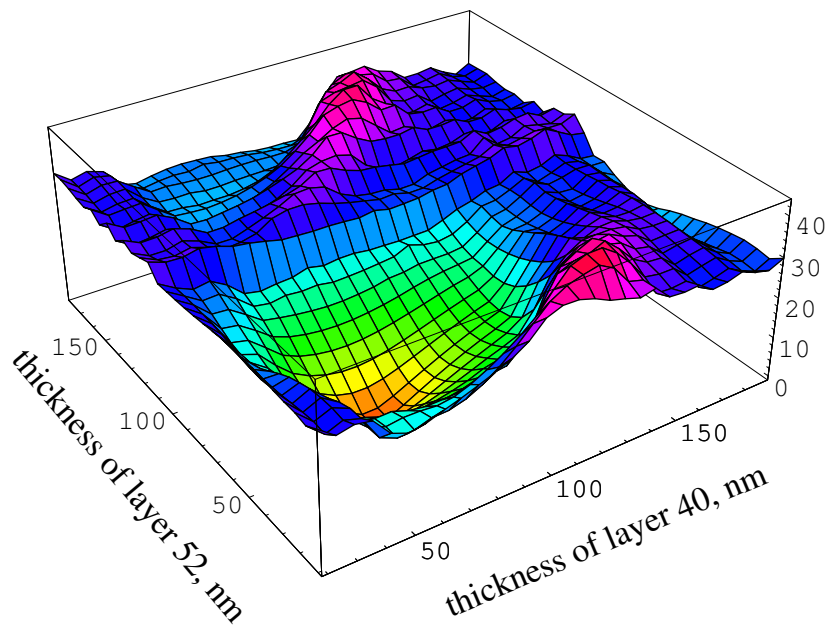


Figure 1.2: Merit function of a broadband TFI chirped mirror as a function of thicknesses of the 40th and 52nd layers. The coating consists of 70 layers, the merit function is based on simulation of pulse reflection (section 1.2.1). The merit function has many local minima, which create obstacles for local optimisation.

to find one of the nearest minima as quickly as possible, global optimisation algorithms are capable of optimising functions, which have many local minima, but these algorithms are not deterministic in the sense, that they exploit some strategy of *random* trials. There have been many successful attempts to apply global optimisation algorithms to the design of optical multilayer structures. In Ref. [27] authors compare different optimisation techniques, including a few global optimisation algorithms: adaptive random search, generalised simulated annealing, and Monte Carlo simulated annealing. Application of genetic algorithms to optimisation of optical interference coatings was discussed in detail in Ref. [28], while Ref. [26] was devoted to the thin-film design by simulated annealing. The algorithms were reported to be useful, but there was one common problem: all known global optimisation algorithms demand a large number of evaluations of the merit function. Therefore such an optimisation is often extremely time consuming.

1.1.2 The memetic algorithm and the optimisation of multilayer interference coatings

The approach I'm going to present is based on the so-called *memetic* algorithm [29]. On the web site [30] devoted to this class of algorithms they are introduced in the following way:

Memetic Algorithms is a population-based approach for heuristic search in optimization problems. They have shown that they are orders of magnitude faster than traditional Genetic Algorithms for some problem domains. Basically, they combine local search heuristics with crossover operators. For this reason, some researchers have viewed them as Hybrid Genetic Algorithms. However, combinations with constructive heuristics or exact methods may also belong to this class of metaheuristics. Since they are most suitable for MIMD parallel computers and distributed computing systems (including heterogeneous systems) as those composed by networks of workstations, they have also received the dubious denomination of Parallel Genetic Algo-

rithms. Other researchers know it as Genetic Local Search.

So, memetic algorithms can be defined as a class of evolutionary algorithms in which local search plays a significant role. Usually a type of genetic algorithm (a particular type of evolutionary algorithm) is used in conjunction with local optimisation. We adopt the terminology of evolutionary computation and call a set of trial designs a *population* and a particular design from this set a *member* of the population. Like in any genetic algorithm the memetic optimisation process evolves from population to population by means of crossover and mutation operators. The difference between the genetic and memetic algorithms is that in the latter each newly constructed member is locally optimised before it is included in the new population; i.e. constructing a new set of trial designs from the old set we locally optimise each design that is going to be added to the new set. This local optimisation does not necessarily have to lead to the very (local) minimum: the most important thing is that it be fast but able to considerably improve designs bringing them closer to local minima. The effectiveness of a memetic algorithm depends to a large extent on the effectiveness of the local optimisation, which I will call *partial refinement*. It turns out that this partial refinement can be performed very fast in the case of multilayer coatings.

The properties of multilayer dielectric structures are calculated by the transfer matrix method [31] (see A.1 in the appendix). To calculate the reflectivity of a mirror consisting of n layers at a particular wavelength, one has to calculate the product of n transfer matrices M_k . This is a very time consuming part of any CM optimisation routine. The calculations can be made faster if the merit function has to be evaluated for several designs that differ from some particular previously characterised design by thickness of only one layer. Let us define n matrices L_k

$$L_k = \begin{cases} \mathbf{1}, & k = 1, \\ \prod_{i=1}^{k-1} M_i, & 1 < k \leq n, \end{cases} \quad (1.3)$$

and n matrices R_k

$$R_k = \begin{cases} \mathbf{1}, & k = n, \\ \prod_{i=k+1}^n M_i, & 1 \leq k < n. \end{cases} \quad (1.4)$$

When all the matrices are calculated, one can quickly find the reflectivity in the case, when only the k th layer is changed, because only one single matrix M_k has to be calculated and only two matrix multiplications instead of $n - 1$ have to be performed:

$$\prod_{i=1}^n M_i = M_1 M_2 \dots M_{k-1} M_k M_{k+1} \dots M_n = L_k M_k R_k. \quad (1.5)$$

This opens a way for quick evaluation of the gradient of the merit function, quick optimisation of one particular layer, and so on. There are a few ways, how to implement partial refinement by using this method. For example, one can calculate the gradient and optimise the mirror along the gradient direction or optimise each layer one by one.

The whole algorithm I utilised for optimisation of CMs is built as following. The initial population (the set of initial designs) is constructed randomly (except, maybe, a few designs which can be obtained from the analytical theory [21] or from previous optimisations). All the designs have the same number of layers made from the same materials; only the layer thicknesses are different. On each iteration two members of the population are randomly chosen according to their values of the merit function: the lower the value is, the more chances there are that the member will be selected (the rank selection was used). After that a new member is formed by the crossover: a part of its layers is taken from the first design, the rest is taken from the second design, and together they form the new member; the sizes of the parts are determined randomly each time. To avoid congestion of designs in a small number of local minima, a simple heuristic check can be made on whether the newly formed member is in the same local minimum as one of the existing members: for each of the designs I check whether the maximal difference between layer thicknesses of the selected and the newly constructed designs is smaller than 10 nm. If this is the case, the designs are moved towards each other

step by step (considering each design as a point in the multidimensional parametric space) as long as the steps decrease the value of the merit function. If this procedure decreases the distance between the designs to zero, one of the designs is excluded from the population. Finally, a partial refinement of the new member is performed and the new population is formed by adding the member to the old population. In a last step the worst member of the new population is “killed” (extracted from the population) if the population size exceeds some prescribed limit. When the global optimisation is completed (after the specified number of iterations is reached or some convergence criterion is fulfilled), a few best members are chosen and further optimised with the aid of a full-power local optimisation (conjugate gradients algorithm, for example).

1.1.3 Advantages of the memetic algorithm

Global optimisation outperforms local optimisation algorithms, particularly if no good starting design is available. Despite the progress in analytical design techniques for CMs, for several dispersive-mirror design problems no direct synthesis is currently possible. One of these problems is the design of dichroic CMs (input-couplers) used in femtosecond lasers, where they exhibit high reflectance and controlled negative dispersion over the fluorescence spectrum of the active laser medium and high transmittance over the relatively narrow wavelength range, at which the medium efficiently absorbs the pump radiation. Although double-chirped mirrors inherently tend to exhibit large transmittance at wavelengths below the high-reflectance range, parameters such as position, width and losses of the high-transmittance band cannot be explicitly taken into account by analytical pre-design, thus the use of a global optimisation technique is called for.

Fig. 1.3 presents a CM designed to be used as an input coupler of a Ti:Sapphire oscillator that has a high reflectance and a nearly constant GDD in the range 650-900 nm (the target GDD was set to -35 fs^2) and transmission as high as possible in the range 527-537 nm. The mirror consists of 60 layers made of two materials: the low-refractive-index material is SiO_2 , and the refractive index of the second ma-

material is equal to 2.25 at 800 nm (these materials are used by LAYERTEC GmbH; the exact chemical formula of the high-refractive-index material has not been revealed to us, although we know the dispersion properties of this material). The mirror was designed, first, with the conjugate gradients algorithm starting from a double-chirped design provided by the analytical theory [21] and, second, by use of the memetic algorithm, where the double-chirped design was included into the initial population, which consisted of 100 members, and the rest of the population was made up of designs with random layer thicknesses. 3000 iterations of the memetic algorithm were performed. As can be seen from Fig. 1.3, the global optimisation found a better solution than the local refinement.

As stated above, without the partial refinement the memetic algorithm would be just a genetic algorithm. The effectiveness of the memetic approach is demonstrated by a comparison of optimisations with and without the partial refinement. Such a comparison is shown in Fig. 1.4. The algorithms cannot be compared in terms of the number of merit function evaluations, because the memetic algorithm uses two different ways to calculate the function, so they can only be compared in terms of the processor time required by the optimisation (a PC with a 600 MHz Athlon processor was used). Although the partial refinement slows down the optimisation process at the initial stage, it allows the memetic algorithm to outperform its genetic counterpart on the long-term run.

Finally I would like to summarise my experience with design of “ordinary” CMs using the memetic algorithm. The theory of double-chirped mirrors usually provides very good starting designs. Such a design should include at least three different parts [21]: an anti-reflection coating, a double-chirped part, and a Bragg reflector which usually consists of a few layers and serves to improve the mirror’s reflectance. It is necessary to notice that the double-chirping approach has some free design parameters, the most important being the number of layers assigned for each of the parts and the choice of the double-chirping method. One can vary these parameters to obtain a set of starting designs, each of those can either be optimised locally or serve as a member of the initial population for the memetic

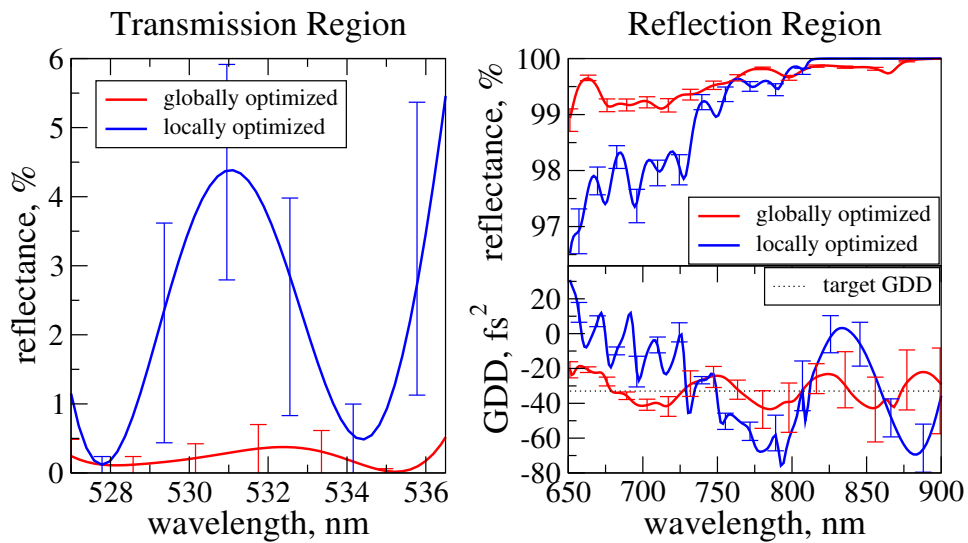


Figure 1.3: Comparison of an input-coupler design found by the memetic algorithm (red curves) with that obtained by local optimisation using the conjugate-gradient algorithm (blue curves). Large transmittance in the wavelength range 527-537 nm as well as high reflectance in the range 650-900 nm together with the target dispersion of -35 fs^2 were required. The error bars correspond to perturbation of layer thicknesses with the standard deviation of 1 nm (discussed in section 1.3).

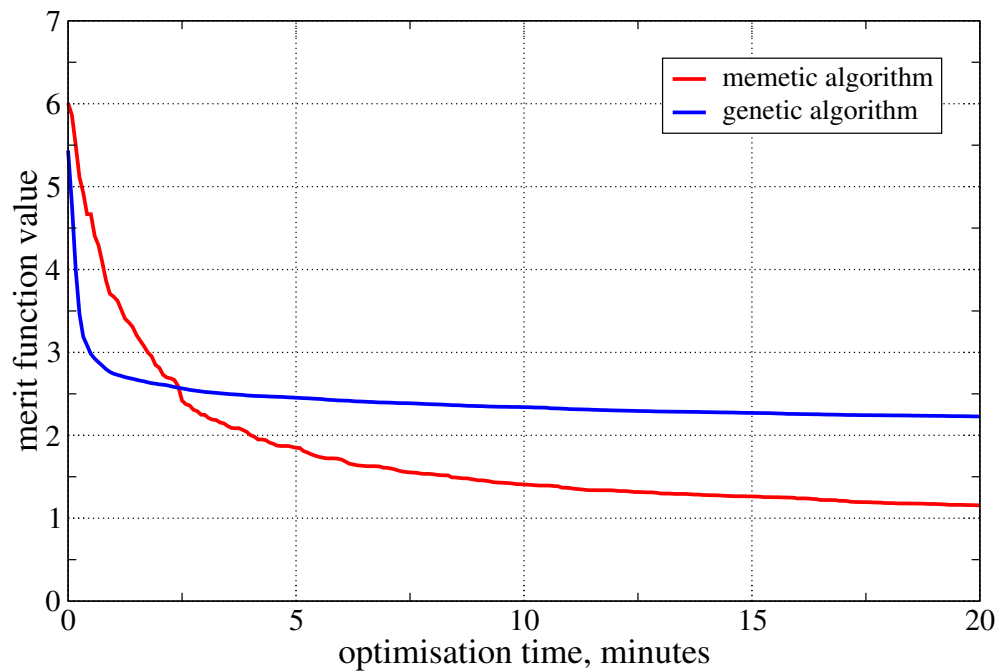


Figure 1.4: Comparison of the memetic algorithm with the genetic algorithm formed by exclusion of the partial refinement. The y-axis is the value of the merit function of the best member in the population. Each curve is the result of averaging over 11 runs of the optimisation code.

algorithm. It is a good idea to let the number of double-chirped layer pairs take all the values allowed for a fixed overall number of layers.

A simple local optimisation of a double-chirped design often results in a coating of a good quality, but the quality can be improved even further, if one employs the memetic algorithm. It usually does not make much difference, whether one applies the global optimisation directly to the analytic designs, or optimises them locally first and then includes them into the initial population. A typical example is presented in Fig. 1.5. This is a CM designed to compensate for 0.75 mm of Ti:Sapphire in the wavelength range 625-975 nm. The mirror consists of 65 layers made of the same materials as the mirror in Fig. 1.3. The solid black curves correspond to the best result obtained by local optimisation of double-chirped designs, the blue and the red curves correspond to designs, obtained with the memetic algorithm, where the initial population either contained the “raw” double-chirped designs (red curves) or was formed by perturbing layer thicknesses of the best locally optimised double-chirped design (blue curves). One can see, that the latter two approaches provide designs of a comparable quality, and both of them outperform the locally optimised double-chirped design.

1.2 Extremely broadband chirped mirrors

The pursuit to generate ultrashort light pulses with duration approaching the one-cycle limit created a demand of dispersion control over large bandwidths. At present chirped mirrors are the only tool suitable for accurate dispersion compensation in a spectral range approaching or even exceeding one optical octave. Such an extreme bandwidth of operation creates new challenges and difficulties, makes some of the small-bandwidth approaches ineffective, and therefore deserves a special treatment.

In contrast with coatings designed for a modest bandwidth, dispersion control in a broad spectral range can only be realised with chirped mirrors, where the basic mechanism of dispersion control is the difference in penetration depths for

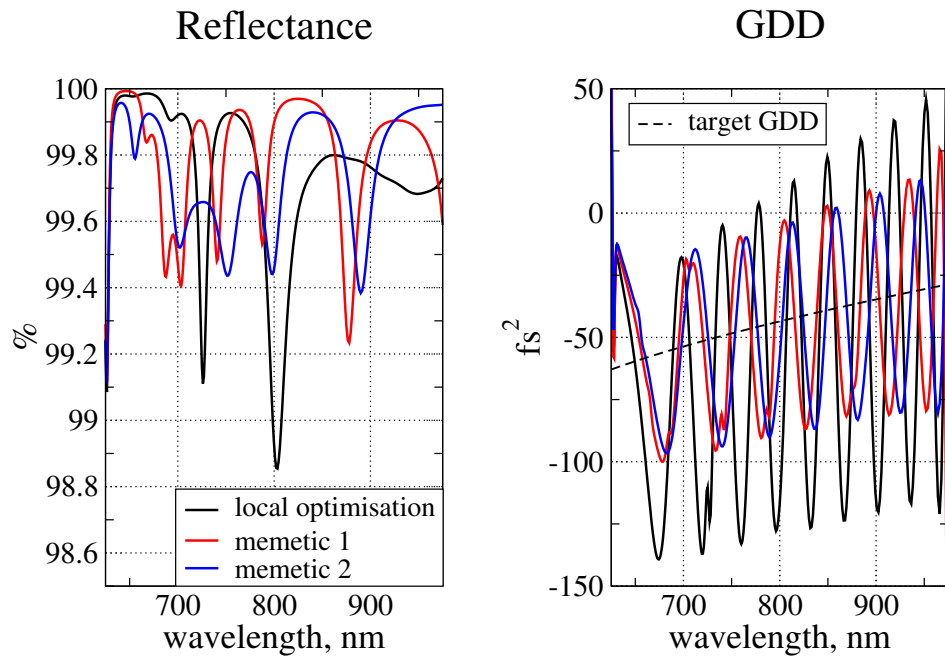


Figure 1.5: A chirped mirror compensating for the dispersion of 0.75 mm Ti:Sapphire in the wavelength range 625-975 nm, which was designed in three different ways: the local optimisation of a double-chirped design (marked as “local optimisation”), the optimisation with the memetic algorithm, where the initial population was made up of random designs together with a few double-chirped designs (marked as “memetic 1”), and the optimisation with the memetic algorithm, where the initial population was formed by perturbing layer thicknesses of the “locally optimised” design (marked as “memetic 2”).

different wavelength components. For a smaller bandwidth other types of optical interference coatings exist, which may outperform chirped mirrors. For example, the multiple-cavity Gires-Tournois interferometer reported in Ref. [32] has a smooth dispersion and an extremely high reflectance in the wavelength range 740-860 nm. However, as practice shows, these approaches don't work for larger bandwidths, because it becomes increasingly difficult to make wavelength components interfere in a proper way in the whole spectral range, unless different components are reflected more or less at different parts of the coating. It also turns out, that several kinds of optical coatings can't be designed at all, if the bandwidth of operation approaches an optical octave: examples include Bragg-reflectors and positive-dispersion mirrors.

The GDD of a chirped mirror usually oscillates around some smooth target dispersion. As the bandwidth of a design is increased, the amplitude of the GDD oscillations grows and at some point it may become intolerable. Currently there are two approaches, which allow to overcome this problem. One of them is represented by the TFI or BASIC mirrors mentioned in the introduction (page 11). Solving the problem of parasitic interference between the light reflected off the mirror's surface and the light reflected within the multilayer structure, this approach leads to designs of broadband CMs with very smooth dispersion characteristics. Design of these mirrors doesn't differ from the design of ordinary CMs, except that the medium of incidence is not air, but some optically dense material, whose refractive index is close to the refractive index of one the layer materials. Another useful approach to increase the bandwidth of CMs is to use pairs of mirrors designed for mutual compensation of GDD oscillations [33]. In this case each of the mirrors may have relatively large GDD oscillations, but the net dispersion of the pair is smooth. To design such a pair of mirrors one has to optimise layer thicknesses of both mirrors simultaneously using the same algorithms as for design of single mirrors.

Although the design of ultrabroadband CMs doesn't require new optimisation techniques, it does require that one should be much more careful defining

optimisation targets. It turns out, that an accurately chosen merit function is indispensable for successful design of ultrabroadband coatings.

1.2.1 A merit function based on simulation of pulse reflection

An ideal CM would reflect 100% of the incident radiation and introduce a GDD exactly equal to the prescribed one. Thus, the merit function commonly used for characterising properties of dispersive multilayer coatings has the form [5]:

$$f(x_1, x_2, \dots, x_n) = \frac{1}{m} \sum_{i=1}^m (v_i(1 - R_i)^2 + w_i(\tilde{D}_i - D_i)^2), \quad (1.6)$$

where R_i and D_i are the reflectance and the GDD of the mirror at the wavelength λ_i calculated from the parameters of the merit function x_1, x_2, \dots, x_n , \tilde{D}_i is the target GDD at this wavelength, v_i and w_i are the weights given to the reflectance and the GDD values, respectively. The number of wavelengths m , at which the reflectance and the GDD have to be evaluated, depends on the required bandwidth; for a chirped mirror with the bandwidth of 200 ÷ 300 nm it is reasonable to take $m \sim 100$.

Standard CMs can be efficiently designed by employing this merit function. Usually both a reflectance close to 100% and accurate GDD control over ≈ 300 nm can be achieved with a moderate (< 50) number of layers. Extreme design specifications such as bandwidth approaching an optical octave call for a trade off between reflectance/transmittance and GDD deviations making the choice of the weights in Eq. (1.6) non-trivial. For example, at some iteration an optimisation algorithm may have to choose between two designs: one with an average reflectance of 98% and an amplitude of GDD oscillations of 30 fs², and the other with an average reflectance of 97%, and GDD oscillations having an amplitude equal to 10 fs². Which of these designs will be preferred depends on the weights given to the reflectance and the GDD in Eq. (1.6), but which of them is really better for a particular application?

There is another problem with the merit function defined by Eq. (1.6). If GDD curves of two different designs exhibit the same second-order momentum deviation

tions from the target GDD, their contributions to the merit function (1.6) will be equal. Still, reflecting the pulse off the mirrors with identical merit functions can affect the temporal shape of the pulse in very different ways. Mirrors introducing a residual GDD described by the full oscillating curve or by the dashed step-like curve in Fig. 1.6 (left plot) have the same figure of merit according to Eq. (1.6) (we assume that the reflectance is 100% in both cases). The effect of the residual chirp corresponding to the two GDD curves on a 5-fs bandwidth-limited Gaussian pulse (having a centre wavelength of 800 nm) is also shown in Fig. 1.6 (right plot). The oscillating dispersion distorts the pulse shape to a much smaller extent, although both residual GDDs deliver exactly the same contribution to the merit function (1.6). This ambiguity and the difficulty in choosing the weight coefficients can be avoided by using a merit function that directly evaluates the effect of the amplitude and phase change introduced by the mirror on a reflected broadband pulse.

The effect of the reflection on the temporal pulse shape can be calculated by multiplying the complex spectrum of the incident pulse by the transfer function of the mirror $H(\omega) = |r(\omega)| \exp[i\varphi(\omega)]$, where $r(\omega)$ and $\varphi(\omega) = \arg[r(\omega)]$ are the complex reflectivity and the phase shift on reflection, respectively. Fourier transforming the product yields the temporal shape of the reflected pulse. To evaluate the quality of a design one should take a sufficiently short trial pulse and set $\varphi(\omega)$ equal to the difference between the target phase and the phase shift introduced by the mirror.

The evaluation of the merit function based on simulation of pulse reflection is more time-consuming than the evaluation of Eq. (1.6), because it involves calculating a Fourier transform (even if the fast Fourier transform algorithm is applied). Thus, such a merit function should only be used for optimisation of sophisticated dispersive coatings (e.g. chirped input/output couplers or ultrabroadband CMs) that can not be unambiguously characterised by the standard merit function (1.6). Fig. 1.7 compares two CMs, one of which was optimised to yield maximum peak intensity of the reflected pulse, and the other was optimised to minimise (1.6).

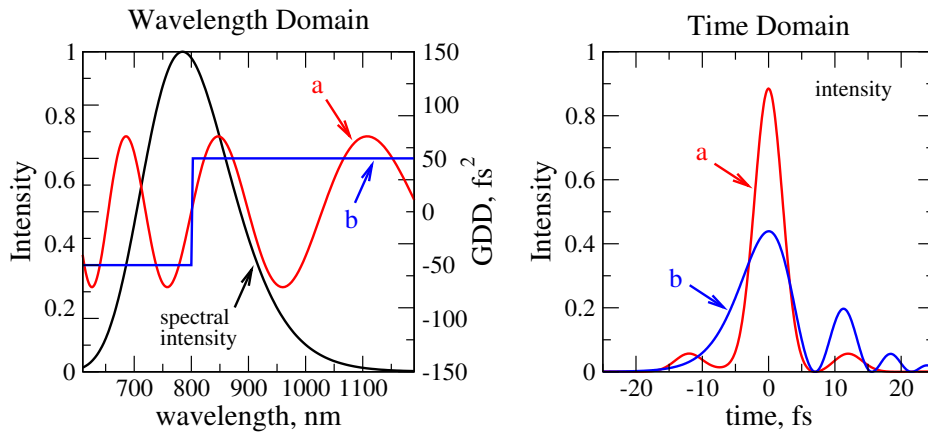


Figure 1.6: Comparison of influences of oscillating (a) and step-like (b) deviations from the GDD target on the shape of a 5-fs bandwidth-limited Gaussian pulse: The left panel depicts the spectrum of the pulse and GDD deviations from the target that produce equal contributions to the merit function given by Eq. (1.6). The step-like GDD distorts the pulse shape much more strongly compared to the oscillating GDD as revealed by the respective reflected temporal intensity profiles (right panel).

Although the GDD oscillations are much smaller and the reflectance is better in the second case, the corresponding pulse is much longer.

Depending on the parameters most critical for the application, either the peak intensity, the pulse duration (root mean square or full width at half maximum), or a weighted combination of these parameters can be used to construct the merit function. Obviously, traditional targets can be additionally used, e.g. in order to impose a high transmittance within the absorption-band of a laser medium that is necessary for input-couplers. An example of an ultrabroadband TFI chirped mirror designed with such a merit function is given by Fig. 1.8. The mirror consists of 70 layers made of the “Layertec” materials (section 1.1.3 on page 18). The mirror was designed with the additional requirement that the reflectance be as high as possible in the long-wavelength part. After several attempts the following merit

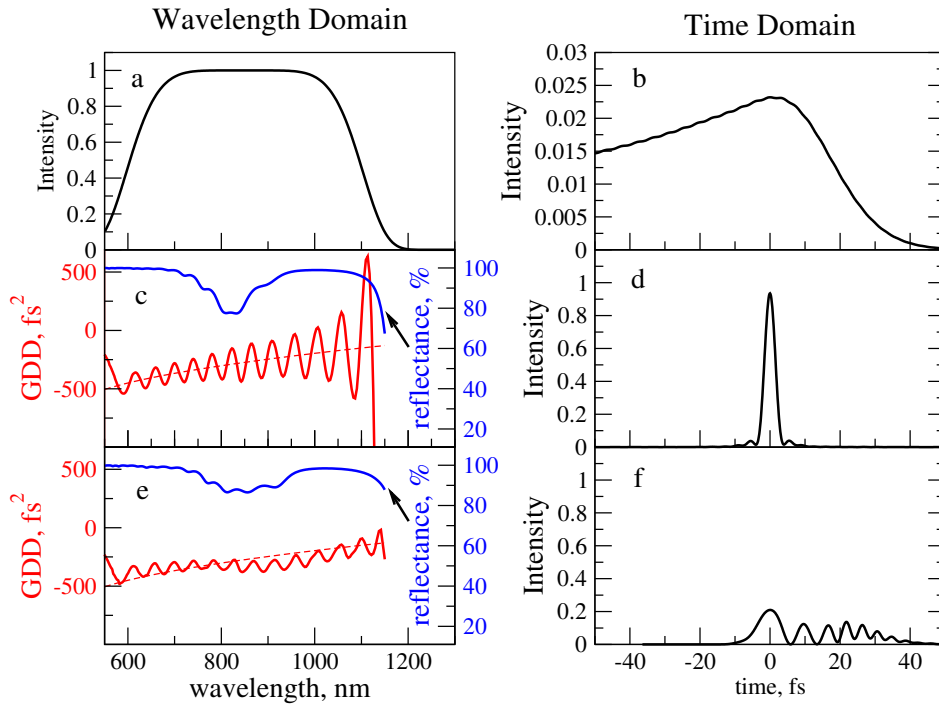


Figure 1.7: Comparison of two TFI chirped mirrors. The incoming pulse (for the compression of which the mirrors were designed) is shown in panel (b). It has the spectrum depicted in (a) and carries a chirp corresponding to a 10 mm propagation path through fused silica. Panels (d) and (f) show the calculated intensity obtained after 10 bounces of the chirped pulse off a mirror optimised for the peak intensity of the reflected pulse and off a mirror optimised with the conventional merit function, respectively. Comparison between (d) and (f) clearly demonstrates that compression with the mirror optimised with the conventional merit function (e), which has smaller GDD oscillations and better reflectance, results in a much poorer pulse shape.

function was found to provide a satisfactory result:

$$f = \left(\frac{W - \tilde{W}}{\tilde{W}} \right)^4 + \frac{1}{N} \left[\sum_{550 \leq \lambda_i \leq 1100} \begin{cases} \left(\frac{0.8 - R_i}{0.01} \right)^4, & R_i \leq 0.8, \\ 0, & \text{otherwise} \end{cases} + \sum_{\lambda_i > 1100} \left(\frac{1 - R_i}{0.01} \right)^4 \right], \quad (1.7)$$

where W is the root-mean-square (RMS) width of the reflected pulse, \tilde{W} is the RMS width of the trial pulse, R_i is the reflectance at the wavelength λ_i , the summation is performed over N wavelengths λ_i , at which mirror properties are evaluated. The first term in (1.7) sets the requirement that the dispersion broadening of the trial pulse followed by dispersion compensation (one reflection off the mirror) should change the duration of the pulse as little as possible. The rest of the merit function represents the target for reflectance, where the mirror's bandwidth is split into two regions: in the spectral region $550 \leq \lambda_i \leq 1100$ we do not care about reflectance if it is larger than 80%, while in the spectral region $\lambda > 1100$ nm reflectance as high as possible is demanded.

1.3 Sensitivity to perturbations of layer thicknesses

Any manufacturing process introduces systematic and random errors into the optical thicknesses of layers. The systematic errors (like, e.g. a uniform increase in the thickness of all layers) are usually not critical for CMs, because these errors only slightly change the reflectance and dispersion characteristics and/or shift them in the spectral domain, but the random perturbations pose a serious problem. The group delay dispersion (GDD) of CMs is very sensitive to small discrepancies between the layer thicknesses of a calculated design and those of the manufactured mirror. This effect becomes more and more pronounced as the required spectral range gets broader. Modern technologies, like ion-beam sputtering, allow control of layer thicknesses within a fraction of nanometre, but even these small deviations can make the GDD of a manufactured design very different from the expected one.

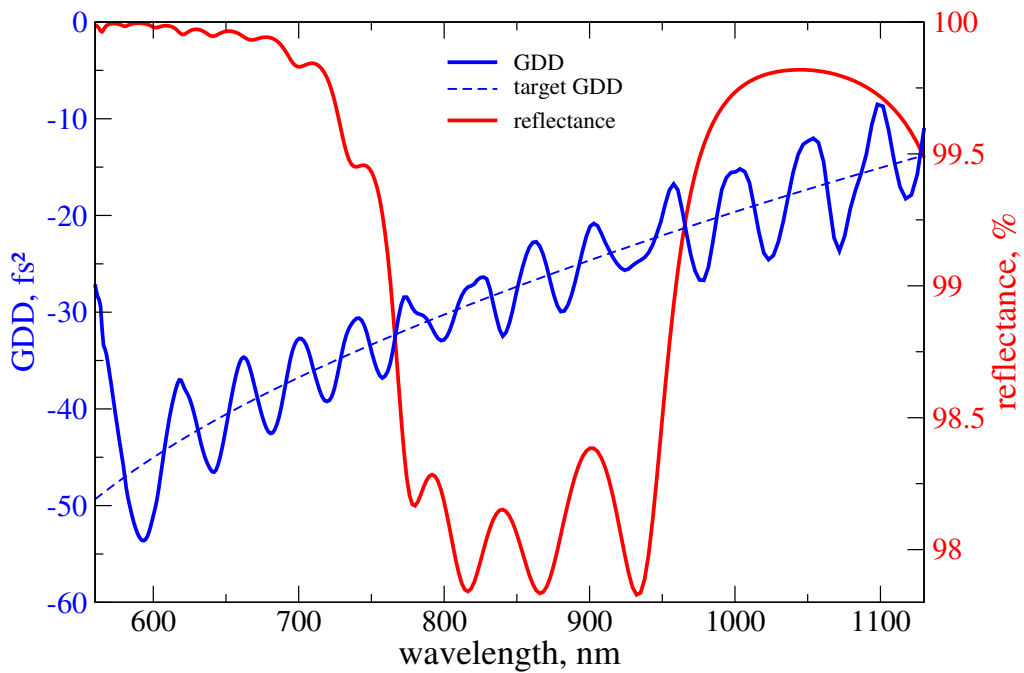


Figure 1.8: An example of a broadband TFI chirped mirror designed for the wavelength range 560-1130 nm. The mirror consists of 70 layers, the incidence medium is fused silica, the angle of incidence is 5° , the light is p-polarised. Neither the reflectance of the fused-silica wedge to the air, nor the dispersion of the wedged plate were taken into account in this figure.

This sensitivity may be regarded as an additional design criterion, it should be taken into account when choosing the best design out of a few comparable ones, and it can be optimised with a proper algorithm. In this section I present such an algorithm that can be used to make designs more robust and more suitable for manufacturing, but first, I would like to put down a few simple but important statements about the sensitivity.

- Reflectance of a chirped mirror is usually rather insensitive to small perturbations, while the GDD oscillations may grow by an order of magnitude as compared to the ideally manufactured mirror. This is explained by the fact that the dispersion $\text{GDD}(\omega) = -\varphi''(\omega) = -d^2(\arg[r(\omega)])/d\omega^2$ being the second derivative of the phase shift is very sensitive to small frequency-dependent changes of the complex reflectivity $r(\omega)$ introduced by the perturbations, while the reflectance $R(\omega) = |r(\omega)|^2$ doesn't involve any differentiation and, consequently, it is more robust against the perturbations.
- Even a single thin layer can make a CM design very sensitive to perturbations of layer thicknesses, especially, if this layer is close to the front interface of the mirror. If an optimisation process has not made the layer infinitely thin, then the layer, even being much thinner than the wavelength, is supposed to play an important role in the coating. In this case it is not surprising when a perturbation comparable to the thickness of the layer has a big impact on mirror properties. Unfortunately, thin layers ($\lesssim 10\text{nm}$) are unavoidable in broadband CMs. Nevertheless a reasonable compromise can always be found.
- The larger the penetration depth, the higher the sensitivity is. For example, negative-dispersion CMs are always more sensitive in the long-wavelength region, because the penetration depth increases with the wavelength.

As a good example of how important the penetration depth can be in the context of sensitivity, let us consider a CM with a high third-order dispersion (TOD).

This mirror was manufactured and now it is used in pulse-compression experiments. The requirements to the design were the following: the third- and the fourth-order dispersion at the central wavelength $\lambda_0 = 800\text{nm}$ had to be equal to 600fs^3 and 1800fs^4 , respectively, the second-order dispersion $D_2(\lambda_0)$ was a free parameter, the mirror had to be designed for the wavelength range 680-930 nm. Setting $D_2(\lambda_0)$ to 100fs^2 one can design a mirror, for which the GDD closely follows the target curve shown in Fig. 1.9 in the left panel. Nevertheless, this design has virtually no chance to become a useful mirror when manufactured, since the sensitivity of its GDD to small perturbations of layer thicknesses is very high in the short-wavelength region, as it is revealed by the sensitivity analysis: each error bar in the plot represents the smallest GDD range such that the probability of GDD being in this range is equal to $\text{erf}(1/\sqrt{2}) \approx 0.68$ (the probability of finding a normally distributed random variable within the root-mean-square width of the distribution). The sensitivity can be reduced dramatically, if one sets the $D_2(\lambda_0) = -100\text{fs}^2$. The GDD of a mirror designed with this target is shown in Fig. 1.9 in the right panel. As one can see, the error bars are significantly shorter in the latter case, and the mirror is most sensitive in the long-wavelength region. An insight into why the sensitivity depends so much on the target $D_2(\lambda_0)$ can be given by electric-field intensity plots, such as the ones shown in Fig. 1.10. The GDD of a mirror is positive, if the penetration depth decreases with the wavelength. Since $D_2(\lambda_0) = 100\text{fs}^2$ implies a large positive target GDD in the short-wavelength region, large penetration depths are unavoidable for short wavelengths. Thus, mirrors generated with this target will inevitably be very sensitive in this region. The sensitivity can be diminished, if one carefully selects $D_2(\lambda_0)$ in order to make the penetration depth as uniform as possible over the whole spectral range. For the considered design the optimal value is close to $D_2(\lambda_0) = -100\text{fs}^2$ (Fig. 1.10, the right panel).

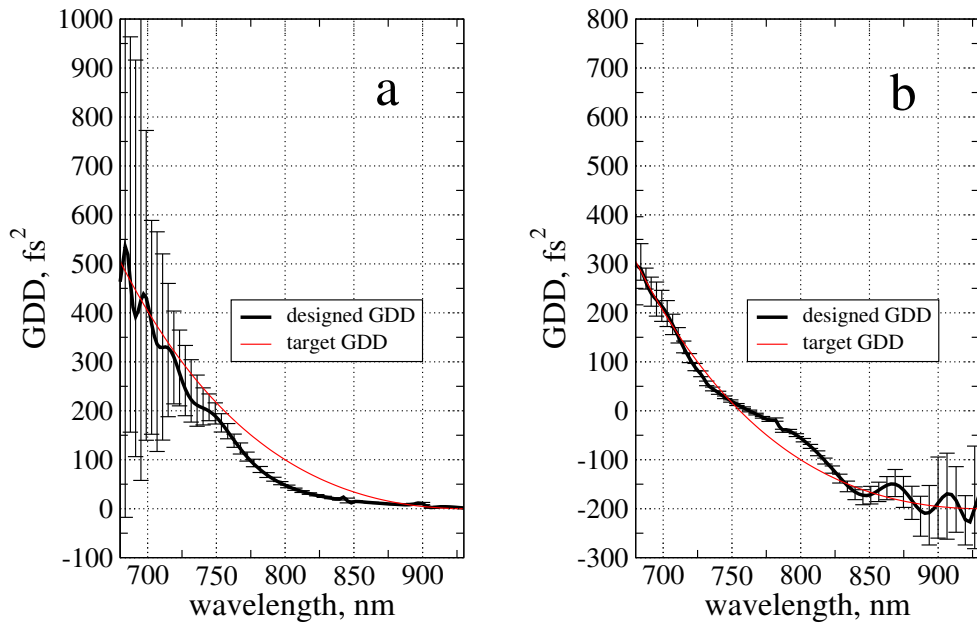


Figure 1.9: Chirped mirrors designed to have a large TOD, where the target GDD at the central wavelength $D_2(\lambda_0)$ is a free parameter equal to 100 fs^2 for the mirror (a) and -100 fs^2 for the mirror (b). The error bars are calculated from analysis 1000 randomly perturbed designs, where the perturbations of layer thicknesses have the Gaussian distribution with the standard deviation of 1 nm .

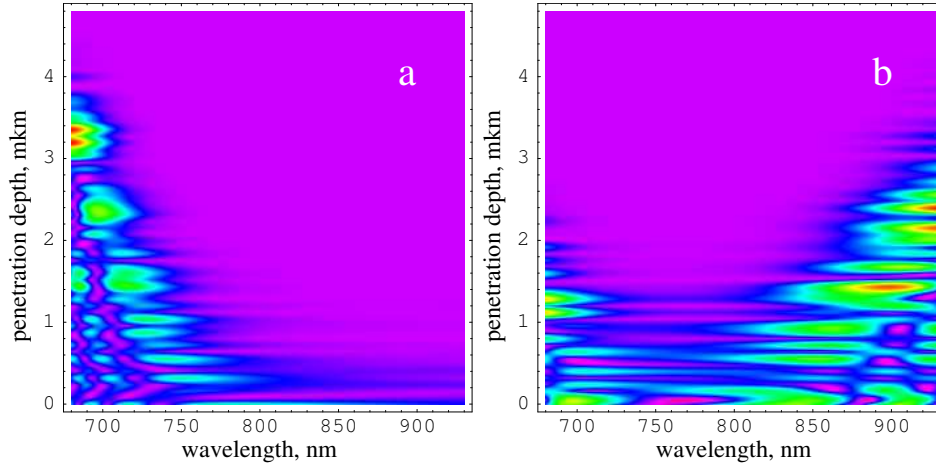


Figure 1.10: The electric-field-intensity plots for the mirrors presented in Fig. 1.9. Red colour represents large values of the squared amplitude of the electric field $|E_0|^2$, while the violet colour corresponds to small values of $|E_0|^2$. From these figures one can see that the sensitivity is higher in those parts of the spectral range, where the penetration depth is larger.

1.3.1 Stochastic quasigradient algorithm

The global optimisation algorithm, described in section 1.1.2, leads to a set of designs of comparable quality. In analysing these designs, one may notice that they have different sensitivities to random perturbations of layer thicknesses. This raises the question: is it possible to optimise this sensitivity? There have been attempts to do so; for example, the sensitivity optimisation is included in commercial software [34] (where it is known to work quite slowly). Here I report an attempt to apply algorithms of optimisation of noisy functions to the design of chirped mirrors.

Why should the merit function be noisy and how can it be made so? If one were able to evaluate the merit function for each of the trial designs by manufacturing the corresponding mirror and measuring its properties, the function would look as if some noise were added to it. To find a minimum of such a function would mean to find a point, where its average value is minimal, and this solution would obviously give us the most robust design. This noise can be simulated

by calculating the merit function each time not exactly for the given layer thicknesses but for randomly perturbed thicknesses for which the random perturbation simulates the errors introduced by the manufacturing process.

The classical optimisation algorithms are barely applicable, when the function values are corrupted with noise, because they rely on determinism of the merit function. One of the approaches that are suitable for this case is known under the name “stochastic quasigradient methods” [35]. The underlying idea is simple: at each iteration the gradient of the merit function is estimated and a step in the direction opposite to the gradient is made. It resembles the steepest descent method, but the stochastic nature of the merit function requires specialised techniques to estimate the gradient and places certain restrictions on the sequence of step sizes. If all the necessary mathematical conditions (thoroughly described in [35]) are met, the algorithm is guaranteed to converge to a stationary point with probability 1, though the convergence may be very slow. One of the advantages of this method is that the sensitivity does not have to be explicitly calculated to be optimised. The algorithm I implemented is analogous to the one used for the feed-back control of adaptive optics [36], for which it is termed “parallel stochastic perturbative gradient descent”. To estimate the gradient of the merit function, the simultaneous perturbation approximation [37] was used. Let (x_1, x_2, \dots, x_n) be a vector of layer thicknesses. The noisy merit function $\tilde{J}(x_1, x_2, \dots, x_n)$ is connected to the exact merit function $J(x_1, x_2, \dots, x_n)$ by applying random technological perturbations to the layer thicknesses:

$$\tilde{J}(x_1, x_2, \dots, x_n) = J(T_1(x_1), T_2(x_2), \dots, T_n(x_n)). \quad (1.8)$$

To estimate the gradient of this function let us introduce m vectors of n mutually independent random variables $(\xi_{k1}, \xi_{k2}, \dots, \xi_{kn})$, $k = 1, \dots, m$. If the variables satisfy certain mathematical conditions [37], the most important of which are that 1) the variables must have zero expectation value $E(\xi_{ki}) = 0$ and 2) $E|\xi_{ki}^{-1}|$ or some higher inverse moment of ξ_{ki} must be bounded, then the gradient

of $\tilde{J}(x_1, x_2, \dots, x_n)$ may be estimated from $2m$ measurements:

$$\nabla \tilde{J} \approx \frac{1}{m} \sum_{k=1}^m \begin{pmatrix} \frac{\tilde{J}_k^+ - \tilde{J}_k^-}{2c_k \xi_{k1}} \\ \vdots \\ \frac{\tilde{J}_k^+ - \tilde{J}_k^-}{2c_k \xi_{kn}} \end{pmatrix}, \quad (1.9)$$

where

$$\begin{aligned} \tilde{J}_k^+ &= J(T_1(x_1 + c_k \xi_{k1}), T_2(x_2 + c_k \xi_{k2}), \dots, T_n(x_n + c_k \xi_{kn})), \\ \tilde{J}_k^- &= J(T_1(x_1 - c_k \xi_{k1}), T_2(x_2 - c_k \xi_{k2}), \dots, T_n(x_n - c_k \xi_{kn})), \end{aligned}$$

and c_k is a positive scalar determining the step size. It is common to take the random variables ξ_{ki} as symmetrically Bernoulli distributed: $\xi_{ki} = \pm 1$ with equal probabilities $P(1) = P(-1) = 1/2$. In this case $E(\xi_{ki}) = 0$ and $E|\xi_{ki}^{-1}| = 1$, so that the necessary conditions for (1.9) are satisfied. A larger number of iterations m provides a more accurate estimation of the gradient, improving the convergence of the algorithm, but requires more evaluations of the merit function, increasing the time necessary for one iteration. A compromise should be found that will produce the best performance. The remarkable feature of this algorithm is that the optimal value of m is often much smaller than the number of variables n , which makes the algorithm faster than the one based on the ‘‘classical’’ estimation of the gradient.

A result of the sensitivity optimisation is shown in Fig. 1.11. The mirror consisting of 49 layers was optimised in the wavelength range 650-900 nm for the normal incidence of light from the air. The design obtained was further optimised with the aid of a simple implementation of the stochastic quasigradient algorithm, in which the step size was kept constant (equal to 0.5 nm), the random variables ξ_{ki} were allowed to take only values $+1$ and -1 with equal probabilities, c_k were chosen to be equal to 2 nm; 10000 iterations were performed to get the final design. Two major assumptions were made regarding the error distribution of layer thicknesses introduced by the manufacturing process: first, the perturbations were simulated by an additive noise that affected all the layers in the same way, and, second, the distribution was taken to be Gaussian with a standard deviation of

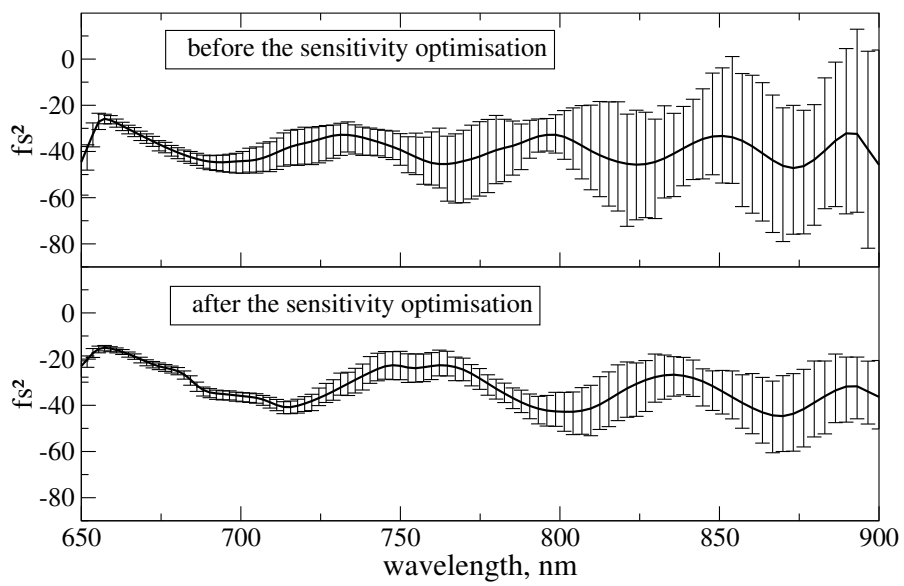


Figure 1.11: The result of sensitivity optimisation of a modest-bandwidth chirped mirror. The mirror consists of 49 layers, the incidence medium is the air, normal incidence. The error bars were obtained for the standard deviation of technological errors equal to 1 nm.

1 nm. It was observed that the sensitivity optimisation substantially shortens the error bars. Although the optimisation tends to decrease the quality of the ideally manufactured design (with the layer thicknesses exactly equal to the prescribed ones), this effect may be overcompensated by improved design robustness, provided the technological perturbations have been well enough approximated.

Chapter 2

High harmonic imaging of few-cycle laser pulses

In ordinary optics a laser pulse is well defined for all practical purposes, when its envelope and chirp or, equivalently, the spectrum and the relative phases between the spectral components are known. With extremely short pulses the peak heights of the electric field vary significantly with their positions under the envelope. To determine these positions, the “carrier-envelope” (also known as “absolute”) phase φ_{CE} must be known in addition to the relative phases between spectral components. For a chirp-free pulse with fundamental frequency ω_l one can define φ_{CE} by writing the electric field $E(t)$ as

$$E(t) = f(t) \cos(\omega_l t + \varphi_{\text{CE}}). \quad (2.1)$$

The pulse envelope $f(t)$ is chosen such that the maximal electric field strength for a given envelope is reached at $t = 0$ for a “cosine pulse” $\varphi_{\text{CE}} = 0$, while a “sine pulse” $\varphi_{\text{CE}} = \pi/2$ has two smaller field peaks with opposite signs (Fig. 2.1).

Without stabilisation, the CE phase changes randomly from pulse to pulse [38]. If pulse duration is much larger than one optical cycle, all known physical effects are insensitive to the CE phase. The situation changes for few-cycle pulses. In this case the CE phase was predicted [39, 40, 41, 42, 43] and observed [A4, 44] to affect strong-field phenomena, manifesting itself in harmonic spectra, harmonic

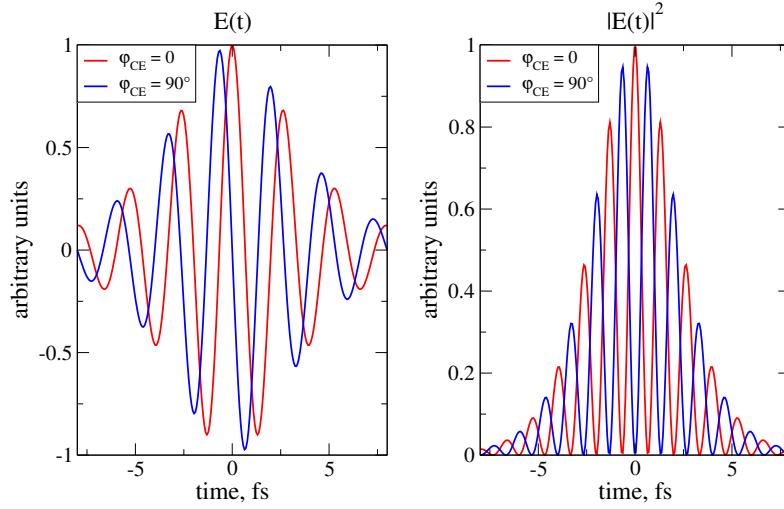


Figure 2.1: A “cosine” ($\varphi_{\text{CE}} = 0$) and a “sine” ($\varphi_{\text{CE}} = 90^\circ$) laser pulses. The cosine pulse has one dominant peak of intensity, while the sine pulse has two dominant peaks that are equal in magnitude as long as the pulse envelope is symmetric and chirp is absent. The pulses in this figure have a sech shape with the FWHM of 5 fs.

yield, energy and angular distribution of photoelectrons. Still, it was only recently that the advances in the generation of ultrashort laser pulses allowed to stabilise [15] and measure [A4] the CE phase.

The stabilisation of the CE phase allowed for the first time to measure high-harmonic spectra for a fixed value of the phase, and not just an averaged spectrum. Although the structure of these harmonic spectra had already been predicted by numerous numerical calculations [40, 42, 45, 46, 47, 48, 49, 50, 51, 52, 53], nobody had proposed a method of systematical analysis of experimental spectra and it was not clear, what kind of information could be extracted from them. In this chapter it will be shown that the high harmonic power spectrum provides an image of the strongest laser electric field peaks giving direct access to intensity, pulse duration, and φ_{CE} up to an ambiguity with respect to the overall sign of the electric field and the sequence of field peaks in the pulse. By looking at harmonics we literally for the first time can have a look on the electric field of a short light pulse.

This chapter is organised in the following way. In section 2.1 I briefly describe the model used for simulations of high-harmonic generation and propagation, and I also compile all the information about the recollision model that is necessary to introduce the method of analysis of high-harmonic spectra. The method itself is described in section 2.2. It is important to take pulse chirp into account, when applying this method, this issue is discussed in section 2.2.1. The applicability of the method, its advantages and disadvantages are discussed in section 2.2.2

2.1 Simulation of generation and propagation of high-order harmonics

Theoretical investigations of high-harmonic generation (HHG) are hardly possible without computer simulations. The first *ab-initio* calculations of HHG in a rare gas taking account of both the single-atom response and propagation effects in a non-perturbative way were reported in Ref. [45]. Since then different aspects of the process were explored by either solving the time-dependent Schrödinger equation or employing the semi-classical theory of Lewenstein *et. al.* [47]. The former approach is more accurate and it allows to investigate effects inaccessible to the semi-classical model (e.g. diffusion of electronic wavepackets, quantum interferences, HHG by rescattered electrons etc), but numerical solution of the Schrödinger equation is much more time consuming in comparison with semi-classical calculations. This becomes especially important if spatial effects play an important role, so that generation and propagation of high harmonics in three spatial dimensions has to be simulated.

In my work I used an improved version of the code which was first presented in Ref. [53]. The code simulates propagation of an ultrashort laser pulse in a gas undergoing ionisation. A three-dimensional model is implemented, where cylindrical symmetry is assumed for the transverse beam profile. Simultaneously, the code simulates generation and propagation of high harmonics. The atomic dipole response to the laser field is calculated by an extension of the model of Lewenstein

et. al. [47, 53], using accurate static-field ionisation rates obtained from numerical fully quantum-mechanical calculations [54]. Harmonic absorption and diffraction are taken into account, as well as the geometrical (Gouy) phase shift, dispersion introduced by free electrons, ionisation energy losses, and the delay due to the refractive index of neutral atoms. The one-dimensional version of the code was originally written by T. Brabec and G. Tempea [19], then it was generalised to the three-dimensional case by N. Milosevic [55]. My own contribution to the code was, first of all, in making it substantially faster and employing more accurate numerical schemes. I included diffraction of harmonics into the propagation part of the code, implemented the Crank-Nicholson scheme (described in the appendix A.2), and improved the algorithm of birth-time calculation.

In order to test the code a comparison was performed with purely quantum-mechanical calculations [56]. Fig. 2.2 shows a good concordance between the two calculations, especially if the harmonic signal is integrated over the transverse beam profile. The laser pulse in these calculations was specified by the vector potential

$$A(t) = A_0 \operatorname{sech}\left(\frac{2.356t + \pi/4}{2\pi}\right) \sin(2.356t),$$

where the time t is measured in femtoseconds (the FWHM of the pulse is approximately 5 fs), a Gaussian beam profile with the beam waist $w_0 = 61 \mu\text{m}$ was assumed, the peak intensity of the pulse was taken to be equal to $5 \times 10^{14} \text{ W/cm}^2$.

2.1.1 The recollision model of high-harmonic generation

The model of Lewenstein [47] is based on the so-called recollision scheme: an electronic wave packet is detached from the atom by tunnelling around each oscillation peak of a laser electric field that is strong enough to substantially suppress the effective binding potential; depending on the initial conditions the electron can return to the point where it was released where it recombines with its parent ion and releases its excess energy in bremsstrahlung-like radiation. This model is applicable to a regime where bound states are not important (low-frequency high-intensity laser field) and by now the model is well established. Nevertheless, it has

Harmonic Spectra

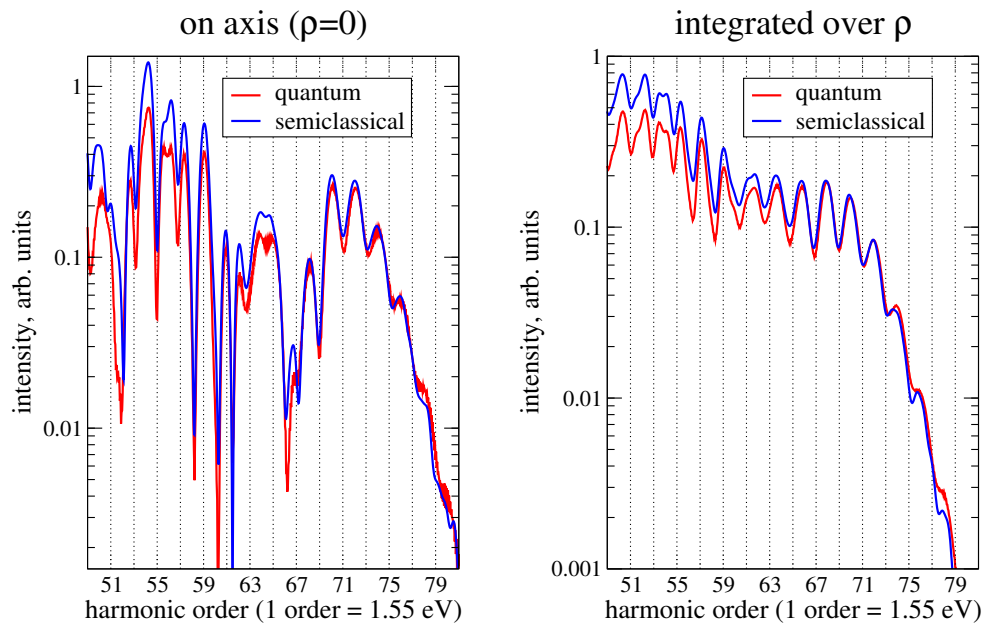


Figure 2.2: Harmonic spectra calculated in the fully quantum-mechanical model (red curves) and in the semiclassical model (blue curves). The left panel shows the power spectrum of the second derivative of the single-atom dipole response $|\mathcal{F}[\ddot{d}(t)]|^2$, while the right panel shows the power spectrum integrated over a range of intensities of the laser pulse, accounting in such a way for a particular transverse profile of the laser beam. Parameters of the calculations are listed in the text.

some subtleties that are very important for the research presented in the thesis. So, I will shortly describe the model along the lines of Ref. [57].

The dipole moment responsible for high-harmonic generation is obtained as a product of three probability amplitudes (atomic units are used throughout this section):

$$d(t) = \text{Re} \left[\sum_{t_b} \frac{1}{\sqrt{i}} a_{ion}(t_b) a_{pr}(t_b, t) a_{rec}(t) \right], \quad (2.2)$$

where t_b stands for a particular birth time of the electron, which recollides with its parent ion at the moment t . The “ionisation”, “propagation”, and “recombination” probability amplitudes in Eq. (2.2) are given by

$$a_{ion}(t_b) = \sqrt{\frac{dn(t_b)}{dt}}, \quad (2.3)$$

$$n(t) = n_0 \left(1 - \exp \left[- \int_{-\infty}^t dt' w \{ E_I(t') \} \right] \right), \quad (2.4)$$

$$a_{pr}(t_b, t) = \left(\frac{2\pi}{t - t_b} \right)^{3/2} \frac{(2W_b)^{1/4}}{E_I(t_b)} \exp[-iS(t_b, t)], \quad (2.5)$$

$$S(t_b, t) = \int_{t_b}^t dt' \left(\frac{1}{2} [p(t_b, t) - A_I(t')]^2 + W_b \right), \quad (2.6)$$

$$a_{rec}(t) = \frac{p(t_b, t) - A_I(t)}{[2W_b + \{p(t_b, t) - A_I(t)\}^2]^{3/2}}, \quad (2.7)$$

$$A_I(t) = - \int_{-\infty}^t dt' E_I(t'), \quad (2.8)$$

$$p(t_b, t) = \frac{1}{t - t_b} \int_{t_b}^t dt' A_I(t'), \quad (2.9)$$

where $n(t)$ is the free-electron density, $w\{E_I\}$ is the ionisation rate at the electric field E_I , n_0 is the initial concentration of neutral atoms, W_b is the ionisation potential, p is the classical momentum of the electron. The instant of birth t_b as a function of time t is determined by solution of the algebraic equation

$$p(t_b, t) - A_I(t_b) = 0. \quad (2.10)$$

For a fixed time t this equation can have several solutions, which are included into the sum in Eq. (2.2).

2.1.2 Photon energies

It is convenient to regard oscillations of the dipole moment (2.2) as radiation of photons, where the photon energy depends on the recollision time. Since the only fast-oscillating term in equations (2.3-2.9) is $\exp[-iS(t_b, t)]$, the frequency is given by the derivative dS/dt at the moment of recollision. From (2.6) we have

$$\frac{dS}{dt} = \left(\frac{1}{2}[p(t_b, t) - A_I(t)]^2 + W_b \right) - \frac{dt_b}{dt} \left(\frac{1}{2}[p(t_b, t_b) - A_I(t_b)]^2 + W_b \right). \quad (2.11)$$

According to (2.10) $p(t_b, t)$ is equal to $A_I(t_b)$ provided that t is the recollision moment, and from (2.9) we conclude that

$$p(t_b, t_b) = \lim_{t \rightarrow t_b} \frac{1}{t - t_b} \int_{t_b}^t dt' A_I(t') = A_I(t_b). \quad (2.12)$$

Further, from (2.8), (2.9), and (2.10), we obtain

$$\frac{dt_b}{dt} = \frac{A_I(t) - A_I(t_b)}{A_I'(t_b)(t - t_b)} = -\frac{A_I(t) - A_I(t_b)}{E_I(t_b)(t - t_b)}. \quad (2.13)$$

With this expression and Eq. (2.11) the instantaneous frequency of dipole oscillations (the photon frequency) can be written as

$$\omega(t_b, t) = \frac{dS}{dt} = \varepsilon_{kin} + W_b \cdot \left(1 + \frac{A_I(t) - A_I(t_b)}{E_I(t_b)(t - t_b)} \right), \quad (2.14)$$

where

$$\varepsilon_{kin} = \frac{1}{2}[p(t_b, t) - A_I(t)]^2 = \frac{1}{2}[A_I(t) - A_I(t_b)]^2 \quad (2.15)$$

is the kinetic energy of the electron at the recombination moment. This result is rather surprising, because the photon energy is not simply the kinetic energy of the electron plus the ionisation potential, but it also contains the correction term, which is basically explained by the connection between the birth and the recombination times of an electron. Mathematically speaking, the term appears, because the derivative dt_b/dt in Eq. (2.11) is not equal to zero. It does not imply any contradiction with the energy conservation law, because equation (2.14) does not determine the energy radiated in the form of harmonic radiation, it only gives a semiclassical value for the most probable photon energy.

Let us estimate the correction term for some typical parameters. Taking the harmonic energy $\epsilon_{kin} = 100 \text{ eV} = 3.7 \text{ a.u.}$, the electric field at the birth time $E_l(t_b) = 6 \times 10^{10} \text{ V/m} = 0.1 \text{ a.u.}$, and $t - t_b = 1.6 \text{ fs} = 70 \text{ a.u.}$ we obtain

$$\left| \frac{A_l(t) - A_l(t_b)}{E_l(t_b)(t - t_b)} \right| = \frac{\sqrt{2\epsilon_{kin}}}{|E_l(t_b)|(t - t_b)} = 0.4.$$

So, the correction term in Eq. (2.14) is important for interpretations of high-harmonic simulations.

The correctness of formula (2.14) has been confirmed by the full quantum-mechanical calculations. Fig. 2.5 on page 51 shows such an example, in which the photon energies calculated with Eq. (2.14) are compared to the time-frequency analysis of a quantum-mechanical calculation (a detailed discussion of the time-frequency analysis is given in section 2.1.4). Fig. 2.5 also shows that the recollision model gives a consistent explanation of high harmonic generation throughout the laser cycle.

The highest-order harmonics form the so-called “cut-off” region in the harmonic spectrum where radiation intensity rapidly decreases with the frequency. It is well known (Ref. [47]) that for long laser pulses the cut-off energy is approximately equal to

$$\epsilon_{\text{cutoff}} = W_b + 3.17 \frac{E_0^2}{4\omega_l^2}, \quad (2.16)$$

where E_0 is the amplitude of the laser field. Surprisingly, Eq. (2.16) gives accurate results even for few-cycle pulses if one replaces E_0 with the amplitude of the electric field half cycle, within which the corresponding electron recollides with the parent ion. So, the semiclassical cut-off energy for the 5-fs Gaussian pulse shown in Fig. 2.3 is equal to 113 eV. With $E_0 = 5.86 \times 10^{10} \text{ V/m} = 0.114 \text{ a.u.}$, $\omega_l = 2.36 \text{ fs}^{-1} = 0.057 \text{ a.u.}$, and the ionisation potential of neon $W_b = 21.6 \text{ eV} = 0.79 \text{ a.u.}$ the cut-off energy calculated with the aid of Eq. (2.16) is equal to $\epsilon_{\text{cutoff}} = 108 \text{ eV}$, which differs by only 5% from the exact value.

It is also important to understand that each photon energy is generated at most twice during a laser half-cycle, corresponding to “short” and “long” trajectories of the classical picture [47, 58]. This is illustrated in Fig. 2.3. There are a few effects

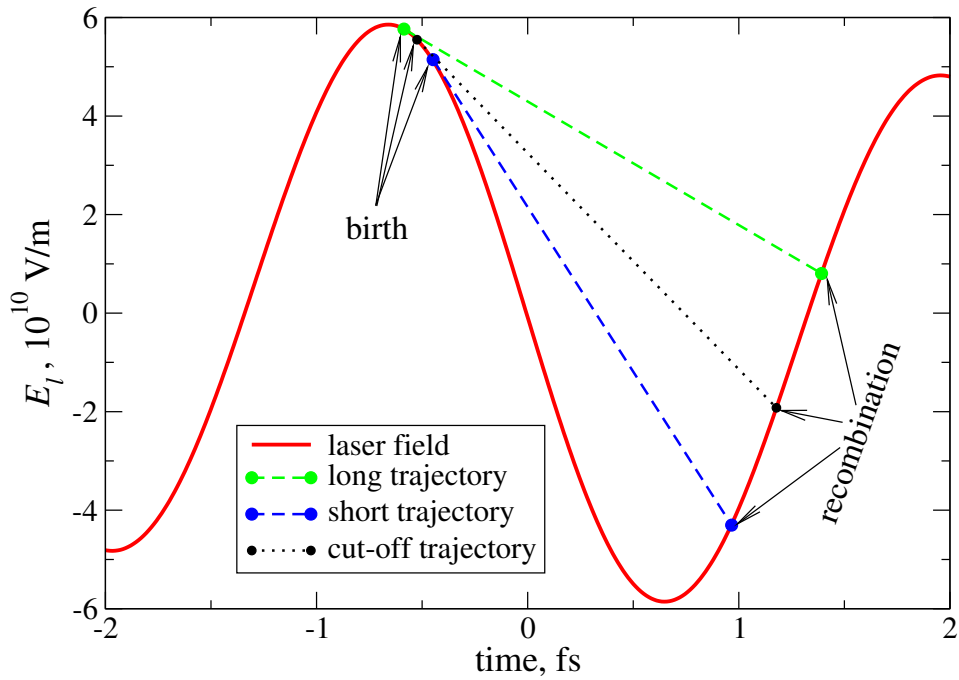


Figure 2.3: Detachment and recombination of electrons. Both the short and long electron trajectories result in the same kinetic energy of the electron at the recombination moment, but the phase change of an electronic wavepacket between the birth and recombination moments is more sensitive to the laser field, if the electron follows the long trajectory. The trajectory of the maximal electron's kinetic energy is plotted as the black broken line (in this case the short and long trajectories become identical).

which make the contribution from short trajectories much stronger in comparison with the contribution from long trajectories [58]. First, an electronic wave packet expands as it is moving in the continuum, thus the probability of hitting the parent ion is lower for longer trajectories. Second, the phase of radiated photons depends on the intensity of the laser pulse, so it depends on the distance to the axis of the laser beam. For longer trajectories this dependence is stronger than for short ones, and this effectively suppresses the contribution from the long trajectories when the harmonic spectrum is integrated over the beam profile (Fig. 2.4). Third, short trajectories are found to experience more favourable phase-matching conditions, so that propagation through a target medium further attenuates the long-trajectory signal.

2.1.3 Simulated harmonic spectra

At this point we have to clarify what we call “harmonics”. In the domain of the perturbative non-linear optics the n th harmonic of the electric field oscillating with the frequency ω_0 oscillates with the frequency $n\omega_0$. In particular, only harmonics with an odd value of n can be generated in an inversion symmetric medium. The situation changes dramatically in the strong-field regime, where the perturbative approach is no longer applicable. If a laser pulse is as short as a few optical cycles, then the peaks in the harmonic spectrum are no longer fixed to multiples of the central frequency of the laser pulse. This behaviour appeared in numerical simulations [51] and was observed in a recent experiment with phase-stabilised pulses [A4]. Strictly speaking, the high-frequency radiation generated by an ultrashort laser pulse in the strong-field region may not be called “harmonic radiation”. Nevertheless, there is currently no alternative name for it. To remain consistent with the current conventions in this field of science, I call this radiation “harmonic” and the physical process behind it the “high harmonic generation”. One should keep in mind though, that these harmonics have some very special properties, discussed below.

One of these properties, which attracted attention of researchers, is the influ-

ence of the CE phase φ_{CE} of the laser pulse on the structure of harmonic spectra [40]. It was observed that the frequencies of “harmonics” are shifted when the CE phase is changed, in spite of the fact that this change does not affect the spectrum of the laser pulse. This can be easily understood if one notices that if a laser pulse is so short, that the φ_{CE} begins to play an important role, the sine- and cosine-pulses show different behaviour under the time-reversal $t \rightarrow -t$: the field of a cosine-pulse remains invariant, while the field of a sine-pulse changes its sign (here we consider bandwidth-limited pulses with symmetric envelopes). The cosine pulse therefore has a preferred orientation of the electric field—the orientation of the maximal field peak, which breaks the symmetry of field orientations usually assumed in optics. The violation of symmetry has a striking manifestation in the high-harmonic spectrum of a cosine pulse: the rule that harmonic peaks only appear at odd multiples of the fundamental frequency is violated.

Another interesting property of high harmonics is the structure of the so-called cut-off region—the farthest part of spectrum, where the spectral intensity rapidly decreases with photon energy. In Fig. 2.2 the cut-off region spans approximately over harmonic orders 73-80. It was found [40] that this region can be either smooth or modulated depending on the CE phase of a few-cycle laser pulse: a cosine-pulse generates a smooth cut-off without any harmonic structure, while a sine-pulse is associated with a regularly modulated cut-off. This behaviour is clearly seen in Fig. 2.4. The two upper panels show the intensity of the harmonic field on axis $I_h(\omega, \rho = 0)$ for a very short propagation distance and for the distance, where phase-matching effects come into play ($L = 2 \text{ mm}$ is approximately 1/4 of the coherence length near $\hbar\omega = 100 \text{ eV}$). The lower panels show the corresponding spectra integrated over the radial coordinate:

$$\tilde{I}_h(\omega) = \int_0^\infty \rho I_h(\omega, \rho) d\rho. \quad (2.17)$$

In these pictures one can also see that the integrated spectra look much more regular than the spectra on axis, and they become even more regular after propagation. Both effects are explained by the effective suppression of long electron trajectories [51, 59]. On the one hand, Fig. 2.4 demonstrates that it is absolutely

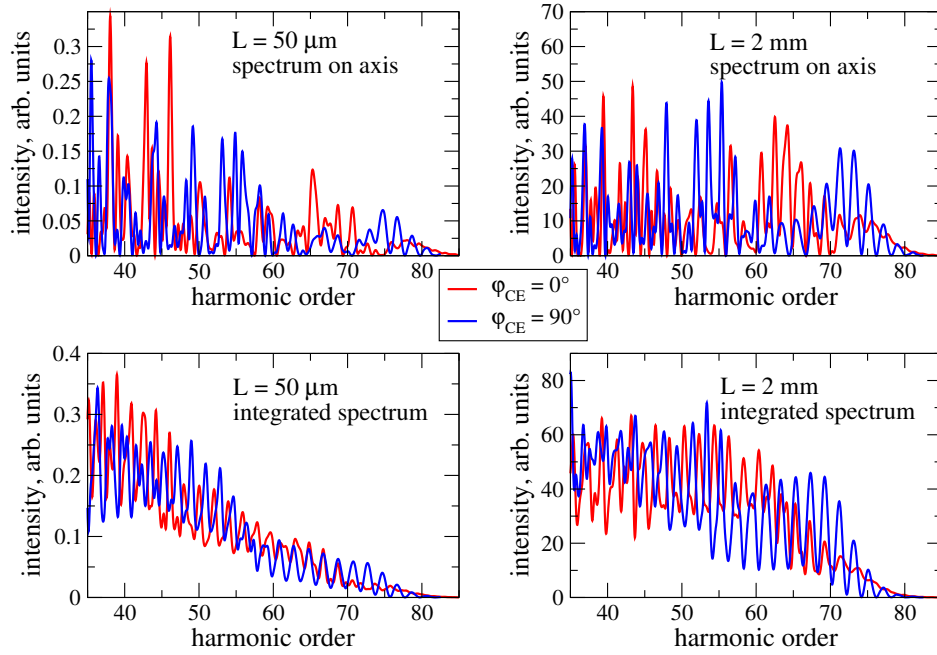


Figure 2.4: Harmonic spectra obtained by semi-classical simulations for different propagation distances and two different values of the CE phase: $\varphi_{\text{CE}} = 0^\circ$ (red curves) and $\varphi_{\text{CE}} = 90^\circ$ (blue curves). Integration over the radial coordinate makes spectra much more regular (this is explained by the effective suppression of the long electronic trajectory). The HHG was simulated for neon at 100 mbar, 5-fs Gaussian laser pulse with the beam waist of $61 \mu\text{m}$ and the central wavelength $\lambda_0 = 750 \text{nm}$ that corresponds to the photon energy of 1.65 eV. The cut-off region covers harmonic orders 73-80.

necessary to consider spatial effects to analyse harmonic spectra, on the other hand, we will soon see that the classical picture of photon energies can still be used to interpret harmonic spectra, provided that one removes the long trajectories from the picture.

2.1.4 Time-frequency analysis

A very useful tool which gives us insight into the HHG process is the time-frequency analysis. In this analysis a time-dependent signal [in our case, the electric field of the harmonic radiation $E_h(t)$ or the second derivative of the atomic dipole $\ddot{d}(t)$] is multiplied by a narrow window function $g(t)$ and the result is Fourier transformed. We used a Gaussian window with the width chosen to be a small fraction of the laser optical cycle, but still longer than the period of harmonic oscillations: $T = 0.05 \times 2\pi/\omega_l$. Fig. 2.5 shows the time-frequency analysis of a dipole response calculated in the full quantum-mechanical model:

$$H(\omega, t) = \left| \mathcal{F}_{t'}[\ddot{d}(t')e^{-(t-t')^2/T^2}] \right|^2. \quad (2.18)$$

In the central panel one sees several harmonic radiation bursts, which we label by B_t with $t = -0.5, 0, 0.5$, and 1 referring to the approximate times where the lower energies of the burst are generated. The intensity of each B_t is proportional to the ionisation rate at the starting time t_b of the classical trajectory, which precedes recollision by typically $|t - t_b| \approx 1/2$ optical cycle. As ionisation is strongest for the peak field at $t = 0$, the burst $B_{0.5}$ has the highest intensity. The right panel of Fig. 2.5 shows the spectrum of the single-atom contribution to the harmonic radiation. It is interesting now to interpret the spectrum with the aid of the time-frequency analysis. At the highest photon energies (≈ 125 eV), there is only one single burst of high-harmonic radiation that is responsible for the smooth cut-off of the harmonic spectrum. At lower photon energies, there are contributions from several bursts, which modulate the spectrum. If the laser pulse is much longer than its central wavelength λ_0 , there will be many nearly identical bursts, with the phase changing by π from burst to burst. In the frequency domain this produces

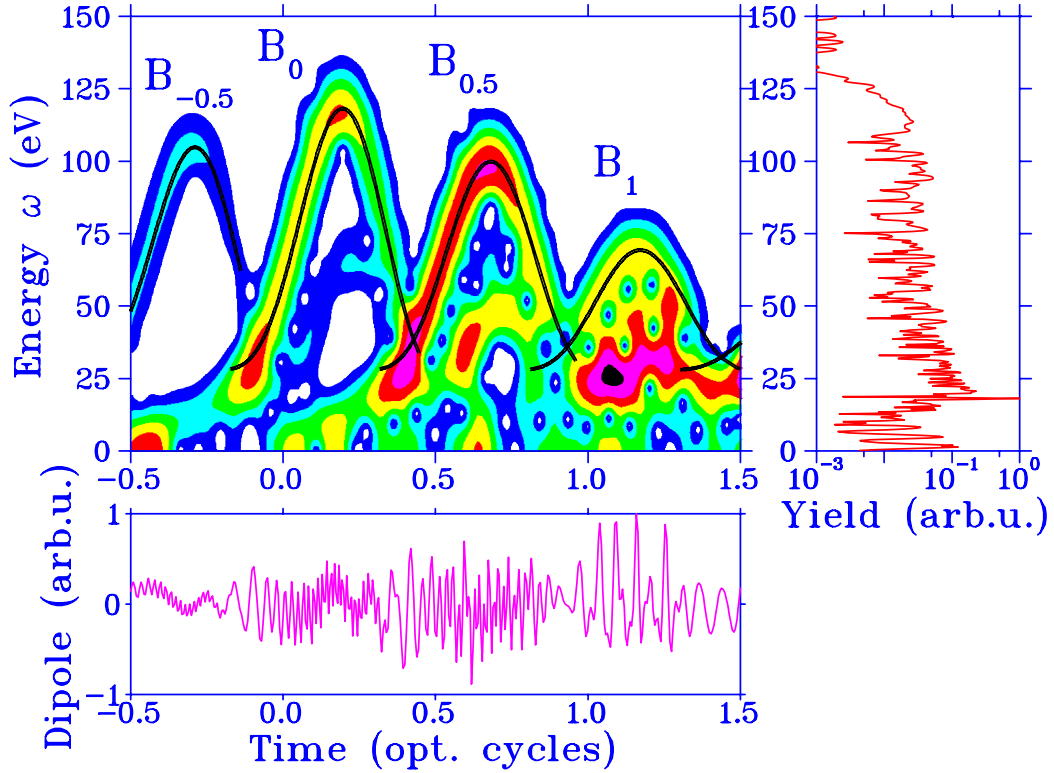


Figure 2.5: Time-frequency analysis of the dipole response of a neon atom to a strong short laser pulse. The box at the bottom shows the acceleration of the atomic dipole by a 5-fs laser pulse with sech envelope, central wavelength of 800 nm, and peak intensity of $5 \times 10^{14} \text{ W/cm}^2$. The box to the right shows the harmonic power spectrum. Solid lines in the time-frequency plot indicate harmonic energies calculated from equation (2.14).

the usual harmonic comb, in which the peaks are centred around odd multiples of $\omega_l = 2\pi c/\lambda_0$. The picture is different for few-cycle laser pulses. In this case only a few bursts contribute to the spectral part situated just below the cut-off. This creates a rather irregular modulation of harmonic spectra. In the next section it will be demonstrated that the information contained in this modulation is sufficient to retrieve the electric field of the highest peaks of a laser pulse as well as the CE phase of the pulse. This is the main finding presented in this chapter of my PhD thesis.

2.2 Advanced analysis of high-harmonic spectra

In section 2.1.4 it was demonstrated that the frequencies of the dipole response keep a detailed record of the laser field, which to a certain degree has to reappear in the harmonic power spectrum, except that information on the harmonic phase is lost and therefore no absolute times but only time-separations of the electric field peaks are reflected in the spectrum. One of the well known features, for example, is the modulation of the cut-off region in harmonic spectra: for a cosine laser pulse the cut-off is smooth, while for a sine pulse, it is modulated. This behaviour was exploited to make the first measurements of the CE phase [A4]. To perform such an experiment, ultimately short laser pulses are necessary. Apart from that, the photon flux in the cut-off region is rather weak. This stimulated the research to find a way to extract some useful information from the part of the harmonic spectrum, which precedes the cut-off region.

In an experiment, one does not record the signal from a single atom, but from an ensemble of atoms distributed across the focal region of the laser. Phase matching effects, the spatial laser intensity profile, and the focal distortions of the laser wave front must be taken into account. By simulating the three-dimensional propagation of laser pulse and harmonics we verified that phase matching effects do not distort the harmonic image, provided one uses a long laser focus and operates well below the regime, where harmonic generation saturates (see A.3 in the ap-

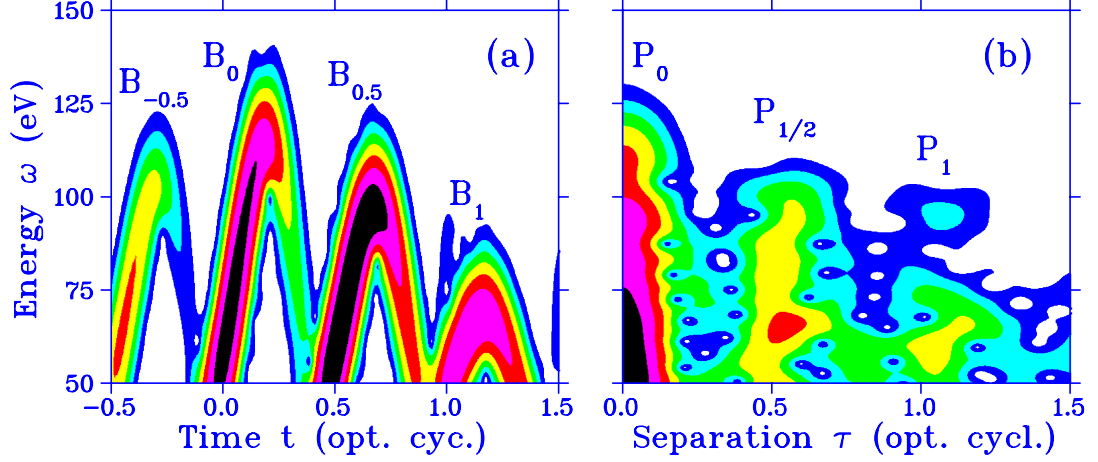


Figure 2.6: Time-frequency plot of electric field on axis (a) and power spectrum (b) generated in a gas volume after propagation over 10 cm. (Pulse parameters as in Fig 2.5.)

pendix). Under these conditions the time-frequency plot of HHG can be partially recovered from the harmonic power spectrum $h(\omega)$. Applying a frequency-time analysis to $h(\omega)$

$$Z(\tau, \omega) = \left| \mathcal{F}_{\omega'} [h(\omega') e^{-(\omega - \omega')^2 / \Omega^2}] (\tau) \right|^2, \quad (2.19)$$

we can determine the time-separation of radiation bursts contributing to the harmonic spectrum at a given energy ω . The width of the Gaussian window function Ω must be large enough to enclose a few harmonic orders, and at the same time it should be as small as possible to get better resolution. Acceptable performance is achieved with $\Omega = 3\omega_l$. In Fig. 2.6 the time-frequency analysis of the on-axis dipole field and the frequency-time analysis of the harmonic power spectrum are shown. The harmonic pulse for this figure was obtained with the aid of three-dimensional HHG simulations for a 2 mm neon target ($p = 100$ mbar) followed by propagation over 10 cm in vacuum. Both, the propagation in the gas and the diffraction in vacuum made the time-frequency plot more regular, as compared to the single-atom response in Fig. 2.5, because the contributions of the classical short recollision trajectories are favoured by phase matching. The laser pulse for this simulation has a sech time-envelope with 5-fs FWHM and peak intensity of

$5 \times 10^{14} \text{ W/cm}^2$, the central wavelength is equal to 800 nm. The focus of the Gaussian beam was placed in the centre of the gas volume, the beam waist was $72 \mu\text{m}$ resulting in the confocal parameter of 2 cm. The frequency-time analysis of the harmonic power spectrum shows distinct peaks at time-separations $\tau = 0$, $1/2$, and 1 optical cycles, which we label by P_τ . There is a close correspondence between the radiation bursts B_τ in the analysis of the dipole moment and the peaks P_τ . The cut-off energy of $P_0(\omega)$ coincides with the cut-off of B_0 . The frequency dependence of $P_{1/2}$ and P_1 reflects the successive appearance of contributions with time separations $1/2$ and 1, respectively. $P_{1/2}$ is predominantly due to the pair of bursts $(B_0, B_{0.5})$ and first appears at the maximal energy of $B_{0.5}$. At higher energies a weak signal in P_1 is generated by the pair $(B_{-0.5}, B_{0.5})$, but the stronger contribution at lower frequencies is due to (B_0, B_1) .

Several characteristic features of short pulse high harmonic spectra can be understood from time-frequency and frequency-time plots. Fig. 2.6 shows that in any given range of harmonic frequencies, the separation between peaks is given by the time-separation of the two dominant bursts of radiation. It was noted earlier [40] that peaks observed in short pulse harmonic spectra are not located at odd multiples of the fundamental frequency, since the time-separation of high-frequency radiation deviates from half the optical period: $P_{1/2}$ in Figure 2.6 shifts to larger τ with increasing ω . Another feature appearing in short pulse high harmonic spectra is an apparent phase-jump of modulations of the harmonic spectrum separating groups of “odd harmonics” from “even harmonics”. These jumps can be associated with the end of one of the two dominant bursts and takeover by a new pair of bursts.

For a quantitative analysis one can eliminate the τ -coordinate by defining the integrated peaks

$$P_\tau(\omega) = \int_{\tau-1/4}^{\tau+1/4} Z(\omega, \tau') d\tau'. \quad (2.20)$$

Figure 2.7 compares the cut-off energies of $P_{1/2}$ and P_1 with the second and third highest classical recollision energies as a function of φ_{CE} . For this picture the cut-off was defined as the energy, where the height of an integrated peak drops to 8%

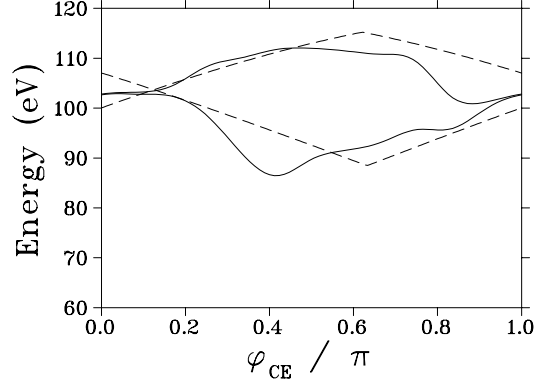


Figure 2.7: Comparison of the peak cut-off energies for $P_{1/2}$ (upper curve) and P_1 (lower curve) with the cut-off energies from the recollision model (dashed) as a function of φ_{CE} .

of the first preceding maximum. The recollision model and the numerical simulation agree within $\lesssim 10\%$. The deviations from the classical recollision energies are brought about by interference of contributions of bursts of comparable height to $P_{1/2}$ and P_1 , which blurs the cut-off.

The frequency-time analysis of the harmonic spectrum generalises the phase-measurement method proposed by de Bohan *et al.* [40], where the structure of the harmonic spectrum near the cut-off was used to distinguish sine- from cosine-pulses. In the terminology introduced here, the main result of Ref. [40] is that for a sine-pulse the cut-off energies of P_0 and $P_{1/2}$ become nearly equal, while for a cosine pulse the difference between the cut-off energies is maximal, leading to a strongly modulated and a smooth cut-off spectrum, respectively. By exploiting a much larger part of the harmonic spectrum, the present method provides more detail on the pulse and in particular higher sensitivity to φ_{CE} . While P_0 and $P_{1/2}$ are both related to bursts B_t at times t near the centre of the laser pulse, whose height and intensity vary little with φ_{CE} , the peak P_1 involves a third burst nearer to the slope of the laser pulse with greater variability with φ_{CE} . For that reason our method is applicable to longer pulses with durations up to $\lesssim 7$ fs. Figure 2.8 shows as an example the φ_{CE} -dependence of the quantity

$$R = \int_{\omega_{0.5}}^{\omega_1} P_1(\omega) d\omega / \int_{\omega_{0.5}}^{\omega_1} P_{1/2}(\omega) d\omega \quad (2.21)$$

for pulse durations between 6 and 8 fs. The frequency range $[\omega_{0.5}, \omega_1]$ is given by the maximal semiclassical energies for $B_{0.5}$ and B_1 , respectively, as obtained from Eq. (2.16). The ratio R indicates, to which extent two bursts separated by $\tau = 1$ contribute to the harmonic spectrum. It shows a pronounced maximum near the cosine-pulse and can therefore be used to fix φ_{CE} .

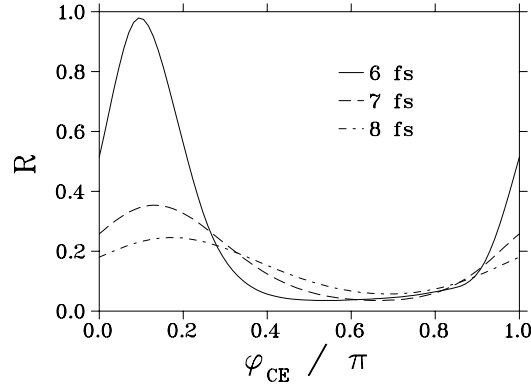


Figure 2.8: Modulation of intensity ratio R at period $\tau = 1/2$ and $\tau = 1$ for pulse durations between 6 and 8 fs FWHM.

2.2.1 High-harmonic imaging of chirped laser pulses

A possible pulse chirp must be taken into account when deducing the electric field from the harmonic cut-off energies. Small chirp is a prerequisite of generating few-cycle pulses, but even pulses as short as 5 fs may carry a non-negligible chirp. As the recollision energies, given by Eq. (2.15), depend on the laser field preceding the recollision moment by more than half an optical period, changes of the effective field period lead to corresponding relative changes in harmonic energy.

To explore the influence of chirp analytically, it is necessary to assume a certain pulse shape. It is convenient to choose the parabolic pulse

$$E_l(t) = E_0(1 - \alpha t^2) \cos(\omega_l t + \varphi_{\text{CE}} + \gamma t^2). \quad (2.22)$$

This is a good approximation, since the nonlinear phenomena that we are discussing occur close to the top of the pulse, where any pulse shape can be approx-

imated by a parabola.

Since the most striking manifestation of the CE phase in harmonic spectra is the structure of the cut-off region, it would be interesting to find an analytical expression for φ_{CE} corresponding to either the smoothest or the most modulated cut-off generated by a chirped laser pulse. Let us denote the first phase by φ_{sco} , and the second one by φ_{mco} , where the abbreviations ‘‘sco’’ and ‘‘mco’’ stand for ‘‘smooth cut-off’’ and ‘‘modulated cut-off’’, respectively. In fact, these two phases differ by $\pi/2$, what can be shown analytically and was verified numerically. The phase φ_{mco} can be derived using the following simple model. The deepest modulation of the cut-off region means that the highest harmonic energies are generated in two bursts of radiation separated by half an optical cycle of the laser pulse. The highest energies of the bursts are approximately given by Eq. (2.16), where the amplitude of the electric field E_0 and the frequency ω_l must be replaced with the amplitude and the instantaneous frequency of the electric field half cycle, within which the harmonic burst is generated. The peaks of the field (2.22) are situated at the times

$$t_n = -\frac{\omega_l}{2\gamma} \left(1 - \sqrt{1 - \frac{4\gamma(\varphi_{\text{CE}} - \pi n)}{\omega_l^2}} \right) \approx \frac{\pi n - \varphi_{\text{CE}}}{\omega_l}, \quad (2.23)$$

where the chirp γ is assumed to be so small that

$$\frac{4\gamma(\varphi_{\text{CE}} - \pi n)}{\omega_l^2} \ll 1. \quad (2.24)$$

The maximal energy of the n th burst according to Eq. (2.16) is given by

$$\varepsilon_n = W_b + 3.17 \frac{E_0^2(1 - \alpha t_n^2)^2}{4(\omega_l + 2\gamma t_n)^2}. \quad (2.25)$$

Two central harmonic bursts have equal highest photon energies if either $\varepsilon_0 = \varepsilon_1$ or $\varepsilon_{-1} = \varepsilon_0$. One of these conditions is fulfilled if the CE phase is equal to

$$\varphi_{\text{mco}} = \frac{\pm \pi \gamma + \omega_l^2 - \sqrt{\frac{1}{\alpha} (\gamma^2 (\pi^2 \alpha - 4\omega_l^2) + \alpha \omega_l^4)}}{2\gamma} \approx \pm \frac{\pi}{2} + \gamma \left(\frac{1}{\alpha} - \frac{\pi^2}{4\omega_l^2} \right), \quad (2.26)$$

where the chirp was, once again, considered to be small:

$$\frac{\gamma^2 (\pi^2 \alpha - 4\omega_l^2)}{\alpha \omega_l^4} \ll 1. \quad (2.27)$$

The term $\pi^2/(4\omega_l^2)$ can be neglected in Eq. (2.26) because $\pi^2/(4\omega_l^2) \ll 1/\alpha$ for pulses longer than one optical cycle. The same argument allows to unify the conditions (2.24) and (2.27) into

$$\gamma \ll \omega_l \sqrt{\alpha} \approx \frac{\omega_l}{\text{FWHM}}. \quad (2.28)$$

Numerical calculations based on the recollision model described in sections 2.1.1 and 2.1.2 confirm that φ_{mco} linearly depends on the chirp γ and that $\varphi'_{\text{mco}}(\gamma) = 1/\alpha$ (Fig. 2.9). However, a certain value $\Delta\varphi_{\text{CE}}$ must be added to the phase given

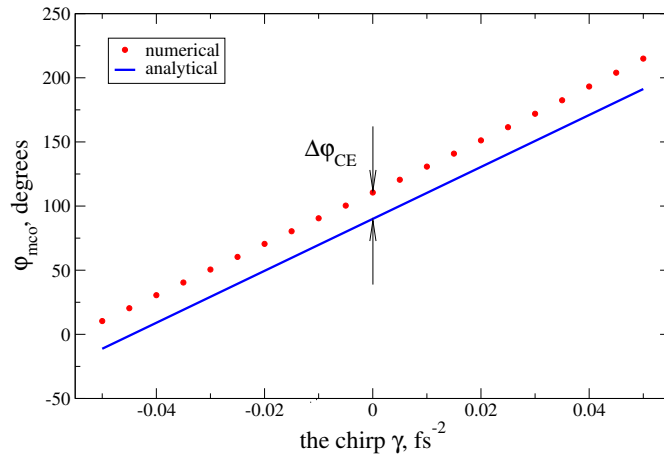


Figure 2.9: The CE phase corresponding to the strongest modulation of the cut-off region in the high-harmonic power spectrum generated by a 7-fs Gaussian laser pulse with the peak intensity $5 \times 10^{14} \text{ W/cm}^2$. The numerical calculations are based on Eq. (2.14) with $W_b = 21.6 \text{ eV}$ (neon). The solid curve shows the result of the simplified analytical treatment: $\varphi_{\text{mco}} = (\pi/2 + \gamma/\alpha)180^\circ/\pi$. The numerical simulations confirm that Eq. (2.26) correctly predicts the slope of $\varphi_{\text{mco}}(\gamma)$, but the phase must be corrected by a certain shift $\Delta\varphi_{\text{CE}}$.

by Eq. (2.26) in order to correctly determine the phase φ_{mco} yielding the strongest modulation of the cut-off region:

$$\varphi_{\text{mco}} = \pm \frac{\pi}{2} + \frac{\gamma}{\alpha} + \Delta\varphi_{\text{CE}}. \quad (2.29)$$

The numerical simulations also show that $\Delta\varphi_{\text{CE}}$ is practically independent of pulse shape and duration, but it depends on the pulse intensity as well as on the ioni-

sation potential W_b . In table 2.1 a few values of $\Delta\varphi_{\text{CE}}$ are given for different peak intensities, where W_b is taken to be equal to the ionisation potential of neon (21.6 eV). It was verified numerically that the correction $\Delta\varphi_{\text{CE}}$ to φ_{sco} is the same

peak intensity, W/cm ²	$\Delta\varphi_{\text{CE}}$, degrees
3×10^{14}	25.2
4×10^{14}	22.8
5×10^{14}	21.4
6×10^{14}	20.4
7×10^{14}	19.7
8×10^{14}	19.2
9×10^{14}	18.8
1×10^{15}	18.4

Table 2.1: Correction to the CE phase φ_{mco} , which yields the most modulated cut-off region (the correction to the CE phase corresponding to the smoothest cut-off is the same). The calculations are based on Eq. (2.14) with $W_b = 21.6 \text{ eV}$ (neon).

as to φ_{mco} , so that

$$\varphi_{\text{sco}} = \frac{\gamma}{\alpha} + \Delta\varphi_{\text{CE}}. \quad (2.30)$$

2.2.2 Applicability of the method

The proposed method of analysis of high-harmonic spectra may be viewed as a generalisation of the cut-off analysis proposed in Ref. [40] and experimentally demonstrated in Ref. [A4]. The main advantage of the new method in comparison with its predecessor is the broader applicability range. Indeed, a sufficiently broad cut-off region can only be generated if pulse FWHM is as small as two optical cycles. If the central wavelength is $\lambda_0 = 800 \text{ nm}$, it corresponds to 5-fs pulses.

Another advantage of the proposed method is that it has relaxed phase-matching requirements. It is still necessary that the propagation length be a fraction of the coherence length, but we can benefit from the fact that the coherence

length is proportional to wavelength. Including into the analysis the part of harmonic spectra preceding the cut-off region, we increase the effective coherence length. Thus, it allows to use a larger propagation distance or a higher gas pressure, which increases the photon flux, shortens the observation time and improves the signal-to-noise ratio.

Chapter 3

Quantum theory of time-resolved Auger measurement

Recent advances in the generation of ultrashort laser pulses with controlled CE phase and application of these pulse to the generation of very short ($\lesssim 1$ fs) extreme ultraviolet (XUV) pulses have opened a new horizon in time-resolved spectroscopy. It was demonstrated that atomic inner-shell processes, which happen on a few femtosecond time scale, can be investigated by pump-probe experiments with the aid of state-of-the-art techniques [A2, 60]. This created a new field in physics research, which is now called “attophysics”.

Theory, however, lagged somewhat behind the exciting experimental achievements. There was no well-founded theory to analyse the Auger-decay pump-probe experiment described in Ref. [A2]. In traditional electron beam or synchrotron spectroscopy time-independent approaches are used (see [61] for a review). Time-dependent methods employing wave-packet dynamics as for Rydberg atoms or in femtochemistry are inappropriate for the Auger process, where only few discrete levels are involved. Approaches developed for atoms in strong fields do not address the question of time-resolved observation [62, 63]. The lack of an appropriate theoretical framework stimulated the research presented in this chapter.

3.1 Time-resolved measurement of Auger decay in krypton

In this section I briefly describe the pump-probe experiment [A2], which demonstrated the feasibility of time-resolved spectroscopy on the attosecond time scale and triggered the theoretical investigations described in the following sections. In this experiment a sub-femtosecond, 97-eV XUV pulse initiates an Auger process in krypton by ionising one of the inner-shell electrons and creating thus a transient hole state (Fig. 3.1). This state is not stable, so the atomic system tends to minimise its energy by filling the vacancy with an electron from an outer shell. The excess of binding energy is either carried away by a fluorescence photon or transferred via electrostatic forces to another (Auger) electron. The latter relaxation channel is most probable for light atoms and moderate binding energies of the inner-shell electron ($E_0 < 1 \text{ keV}$), which is the case with the Auger decay in krypton investigated in Ref. [A2] ($E_0 = 70 \text{ eV}$). The XUV pulse in this experiment serves as a pump pulse, while details of the Auger decay can be revealed if an additional “probe” pulse is used, which either accelerates or retards the Auger electron depending on the instant of time when the electron was released. This method is sometimes referred to as “attosecond streak camera” [64, 65]. In the considered experiment the probe pulse was a linearly polarised sub-7-fs laser pulse with the central wavelength $\lambda_0 = 750 \text{ nm}$ and the peak intensity in the range $10^{11} \div 10^{12} \text{ W/cm}^2$. At this intensity ionisation of the gas by the laser pulse is negligible, which is important for interpretation of pump-probe experimental results. The kinetic energy distribution of emitted electrons was measured with a time-of-flight spectrometer aligned parallel to the polarisation direction of the light pulse. In the experiment the distribution had a form of a deformed Auger line accompanied by a few sidebands generated by the probe pulse. The Auger electron spectrum was measured for different values of the delay between the XUV pulse and the laser pulse, then the measured data were analysed using a simple phenomenological model of the Auger decay. From the delay-dependence of the

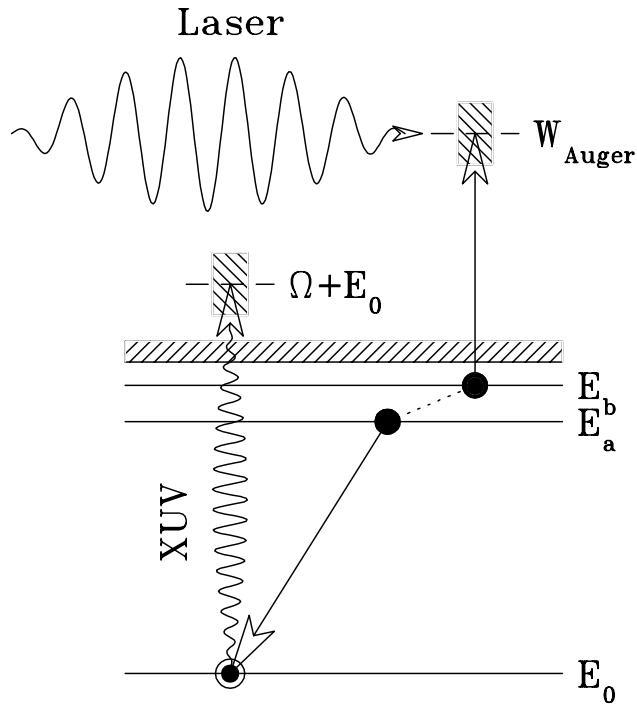


Figure 3.1: Scheme of the time-resolved Auger measurement: an XUV pulse with central frequency Ω removes a core electron from the energy level E_0 . The created vacancy is filled by an electron from the energy level E_a . The energy difference $E_a - E_0$ is carried away by the Auger electron from the energy level E_b , which is ejected to a continuum energy near $W_A = E_a + E_b - E_0$. Interaction of the Auger electron with the laser pulse can change the kinetic energy of the electron depending on the phase of the laser pulse at the moment of ionisation.

area of the first sideband, it was possible to retrieve the Auger decay time, which was found to be in close agreement with the value given by the width of the Auger line¹, giving thus the first evidence for time-resolved attosecond spectroscopy.

3.2 Derivation of basic equations

3.2.1 Essential states method

We consider a krypton atom in the electric field of two pulses linearly polarised in the same direction: an XUV pulse with the central wavelength of 10 nm and a few-cycle laser pulse with the central wavelength $\lambda_0 = 750$ nm. In general, each electron of the atom is to some extent influenced by the electromagnetic field of the pulses. As a first step of developing the analytical approach to the problem, let us limit our consideration to only three electrons participating in the given channel of the Auger decay. Furthermore, we assume that it's possible to construct the wavefunction $\Psi(\mathbf{r}_1, \mathbf{r}_2, \mathbf{r}_3; t)$ from only three electron states: the initial ground state $|g\rangle$, the core hole state $|h\rangle$, in which one inner-shell electron is ionised, and the doubly ionised final state $|f\rangle$. Such an approximation is known by the name “essential states method” [66]. We also assume that all the three states can be described as simple products of one-electron states of the form

$$|g\rangle = [|0, t\rangle|a, t\rangle - |a, t\rangle|0, t\rangle]|b, t\rangle, \quad (3.1a)$$

$$|h\rangle = [|p, t\rangle|a, t\rangle - |a, t\rangle|p, t\rangle]|b, t\rangle, \quad (3.1b)$$

$$|f\rangle = [|p, t\rangle|0, t\rangle - |0, t\rangle|p, t\rangle]|k, t\rangle. \quad (3.1c)$$

The momenta \mathbf{p} and \mathbf{k} are continuous three-dimensional vectors corresponding to the XUV photoelectron and the Auger electron momentum, respectively. The bound states $|0, t\rangle$, $|a, t\rangle$, and $|b, t\rangle$ denote orbitals that are occupied initially corresponding to the energies E_0 , E_a and E_b ; their time-dependence consists only in the phase oscillations $\exp(-itE_\alpha)$, where $\alpha = 0, a, b$ [see (3.5a-3.5c) below]. The

¹From the spectroscopic measurements $\Gamma = 84 \pm 10$ meV, which corresponds to decay time equal to 7.8 fs; the analysis of the area of the first sideband gives the decay time equal to $7.9_{-0.9}^{+1.0}$ fs.

continuum states $|\mathbf{p}, t\rangle$ and $|\mathbf{k}, t\rangle$ are time-dependent Volkov solutions for the free motion of an electron in the XUV field and the laser field, respectively. Antisymmetrisation is only essential to exclude the de-excitation $|a\rangle \rightarrow |0\rangle$ before the state $|0\rangle$ is vacated and was therefore omitted for the state $|b\rangle$.

The next step is to put down the time-dependent Schrödinger equation. Employing the atomic units ($\hbar = m_e = e^2 = 1$) we write

$$i\frac{\partial}{\partial t}\Psi(\mathbf{r}_1, \mathbf{r}_2, \mathbf{r}_3; t) = \hat{H}\Psi(\mathbf{r}_1, \mathbf{r}_2, \mathbf{r}_3; t). \quad (3.2)$$

The Hamiltonian in this equation is also subject to approximations. To take only the most important effects into consideration, we assume that

- each of the three electrons moves in an effective potential created by the nucleus and the rest of electrons;
- the Hamiltonian is only symmetric with respect to electrons 1 and 2;
- there is no direct interaction between electrons 1 and 2;
- electrons 1 and 3 as well as electrons 2 and 3 interact via the Coulomb force with the potential energy $U_{ab}(\mathbf{r}_j - \mathbf{r}_3) = 1/|\mathbf{r}_j - \mathbf{r}_3|$, $j = 1, 2$;
- electrons 1 and 2 only feel the XUV field $\mathcal{E}_x(t)$, while electron 3 only feels the laser field $\mathcal{E}_l(t)$.

With these approximations the Hamiltonian can be written in the following form:

$$\begin{aligned} \hat{H}(t) = & -\frac{1}{2}\Delta_1 + U_a(\mathbf{r}_1) + U_{ab}(\mathbf{r}_1 - \mathbf{r}_3) - \mathcal{E}_x(t)z_1 - \\ & -\frac{1}{2}\Delta_2 + U_a(\mathbf{r}_2) + U_{ab}(\mathbf{r}_2 - \mathbf{r}_3) - \mathcal{E}_x(t)z_2 - \frac{1}{2}\Delta_3 + U_b(\mathbf{r}_3) - \mathcal{E}_l(t)z_3 \end{aligned} \quad (3.3)$$

with the Laplacians Δ_j , $j = 1, 2, 3$ acting on the respective electron coordinates \mathbf{r}_j . The potentials U_a and U_b are effective single-electron potentials (electron 3 may feel a different binding potential than electrons 1 and 2). The laser pulse and the XUV pulse are represented by their electric fields $\mathcal{E}_l(t)$ and $\mathcal{E}_x(t)$, the fields are assumed to be polarised in the z -direction.

Since we assumed that the wavefunction $\Psi(\mathbf{r}_1, \mathbf{r}_2, \mathbf{r}_3; t)$ can be constructed from the $|g\rangle$, $|h\rangle$, and $|f\rangle$ states, it is reasonable to make the following ansatz for the solution of the time-dependent Schrödinger equation (3.2):

$$\Psi(\mathbf{r}_1, \mathbf{r}_2, \mathbf{r}_3; t) = c_g(t)|g\rangle + \int d\mathbf{p} c_h(\mathbf{p}, t)|h\rangle + \int d\mathbf{p} d\mathbf{k} c_f(\mathbf{p}, \mathbf{k}, t)|f\rangle. \quad (3.4)$$

In order to use the ansatz in the Schrödinger equation we have to find derivatives of the states $|g\rangle$, $|h\rangle$, and $|f\rangle$ with respect to time, i.e. we have to differentiate the relations (3.1a-3.1c). To calculate the derivatives we first define the single-electron states so that they satisfy the following one-electron Schrödinger equations:

$$i\frac{\partial}{\partial t}|0, t\rangle = [-\frac{1}{2}\Delta + U_a(\mathbf{r})]|0, t\rangle, \quad (3.5a)$$

$$i\frac{\partial}{\partial t}|a, t\rangle = [-\frac{1}{2}\Delta + U_a(\mathbf{r})]|a, t\rangle, \quad (3.5b)$$

$$i\frac{\partial}{\partial t}|b, t\rangle = [-\frac{1}{2}\Delta + U_b(\mathbf{r})]|b, t\rangle, \quad (3.5c)$$

$$i\frac{\partial}{\partial t}|\mathbf{p}, t\rangle = [-\frac{1}{2}\Delta - z\mathcal{E}_x(t)]|\mathbf{p}, t\rangle, \quad (3.5d)$$

$$i\frac{\partial}{\partial t}|\mathbf{k}, t\rangle = [-\frac{1}{2}\Delta - z\mathcal{E}_l(t)]|\mathbf{k}, t\rangle. \quad (3.5e)$$

For (3.5a-3.5c) we can write the time dependence of the states explicitly, and the equations (3.5d-3.5e) are known to have ‘‘Volkov solutions’’:

$$|0, t\rangle = e^{-itE_0}|0\rangle, \quad (3.6a)$$

$$|a, t\rangle = e^{-itE_a}|a\rangle, \quad (3.6b)$$

$$|b, t\rangle = e^{-itE_b}|b\rangle, \quad (3.6c)$$

$$|\mathbf{p}, t\rangle = \exp[-i\Phi_x(\mathbf{p}, t)] \exp\{i[\mathbf{p} - \mathbf{A}_x(t)]\mathbf{r}\}, \quad (3.6d)$$

$$|\mathbf{k}, t\rangle = \exp[-i\Phi_l(\mathbf{k}, t)] \exp\{i[\mathbf{k} - \mathbf{A}_l(t)]\mathbf{r}\} \quad (3.6e)$$

with

$$A_{x,l}(t) = -\int_{-\infty}^t \mathcal{E}_{x,l}(t') dt' \quad (3.7)$$

and the ‘‘Volkov phases’’ defined by

$$\Phi_x(\mathbf{p}, t) = \frac{1}{2} \int_{t_0}^t [\mathbf{p} - \mathbf{A}_x(t')]^2 dt', \quad (3.8)$$

$$\Phi_l(\mathbf{k}, t) = \frac{1}{2} \int_{t_0}^t [\mathbf{k} - \mathbf{A}_l(t')]^2 dt', \quad (3.9)$$

where t_0 is an arbitrary instant of time.

With the aid of equations (3.5) the time derivatives of the three essential states (3.1a-3.1c) can be written as

$$i\frac{\partial}{\partial t}|g\rangle = \left(-\frac{1}{2}(\Delta_1 + \Delta_2 + \Delta_3) + U_a(\mathbf{r}_1) + U_a(\mathbf{r}_2) + U_b(\mathbf{r}_3) \right) |g\rangle, \quad (3.10a)$$

$$i\frac{\partial}{\partial t}|h\rangle = \left(-\frac{1}{2}(\Delta_1 + \Delta_2 + \Delta_3) + U_b(\mathbf{r}_3) \right) |h\rangle + \left[(U_a(\mathbf{r}_2) - z_1\mathcal{E}_x)|\mathbf{p}, t\rangle|a, t\rangle - (U_a(\mathbf{r}_1) - z_2\mathcal{E}_x)|a, t\rangle|\mathbf{p}, t\rangle \right] |b, t\rangle, \quad (3.10b)$$

$$i\frac{\partial}{\partial t}|f\rangle = \left(-\frac{1}{2}(\Delta_1 + \Delta_2 + \Delta_3) - z_3\mathcal{E}_l \right) |f\rangle + \left[(U_a(\mathbf{r}_2) - z_1\mathcal{E}_x)|\mathbf{p}, t\rangle|0, t\rangle - (U_a(\mathbf{r}_1) - z_2\mathcal{E}_x)|0, t\rangle|\mathbf{p}, t\rangle \right] |\mathbf{k}, t\rangle. \quad (3.10c)$$

These equations can be readily used to apply the ansatz (3.4), but we need further approximations to obtain analytical expressions for $c_g(t)$, $c_h(\mathbf{p}, t)$, and $c_f(\mathbf{p}, \mathbf{k}, t)$.

3.2.2 Equations for the probability amplitudes c_h and c_f

To begin with, let us neglect depletion of the ground state and normalise the wavefunction $\Psi(\mathbf{r}_1, \mathbf{r}_2, \mathbf{r}_3; t)$ so that

$$c_g(t) \equiv 1. \quad (3.11)$$

This is a good approximation, since the flux of XUV photons produced by the high-harmonic generation process is so small that it ionises only a small fraction of atoms. Our goal is now to find the functions $c_h(\mathbf{p}, t)$ and $c_f(\mathbf{p}, \mathbf{k}, t)$. To do this, let us to close the Schrödinger equation with proper bra-vectors. To obtain $c_h(\mathbf{p}, t)$ we consider the equation

$$\langle h' | i\frac{\partial}{\partial t} - \hat{H} | \Psi(\mathbf{r}_1, \mathbf{r}_2, \mathbf{r}_3; t) \rangle = 0, \quad (3.12)$$

where

$$\langle h' | = \langle b, t | [\langle a, t | \langle \mathbf{p}', t | - \langle \mathbf{p}', t | \langle a, t |]. \quad (3.13)$$

Using ansatz (3.4) and approximation (3.11) equation (3.12) can be written as

$$\begin{aligned} \langle h' | i \frac{\partial}{\partial t} - \hat{H} | g \rangle + i \int d\mathbf{p} \frac{\partial c_h}{\partial t} \langle h' | h \rangle + \int d\mathbf{p} c_h(\mathbf{p}, t) \langle h' | i \frac{\partial}{\partial t} - \hat{H} | h \rangle + \\ + i \int d\mathbf{p} d\mathbf{k} \frac{\partial c_f}{\partial t} \langle h' | f \rangle + \int d\mathbf{p} d\mathbf{k} c_f(\mathbf{p}, \mathbf{k}, t) \langle h' | i \frac{\partial}{\partial t} - \hat{H} | f \rangle = 0. \end{aligned} \quad (3.14)$$

Analogously, the way that should lead to an analytical expression for $c_f(\mathbf{p}, \mathbf{k}, t)$ is to consider

$$\langle f' | i \frac{\partial}{\partial t} - \hat{H} | \Psi(\mathbf{r}_1, \mathbf{r}_2, \mathbf{r}_3; t) \rangle = 0, \quad (3.15)$$

with $\langle f' | = \langle k, t | [\langle 0, t | \langle \mathbf{p}', t | - \langle \mathbf{p}', t | \langle 0, t |]$. This yields

$$\begin{aligned} \langle f' | i \frac{\partial}{\partial t} - \hat{H} | g \rangle + i \int d\mathbf{p} d\mathbf{k} \frac{\partial c_f}{\partial t} \langle f' | f \rangle + \int d\mathbf{p} c_h(\mathbf{p}, t) \langle f' | i \frac{\partial}{\partial t} - \hat{H} | h \rangle + \\ + \int d\mathbf{p} \frac{\partial c_h}{\partial t} \langle f' | h \rangle + \int d\mathbf{p} d\mathbf{k} c_f(\mathbf{p}, \mathbf{k}, t) \langle f' | i \frac{\partial}{\partial t} - \hat{H} | f \rangle = 0. \end{aligned} \quad (3.16)$$

When we expand equations (3.14) and (3.16) using the Hamiltonian (3.3) and the equations for time derivatives (3.5), we will get quite a few matrix elements. This is when additional approximations and assumptions become necessary. We shall assume that

1. all the one-electron states $|0, t\rangle$, $|a, t\rangle$, $|b, t\rangle$, $|\mathbf{p}, t\rangle$, and $|\mathbf{k}, t\rangle$ are orthogonal to each other: $\langle \alpha, t | \beta, t \rangle = 0$ if $\alpha \neq \beta$; this does not hold strictly, as the states belong to different Hamiltonians;
2. the state $|h\rangle$ is not disturbed by the XUV field: the matrix elements $\langle h | \mathcal{E}_x(t) z_1 | h \rangle$ and $\langle h | \mathcal{E}_x(t) z_2 | h \rangle$ can be neglected;
3. the XUV electrons do not feel the binding potential, which means that the matrix elements $\langle 0, t | U_a | \mathbf{p}, t \rangle$, $\langle a, t | U_a | \mathbf{p}, t \rangle$, and $\langle \mathbf{p}', t | U_a | \mathbf{p}, t \rangle$ can be neglected;
4. the first-order correction to the energy of the hole-state is small: the matrix elements $\langle h | U_{ab}(\mathbf{r}_1 - \mathbf{r}_3) | h \rangle$ and $\langle h | U_{ab}(\mathbf{r}_2 - \mathbf{r}_3) | h \rangle$ can be neglected;
5. there is no continuum-continuum scattering: the matrix elements like $\langle 0, t | \langle \mathbf{p}', t | U_{ab} | \mathbf{p}, t \rangle | a, t \rangle$ and $\langle b, t | \langle \mathbf{p}', t | U_{ab} | 0, t \rangle | \mathbf{k}, t \rangle$ can be neglected;

With these approximations and using the fact that $\langle \mathbf{p}, t | \mathbf{p}', t \rangle = \delta(\mathbf{p} - \mathbf{p}')$ we obtain from (3.14) and (3.16) the following system of equations:

$$2i \frac{d}{dt} c_h(\mathbf{p}, t) = \langle h | \left[\sum_{i=1,2} U_{ab}(\mathbf{r}_i - \mathbf{r}_3) |f\rangle c_f(\mathbf{p}, \mathbf{k}, t) - \mathcal{E}_x(t) z_i |g\rangle \right], \quad (3.17)$$

$$2i \frac{d}{dt} c_f(\mathbf{p}, \mathbf{k}, t) = \langle f | \sum_{i=1,2} U_{ab}(\mathbf{r}_i - \mathbf{r}_3) |h\rangle c_h(\mathbf{p}, t). \quad (3.18)$$

Introducing the notation

$$W_A = E_a + E_b - E_0, \quad (3.19)$$

$$M(\mathbf{p}, \mathbf{k}, t) = \frac{1}{2} \langle h | \sum_{i=1,2} U_{ab}(\mathbf{r}_i - \mathbf{r}_3) |f\rangle e^{-itW_A}, \quad (3.20)$$

$$F(\mathbf{p}, t) = \frac{1}{2} \langle h | \sum_{i=1,2} \mathcal{E}_x(t) z_i |g\rangle, \quad (3.21)$$

where W_A is the classical kinetic energy of the Auger electron, we can rewrite the system (3.17-3.18) as

$$i \frac{d}{dt} c_h(\mathbf{p}, t) = e^{itW_A} \int d\mathbf{k} M(\mathbf{p}, \mathbf{k}, t) c_f(\mathbf{p}, \mathbf{k}, t) - F(\mathbf{p}, t), \quad (3.22)$$

$$i \frac{d}{dt} c_f(\mathbf{p}, \mathbf{k}, t) = e^{-itW_A} M^*(\mathbf{p}, \mathbf{k}, t) c_h(\mathbf{p}, t). \quad (3.23)$$

Integrating (3.23) and substituting the result into Eq. (3.22) yields the following integro-differential equation:

$$\frac{d}{dt} c_h(\mathbf{p}, t) = - \int d\mathbf{k} \int_{t_0}^t dt' e^{i(t-t')W_A} M(\mathbf{p}, \mathbf{k}, t) M^*(\mathbf{p}, \mathbf{k}, t') c_h(\mathbf{p}, t') + iF(\mathbf{p}, t), \quad (3.24)$$

where the initial condition $c_f(\mathbf{p}, \mathbf{k}, t_0) \equiv 0$ is implied.

Using the orthogonality of the one-electron wavefunctions (assumption 1), the functions $M(\mathbf{p}, \mathbf{k}, t)$ and $F(\mathbf{p}, t)$ can be simplified to

$$M(\mathbf{p}, \mathbf{k}, t) = \langle b, t | \langle a, t | U_{ab} | 0, t \rangle | \mathbf{k}, t \rangle e^{-itW_A}. \quad (3.25)$$

$$F(\mathbf{p}, t) = e^{-itE_0 + i\Phi_x(\mathbf{p}, t)} \mathcal{E}_{x0}(t) (e^{i\Omega t} + e^{-i\Omega t}) d[\mathbf{p} - \mathbf{A}_x(t)], \quad (3.26)$$

where

$$d(\mathbf{p}) = \langle e^{-i\mathbf{p}\mathbf{r}} | z | 0 \rangle. \quad (3.27)$$

As we see, M in Eq. (3.25) does not depend on \mathbf{p} .

There are a few important simplifications that can be made to these equations. Let us start with Eq. (3.26). First, the \mathbf{A}_x potential can be neglected in the dipole matrix element $d[\mathbf{p} - \mathbf{A}_x(t)]$ and in the Volkov phase of the XUV pulse $\Phi_x(\mathbf{p}, t)$, because 1) XUV pulses used in the experiments (obtained as a product of high-harmonic generation) have a very small intensity and 2) the electric field of the XUV pulse oscillates very quickly, so that the potential \mathbf{A}_x defined by Eq. (3.7) is many orders of magnitude smaller than the classical momentum of the XUV electron $p_0 = \sqrt{2(\Omega + E_0)}$, which is approximately 20 eV in the experiment of Ref. [A2]. The approximate expression for the Volkov phase of the XUV pulse is then

$$\Phi_x(\mathbf{p}, t) \approx \frac{p^2}{2}t. \quad (3.28)$$

This approximation can also be regarded as neglecting continuum-continuum transitions caused by the XUV pulse, so it is consistent with approximation 5 (page 68).

Second, the rotating-wave approximation can be used, which means that one of the terms $\exp(\pm i\Omega t)$ in Eq. (3.26) can be neglected. Let us set the lowest energy of the continuum to zero, so that the energies E_0 , E_a , and E_b have negative values. Then the term that has to be neglected is $\exp(i\Omega t)$ and the simplified expression for $F(\mathbf{p}, t)$ can be written as

$$F(\mathbf{p}, t) = e^{it(p^2/2 - E_0 - \Omega)} \mathcal{E}_{x0}(t) d(\mathbf{p}). \quad (3.29)$$

The expression (3.25) for $M(\mathbf{k}, t)$ can be simplified as well. To do this we use the multipole expansion for U_{ab} :

$$U_{ab}(\mathbf{r}_1 - \mathbf{r}_3) = \frac{1}{|\mathbf{r}_1 - \mathbf{r}_3|} \approx \sum_{l=0}^{\infty} \sum_{m=-l}^l \frac{r_1^l}{r_3^{l+1}} \frac{4\pi}{2l+1} Y_{lm}^*(\Theta, \Phi) Y_{lm}(\theta, \phi), \quad (3.30)$$

where the coordinates (r_1, θ, ϕ) are the spherical coordinates of the \mathbf{r}_1 vector, the coordinates of the vector \mathbf{r}_3 being (r_3, Θ, Φ) . In the expansion (3.30) $Y_{lm}(\theta, \phi)$ are the spherical functions, the expansion implies that $r_1 < r_3$. The matrix element in

Eq. (3.25) can now be expanded as

$$\begin{aligned} \langle b, t | \langle a, t | U_{ab}(\mathbf{r}_1 - \mathbf{r}_3) | 0, t \rangle | \mathbf{k}, t \rangle = \\ \sum_{l=0}^{\infty} \sum_{m=-l}^l \frac{4\pi}{2l+1} \langle b, t | r_3^{-(l+1)} Y_{lm}^*(\Theta, \Phi) | \mathbf{k}, t \rangle \langle a, t | r^l Y_{lm}(\theta, \phi) | 0, t \rangle. \end{aligned} \quad (3.31)$$

Let us assume for simplicity that either the $|0\rangle$ or the $|a\rangle$ state has angular momentum equal zero. In this case only a single term of the expansion is different from zero, and that term can be written as

$$\langle b, t | \langle a, t | U_{ab}(\mathbf{r}_1 - \mathbf{r}_3) | 0, t \rangle | \mathbf{k}, t \rangle = \langle a, t | Q(\mathbf{r}) | 0, t \rangle \langle b, t | R(\mathbf{r}) | \mathbf{k}, t \rangle, \quad (3.32)$$

For example, the experiment in Ref. [A2] is based on the Auger transition for which the states $|0\rangle$, $|a\rangle$, and $|b\rangle$ are 3d, 4s, and 4p states, respectively. In this case only the term with $l = 2$, $m = 0$ in Eq. (3.31) is non-zero, so

$$Q = r^2 \frac{4\pi}{5} Y_{20}(\theta, \phi) = r^2 \sqrt{\frac{\pi}{5}} (1 - 3 \cos^2 \theta), \quad (3.33)$$

$$R = \frac{1}{r^3} Y_{20}^*(\Theta, \Phi) = \sqrt{\frac{5}{16\pi}} \frac{1 - 3 \cos^2 \Theta}{r^3}. \quad (3.34)$$

By extracting the time-dependency of $M(\mathbf{k}, t)$ with the aid of equations (3.6) we write

$$M(\mathbf{k}, t) = \exp[-i\Phi_l(\mathbf{k}, t)] G[\mathbf{k} - \mathbf{A}_l(t)] \quad (3.35)$$

with the definition

$$G(\mathbf{k}) = \langle a | Q | 0 \rangle \langle b | R | e^{i\mathbf{k}\mathbf{r}} \rangle. \quad (3.36)$$

Substituting (3.35) into (3.24) yields

$$\frac{d}{dt} c_h(\mathbf{p}, t) = \int_{t_0}^t dt' K(t, t') c_h(\mathbf{p}, t') + iF(\mathbf{p}, t), \quad (3.37)$$

where

$$\begin{aligned} K(t, t') = -e^{i(t-t')W_A} \int d\mathbf{k} M(\mathbf{k}, t) M^*(\mathbf{k}, t') = \\ -e^{i(t-t')W_A} \int d\mathbf{k} \exp[i\Phi_l(\mathbf{k}, t') - i\Phi_l(\mathbf{k}, t)] G[\mathbf{k} - \mathbf{A}_l(t)] G^*[\mathbf{k} - \mathbf{A}_l(t')]. \end{aligned} \quad (3.38)$$

If the laser field is weak, the t -dependence of the G matrix element can be neglected: $G[\mathbf{k} - \mathbf{A}_l(t)] \approx G[\mathbf{k}]$. Numerical simulations showed, that it is legitimate

even if the matrix element changes by 20% as the electric field oscillates between its maximal and minimal values. With this approximation (3.38) simplifies to

$$K(t, t') = -e^{i(t-t')W_A} \int d\mathbf{k} |G(\mathbf{k})|^2 \exp[i\Phi_l(\mathbf{k}, t') - i\Phi_l(\mathbf{k}, t)]. \quad (3.39)$$

3.2.3 An analytical expression for c_h

The integro-differential equation (3.37) can be approximated by a differential equation if the function $c_h(\mathbf{p}, t)$ is a slowly varying function of t :

$$\begin{aligned} \int_{t_0}^t dt' K(t, t') c_h(\mathbf{p}, t') &= \int_{t_0}^t dt' K(t, t') \sum_{n=0}^{\infty} \frac{(t' - t)^n}{n!} \frac{\partial^n}{\partial t'^n} c_h(\mathbf{p}, t) \approx \\ &= \int_{t_0}^t dt' K(t, t') c_h(\mathbf{p}, t) = c_h(\mathbf{p}, t) \int_{t_0}^t dt' K(t, t'), \end{aligned}$$

so that

$$\frac{d}{dt} c_h(\mathbf{p}, t) = c_h(\mathbf{p}, t) \int_{t_0}^t dt' K(t, t') + iF(\mathbf{p}, t). \quad (3.40)$$

In section 3.3 the validity of this approximation will be discussed using results of numerical calculations. Let us also neglect the influence of the laser field on c_h by taking $\Phi_l(\mathbf{k}, t) = k^2 t/2$. With the initial conditions

$$\begin{aligned} \lim_{t \rightarrow -\infty} c_h(\mathbf{p}, t) &= 0, \\ \lim_{t \rightarrow -\infty} c_f(\mathbf{p}, \mathbf{k}, t) &= 0 \end{aligned}$$

the solution of Eq. (3.40) has the following form:

$$c_h(\mathbf{p}, t) = i \int_{-\infty}^t dt' \exp \left[- \int_{t'}^t P(t'') dt'' \right] F(\mathbf{p}, t'), \quad \text{where} \quad (3.41)$$

$$P(t) = \int_{-\infty}^t dt' \int d\mathbf{k} |G(\mathbf{k})|^2 \exp[-i(k^2/2 - W_A)(t - t')]. \quad (3.42)$$

$$(3.43)$$

Let us calculate the integrals in P . Exchanging the integration order we write

$$\begin{aligned} P(t) &= \lim_{\delta \rightarrow +0} \int d\mathbf{k} \int_{-\infty}^t dt' |G(\mathbf{k})|^2 \exp[-i(k^2/2 - W_A)(t - t') + \delta t'] = \\ &= -i \lim_{\delta \rightarrow +0} \int_0^{\infty} dk \int_0^{2\pi} d\phi \int_0^{\pi} d\theta \frac{|G(k, \theta, \phi)|^2 \exp[\delta t]}{k^2/2 - W_A - i\delta} k^2 \sin \theta = [k^2/2 = E] = \\ &= -i \lim_{\delta \rightarrow +0} \int_0^{\infty} dE \int_0^{2\pi} d\phi \int_0^{\pi} d\theta \frac{|G(E, \theta, \phi)|^2 \rho(E) \exp[\delta t] \sin \theta}{E - W_A - i\delta}. \end{aligned}$$

Here $\rho(E) \equiv k$ is the density of states in the continuum. Introducing a new variable $\varepsilon = E - W_A$ we can write

$$P(t) = -i \lim_{\delta \rightarrow +0} \int_{-W_A}^{\infty} d\varepsilon \int_0^{2\pi} d\phi \int_0^{\pi} d\theta \frac{|G(\varepsilon + W_A, \theta, \phi)|^2 \rho(\varepsilon + W_A) e^{\delta t} \sin \theta}{\varepsilon - i\delta}. \quad (3.44)$$

This integral can be split into contribution from the pole and a principal value integral:

$$P(t) = -i \int_0^{2\pi} d\phi \int_0^{\pi} d\theta i\pi |G(W_A, \theta, \phi)|^2 \rho(W_A) \sin \theta - \\ -i V.p. \int_{-W_A}^{\infty} d\varepsilon \int_0^{2\pi} d\phi \int_0^{\pi} d\theta \frac{|G(\varepsilon + W_A, \theta, \phi)|^2 \rho(\varepsilon + W_A) \sin \theta}{\varepsilon}. \quad (3.45)$$

This is a standard approach in the theory of photoionisation and autoionisation [62]. The first term describes the decay of the autoionisation state, and the second term is responsible for the spectral shift due to the Coulomb interaction. So we can introduce the Auger decay rate

$$\frac{\Gamma}{2} = \pi \rho(W_A) \int_0^{2\pi} \int_0^{\pi} |G(W_A, \theta, \phi)|^2 \sin \theta d\theta d\phi \quad (3.46)$$

and the energy shift

$$E_s = -V.p. \int_{-W_A}^{\infty} d\varepsilon \int_0^{2\pi} d\phi \int_0^{\pi} d\theta \frac{|G(\varepsilon + W_A, \theta, \phi)|^2 \rho(\varepsilon + W_A)}{\varepsilon} \sin \theta. \quad (3.47)$$

In this notation $P(t) = \Gamma/2 + iE_s$. Substituting this expression for $P(t)$ in equation (3.41) we obtain the following closed-form expression for c_h :

$$c_h(\mathbf{p}, t) = i \int_{-\infty}^t \exp \left[- \left(\frac{\Gamma}{2} + iE_s \right) (t - t') \right] F(\mathbf{p}, t') dt'. \quad (3.48)$$

3.2.4 Analytical expressions for c_f

As soon as the $c_h(\mathbf{p}, t)$ probability amplitude is found, one can calculate the $c_f(\mathbf{p}, \mathbf{k}, t)$ amplitude by solving the differential equation (3.23). With the expression (3.35) for $M(\mathbf{p}, \mathbf{k}, t)$ and the initial condition $c_f(\mathbf{p}, \mathbf{k}, -\infty) \equiv 0$ the analytical solution of Eq. (3.23) is

$$c_f(\mathbf{p}, \mathbf{k}, t) = -i \int_{-\infty}^t dt' e^{i\Phi_l(k, t') - it' W_A} G^*[\mathbf{k} - \mathbf{A}_l(t')] c_h(\mathbf{p}, t'). \quad (3.49)$$

Neglecting the potential $\mathbf{A}_l(t)$ in $G[\mathbf{k} - \mathbf{A}_l(t)]$ just as we did it in section 3.2.3, we can simplify the equation for c_f slightly more:

$$c_f(\mathbf{p}, \mathbf{k}, t) = -iG^*(\mathbf{k}) \int_{-\infty}^t dt' e^{i\Phi_l(k, t') - it'W_A} c_h(\mathbf{p}, t'). \quad (3.50)$$

The integration can be easily performed numerically, section 3.3 is devoted to this issue. However, it is instructive to consider the cases when the integral can be evaluated analytically. In the most simple case the laser pulse is either absent or delayed from the XUV pulse so much that they practically don't overlap and, consequently, the laser pulse does not have any influence on the Auger spectrum.

No laser field

Without the laser field $\mathcal{E}_l(t) \equiv 0$ the amplitude $c_f(\mathbf{p}, \mathbf{k}, t = +\infty)$ can be evaluated using the following trick. Let us substitute $\mathcal{E}_{x0}(t)$ in Eq. (3.29) by the inverse Fourier transform of its spectrum

$$\mathcal{E}_{x0}(t) = \frac{1}{2\pi} \int_{-\infty}^{\infty} \tilde{\mathcal{E}}_{x0}(\omega) e^{-i\omega t} d\omega. \quad (3.51)$$

Substituting further the obtained expression into (3.48) yields

$$c_h(\mathbf{p}, t) = \frac{id(\mathbf{p})}{2\pi} \int_{-\infty}^t dt' \left(\exp \left[- \left(\frac{\Gamma}{2} + iE_s \right) (t - t') \right] \times \right. \\ \left. \times e^{it'(p^2/2 - E_0 - \Omega)} \int_{-\infty}^{\infty} d\omega \tilde{\mathcal{E}}_{x0}(\omega) e^{-i\omega t'} \right).$$

Exchanging the integration order and evaluating the internal integral analytically we obtain

$$c_h(\mathbf{p}, t) = \frac{id(\mathbf{p})}{2\pi} e^{-it(E_0 + \Omega - p^2/2)} \int_{-\infty}^{\infty} d\omega \frac{\tilde{\mathcal{E}}_{x0}(\omega) e^{-i\omega t}}{\Gamma/2 - i(E_0 - E_s + \Omega - p^2/2 + \omega)}. \quad (3.52)$$

In the absence of the laser field $\Phi_l = k^2 t/2$, so (3.50) can be written as

$$c_f(\mathbf{p}, \mathbf{k}, t) = \frac{d(\mathbf{p})}{2\pi} G^*(\mathbf{k}) \int_{-\infty}^t dt' e^{it'(k^2/2 - W_A - E_0 - \Omega + p^2/2)} \\ \int_{-\infty}^{\infty} d\omega \frac{\tilde{\mathcal{E}}_{x0}(\omega) e^{-i\omega t'}}{\Gamma/2 - i(E_0 - E_s + \Omega - p^2/2 + \omega)}. \quad (3.53)$$

Exchanging the integration order and taking the limit $t \rightarrow +\infty$ yields

$$c_f(\mathbf{p}, \mathbf{k}, +\infty) = \frac{d(\mathbf{p})}{2\pi} G^*(\mathbf{k}) \int_{-\infty}^{\infty} d\omega \frac{\tilde{\mathcal{E}}_{x0}(\omega)}{\Gamma/2 - i(E_0 - E_s + \Omega - p^2/2 + \omega)} \int_{-\infty}^{\infty} dt' e^{it'(k^2/2 + p^2/2 - W_A - E_0 - \Omega - \omega)}. \quad (3.54)$$

The internal integral evaluates to the delta function $2\pi\delta(k^2/2 + p^2/2 - W_A - E_0 - \Omega - \omega)$, and the final expression for the c_f amplitude in the absence of the laser field is

$$c_f(\mathbf{p}, \mathbf{k}, +\infty) = d(\mathbf{p}) G^*(\mathbf{k}) \frac{\tilde{\mathcal{E}}_{x0}(\frac{k^2+p^2}{2} - E_a - E_b - \Omega)}{\Gamma/2 - i(\frac{k^2}{2} - W_A - E_s)}. \quad (3.55)$$

This equation predicts the Lorentzian shape for the Auger spectrum with the FWHM equal to the Auger decay rate Γ . One sees that the *sum* of the electron kinetic energies $(k^2 + p^2)/2$ is distributed according to the spectral width of the XUV pulse, although in our model the Auger electron is never directly exposed to the XUV pulse. This is a purely quantum mechanical effect due to coherent quantum phases of the two particles. The argument of $\tilde{\mathcal{E}}_{x0}$ shows that the probability $|c_f(\mathbf{p}, \mathbf{k}, +\infty)|^2$ is maximal if the sum of the electron kinetic energies is close to the part of the XUV photon energy that was not used for ionisation.

Auger decay dressed by a monochromatic laser field

If the Auger decay time is very short or the laser pulse is very long, then the envelope of the laser pulse can be considered constant during the Auger decay. Let us write the potential \mathbf{A}_l , defined by Eq. (3.7), as

$$\mathbf{A}_l(t) = \mathbf{A}_0 \sin(\omega_l t + \varphi).$$

Then the Volkov phase Φ_l , defined by Eq. (3.9), can be written as

$$\frac{1}{2} \int_{t_0}^t [\mathbf{k} - \mathbf{A}_0 \sin(\omega_l t' + \varphi)]^2 dt' = \frac{k^2}{2} (t - t_0) + (\mathbf{k} \cdot \mathbf{A}_0) \frac{\cos(\omega_l t + \varphi)}{\omega_l} \Big|_{t_0}^t + \frac{A_0^2}{4} \left(t - \frac{\sin[2(\omega_l t + \varphi)]}{2\omega_l} \right) \Big|_{t_0}^t,$$

Since t_0 in the Volkov phase is arbitrary, we can choose its value so that all the terms which include t_0 vanish. Also, we can neglect the term involving A_0^2 assuming a weak laser field (in the experimental conditions of Ref. [A2] there are about

two orders of magnitude difference between the kinetic energy of Auger electrons $k^2/2$ and A_0^2). So we consider the following Volkov phase corresponding to the laser field:

$$\Phi_l(\mathbf{k}, t) = \frac{k^2}{2}t + \frac{(\mathbf{k} \cdot \mathbf{A}_0)}{\omega_l} \cos(\omega_l t + \varphi). \quad (3.56)$$

Introducing this phase into (3.50) we obtain

$$c_f(\mathbf{p}, \mathbf{k}, t) = -iG^*(\mathbf{k}) \int_{-\infty}^t dt' e^{it'(k^2/2 - W_A)} \exp\left(i \frac{(\mathbf{k} \cdot \mathbf{A}_0)}{\omega_l} \cos(\omega_l t' + \varphi)\right) c_h(\mathbf{p}, t').$$

Using the expansion

$$e^{iz \cos \varphi} = \sum_{n=-\infty}^{\infty} i^n J_n(z) e^{in\varphi}, \quad (3.57)$$

where J_n are the Bessel functions, we can write

$$c_f(\mathbf{p}, \mathbf{k}, t) = -iG^*(\mathbf{k}) \sum_{n=-\infty}^{\infty} i^n J_n\left(\frac{(\mathbf{k} \cdot \mathbf{A}_0)}{\omega_l}\right) \times \int_{-\infty}^t dt' e^{it'(k^2/2 - W_A)} e^{in(\omega_l t' + \varphi)} c_h(\mathbf{p}, t'). \quad (3.58)$$

Using Eq. (3.52) for $c_h(\mathbf{p}, t)$ and taking the limit $t \rightarrow +\infty$ we finally obtain

$$c_f(\mathbf{p}, \mathbf{k}, +\infty) = d(\mathbf{p})G^*(\mathbf{k}) \sum_{n=-\infty}^{\infty} \left\{ e^{in(\varphi + \frac{\pi}{2})} J_n\left(\frac{(\mathbf{k} \cdot \mathbf{A}_0)}{\omega_l}\right) \times \frac{\tilde{\mathcal{E}}_{x0}(n\omega_l + \frac{k^2 + p^2}{2} - E_a - E_b - \Omega)}{\Gamma/2 - i(n\omega_l + \frac{k^2}{2} - W_A - E_s)} \right\}. \quad (3.59)$$

If the Auger decay rate Γ is a few times larger than the laser frequency ω_l , then the terms of the sum correspond to sidebands in the Auger spectrum, which are separated by ω_l and have the FWHM equal to Γ .

3.3 Numerical simulations

Equation (3.59) gives a very clear picture of the Auger decay, however, quite a few approximations were made to derive it. On the one hand, some of these approximations require verification, on the other hand, Eq. (3.59) is only applicable when neither the envelope of the probe pulse nor its frequency change during the Auger decay. Pulses with an arbitrary shape and chirp can be easily dealt with

in numerical simulations, and the simulations are of big help to clarify effects of different approximations.

The quantity which is actually measurable in experiments is the energy distribution of Auger electrons (Auger spectrum), which can be expressed through the complex amplitude of the Auger state as

$$\sigma(\mathbf{k}) = \int d\mathbf{p} |c_f(\mathbf{p}, \mathbf{k}, +\infty)|^2. \quad (3.60)$$

There are three levels of approximation for the amplitude c_f , which we introduced in section 3.2. The most general expression is given by the integro-differential equation (3.37). Assuming $c_h(\mathbf{p}, t)$ to be a slowly varying function of t and neglecting the influence of the laser field on c_h we obtained Eq. (3.48). Further, assuming that the laser field oscillates with a constant amplitude and a constant frequency during the Auger decay and neglecting the terms, which depend on A_0 quadratically, we obtained Eq. (3.59). Later in this section we will compare the Auger spectra found in different approximations, but first we have to determine, which expression we are going to use for the matrix elements $G(\mathbf{k})$ and $d(\mathbf{p})$.

3.3.1 The matrix elements

The matrix elements $d(\mathbf{p})$ and $G(\mathbf{k})$ were defined by equations (3.27) and (3.36). Let us write the definitions here once again.

$$d(\mathbf{p}) = \langle e^{-i\mathbf{p}\mathbf{r}} | z | 0 \rangle,$$

$$G(\mathbf{k}) = \langle a | Q | 0 \rangle \langle b | R | e^{i\mathbf{k}\mathbf{r}} \rangle.$$

In order to calculate these elements one has to find the one-electron wavefunctions $|0\rangle$, $|a\rangle$, and $|b\rangle$ by solving the corresponding Schrödinger equations (3.5a-3.5c) with some effective binding potentials $U_a(\mathbf{r})$ and $U_b(\mathbf{r})$. In the simplest case, one can use the Coulomb potential $U(r) \sim 1/r$, for which the solutions of the Schrödinger equations are given by the hydrogen-like wavefunctions:

$$\Psi_{nlm}(r, \theta, \varphi) = R_{nl}(r) Y_{lm}(\theta, \varphi), \quad (3.61)$$

where $Y_{lm}(\theta, \varphi)$ are the spherical functions and

$$R_{nl}(r) = \frac{2a^{-3/2}}{n^2(2l+1)!} \sqrt{\frac{(n+l)!}{(n-l-1)!}} \left(\frac{2r}{na}\right)^l \times \\ \times \exp\left[-\frac{r}{na}\right] F\left(-n+l+1, 2l+2, \frac{2r}{na}\right). \quad (3.62)$$

The scaling parameter a should be chosen differently for each state so that it matches the energy of the state. Let us regard the states $|0\rangle$, $|a\rangle$, and $|b\rangle$ as the $3d$, $4s$, and $4p$ hydrogen-like states. This choice is consistent with the experiment of Drescher *et. al.* [A2].

Let us start with the dipole matrix element $d(\mathbf{p})$, which determines the probability of a transition from the $|0\rangle$ state to a continuum state described by the plane wave $e^{i\mathbf{p}\mathbf{r}}$. Taking $|0\rangle = |3d\rangle$ and using the expansion

$$e^{i\mathbf{k}\mathbf{r}} = 4\pi \sqrt{\frac{\pi}{2kr}} \sum_{l=0}^{\infty} \sum_{m=-l}^l i^l J_{l+1/2}(kr) Y_{lm}^*\left(\frac{\mathbf{k}}{k}\right) Y_{lm}\left(\frac{\mathbf{r}}{r}\right) \quad (3.63)$$

we can write

$$d_m(p, \Theta, \Phi) = 4\pi \sum_{l=0}^{\infty} \sum_{m=-l}^l \int_0^{\infty} dr r^2 \int_0^{\pi} d\theta \sin\theta \int_0^{2\pi} d\varphi \\ r \cos\theta \sqrt{\frac{\pi}{2pr}} (-i)^l J_{l+1/2}(pr) Y_{lm}(\Theta, \Phi) Y_{lm}^*(\theta, \varphi). \quad (3.64)$$

The summation becomes trivial when we notice that there are at most two terms that are different from zero (which correspond to the dipole allowed transitions), and the corresponding integrals can be evaluated analytically.

Examining Eq. (3.48) we see that the matrix element $d(\mathbf{p})$ is the only term in these equations which depends on the direction of the vector \mathbf{p} . So, calculating the Auger spectrum (3.60) the integration over the angles Θ and Φ applies only to $|d(\mathbf{p})|^2$. If the dipole matrix element depends on the magnetic quantum number m of the $|0\rangle$ -state, we have to average over all the possible values of m . So, for the element $d_m(p, \Theta, \Phi)$ introduced in Eq. (3.64) the analytical result is

$$D(p) = \int_0^{\pi} d\Theta \sin\theta \int_0^{2\pi} d\Phi \left| \frac{1}{2l+1} \sum_{m=-l}^l d_m(p, \Theta, \Phi) \right|^2 = \\ \frac{47775744 \pi^2 a_{3d}^7 p^2 (5 - 54 a_{3d}^2 p^2 + 1701 a_{3d}^4 p^4)}{(1 + 9 a_{3d}^2 p^2)^{10}}, \quad (3.65)$$

where $a_{3d} = (-2E_0)^{-1/2}$.

The analytical expression for the G matrix element can also be obtained with the aid of the expansion (3.63). Using equations (3.33) and (3.34) for Q and R one can find the following expression

$$\begin{aligned}
G(k, \theta) = & 5184 \sqrt{\frac{30}{\pi k}} \cos(\theta) a_{3d}^{7/2} \left[\arctan(4ka_{4p}) (1 + 16k^2 a_{4p}^2)^2 \right. \\
& (39(-1 + 5\cos(2\theta)) + 80k^2(-5 + 9\cos(2\theta)) a_{4p}^2) + 4ka_{4p} \left(39 - 195\cos(2\theta) + \right. \\
& \left. \left. 32k^2 a_{4p}^2 (45 - 185\cos(2\theta) + 8k^2 a_{4p}^2 (63 - 179\cos(2\theta) + 320k^2 \sin^2(\theta) a_{4p}^2)) \right) \right] \\
& a_{4s}^{11/2} (-513 a_{3d}^3 + 657 a_{3d}^2 a_{4s} - 216 a_{3d} a_{4s}^2 + 16 a_{4s}^3) / \\
& \left(k^{7/2} a_{4p}^{11/2} (1 + 16k^2 a_{4p}^2)^2 (3a_{3d} + 4a_{4s})^{10} \right), \quad (3.66)
\end{aligned}$$

where θ is the angle between the \mathbf{k} vector and the z axis. The a_{4s} and a_{4p} parameters in this equation should match the energies of the $|a\rangle$ and $|b\rangle$ states: $a_{4s} = (-2E_a)^{-1/2}$, $a_{4p} = (-2E_b)^{-1/2}$.

The functions $D(p)$ and $G(k, \theta = 0)$ are plotted in Fig. 3.2. The corresponding a parameters were calculated for the energy levels $E_0 = -70\text{eV}$ and $E_b = -15\text{eV}$. Numerical calculations showed that energy distributions of Auger electrons measured in a certain direction (for a fixed angle Θ) are rather insensitive to the exact choice of the matrix elements. This can be understood from Eqs. (3.55) and (3.59), in which the probability amplitude c_f is represented as a product of $d(\mathbf{p})G^*(\mathbf{k})$ and some function of the electron's momenta p and k . Only a limited range of values of p and k may contribute to the Auger spectrum, and that range is determined by the spectrum of the XUV pulse and the Auger decay rate. If the matrix elements $d(\mathbf{p})$ and $G(\mathbf{k})$ vary little within this range, they may only have a minor effect on Auger spectra. This justifies the simple choice of the one-electron wavefunctions that we made in the beginning of the section and neglecting the time dependence of $d[\mathbf{p} - \mathbf{A}_x(t)]$ and $G[\mathbf{k} - \mathbf{A}_l(t)]$ introduced in section 3.2.2. Nevertheless, even in this case the matrix elements are important, since they give the angular distribution of the electrons.

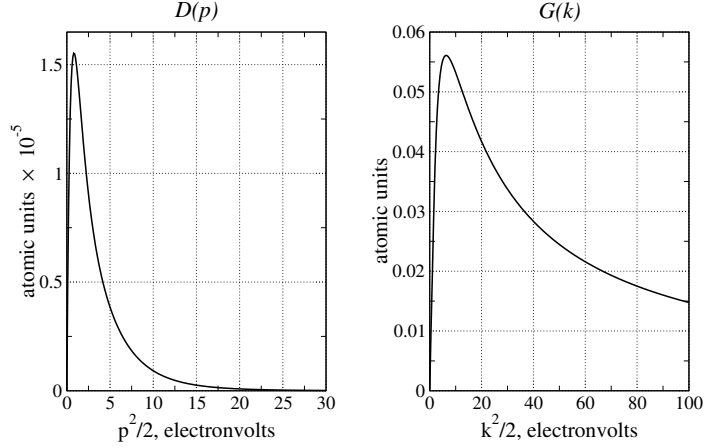


Figure 3.2: The integrated dipole matrix element $D(p)$ and the G matrix element defined by Eq. (3.65) and (3.66), respectively. The calculation is made for the parameters, when the classical energy of the XUV electron is $p^2/2 = 20$ eV, and the classical energy of the Auger electron is equal to $k^2/2 = 40$ eV.

3.3.2 Solution of the integro-differential equation for c_h

The easiest way to solve the integro-differential equation (3.37) is to transform it into a Volterra integral equation of the second kind and use the iteration method to solve the integral equation. Let us integrate Eq. (3.37) with respect to time from t_0 to t taking $c_h(\mathbf{p}, t_0) \equiv 0$ as the initial condition:

$$c_h(\mathbf{p}, t) = \int_{t_0}^t dt'' \left(\int_{t''}^t K(t', t'') dt' \right) c_h(\mathbf{p}, t'') + i \int_{t_0}^t F(\mathbf{p}, t') dt'. \quad (3.67)$$

Introducing the notation

$$\tilde{K}(t'', t) = \int_{t''}^t K(t', t'') dt' \quad (3.68)$$

and using Eq. (3.29) for $F(\mathbf{p}, t)$ we can write

$$c_h(\mathbf{p}, t) = \int_{t_0}^t \tilde{K}(t', t) c_h(\mathbf{p}, t') dt' + id(\mathbf{p}) \int_{t_0}^t e^{it'(p^2/2 - E_0 - \Omega)} \mathcal{E}_{x0}(t') dt'. \quad (3.69)$$

This is a Volterra integral equation of the second kind. A robust and straightforward way to numerically solve this equation is to use the iteration method: choose some initial approximation $c_h^{(0)}(\mathbf{p}, t)$ and repeat the iterations

$$c_h^{(n+1)}(\mathbf{p}, t) = \int_{t_0}^t \tilde{K}(t', t) c_h^{(n)}(\mathbf{p}, t') dt' + id(\mathbf{p}) \int_{t_0}^t e^{it'(p^2/2 - E_0 - \Omega)} \mathcal{E}_{x0}(t') dt'$$

until the iterations converge.

We can significantly simplify the calculations if we neglect the influence of the laser field on the hole state amplitude, that is, if we set in the kernel (3.39) the Volkov phase equal to

$$\Phi_l(\mathbf{k}, t) = \frac{k^2}{2}(t - t_0).$$

In this case the kernel $\tilde{K}(t', t)$ can be written as

$$\tilde{K}(t', t) = -2\pi i \int_0^\infty dk \left[\left(\int_0^\pi |G(k, \theta)|^2 \sin \theta d\theta \right) k^2 \frac{e^{i(t'-t)(k^2/2 - W_A)} - 1}{\frac{k^2}{2} - W_A} \right]. \quad (3.70)$$

As we see, this kernel depends only on the difference between t' and t :

$$\tilde{K} = \tilde{K}(t' - t).$$

One can easily determine the following properties of this kernel:

$$\tilde{K}(0) = 0, \quad (3.71)$$

$$\tilde{K}(-\tau) = -\tilde{K}^*(\tau), \quad (3.72)$$

$$\lim_{\tau \rightarrow \pm\infty} \text{Re}[\tilde{K}(\tau)] = \mp \frac{\Gamma}{2}. \quad (3.73)$$

The last property involves Eq. (3.46), which connects the Auger decay rate Γ with the matrix element G . Since we calculate the matrix element using the hydrogen-like wavefunctions, which is a crude model, the decay rate calculated by Eq. (3.46) may differ to a large extent from the experimentally measured rate. Besides, we would like to have Γ as a controllable parameter in order to investigate different regimes of the Auger decay. This can be achieved by simply normalising $G(k, \theta)$ so that $\text{Re}[\tilde{K}(\infty)]$ is equal to the given $\Gamma/2$. Unfortunately, there is no easy way to independently control the energy shift E_s defined by Eq. (3.47).

A typical kernel is shown in Fig. 3.3. The matrix element G was calculated with the aid of Eq. (3.66) and then normalised so that the Auger decay time became equal to 1 fs. As τ grows, $\tilde{K}(\tau)$ quickly approaches the limit $\tilde{K}(\infty)$.

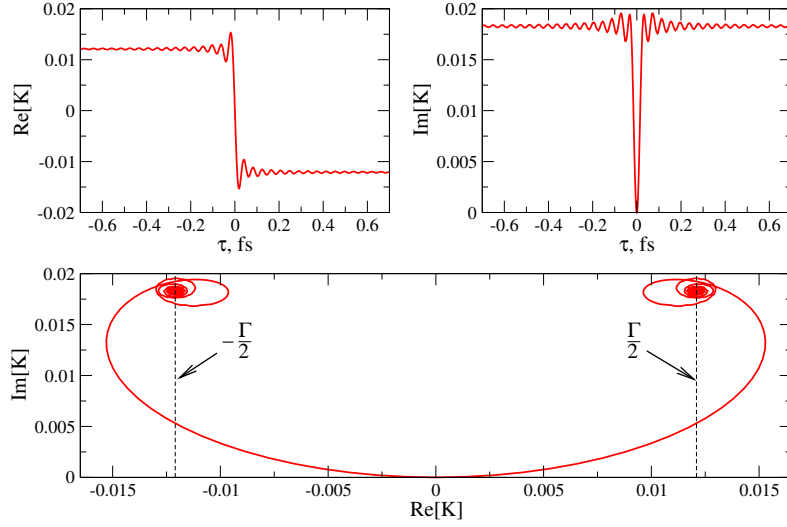


Figure 3.3: The integration kernel $\tilde{K}(\tau)$ defined by (3.70) with the matrix element G normalised to make the Auger decay rate Γ equal to 0.0242 atomic units ($1/\Gamma = 1$ fs).

3.3.3 Solution of the differential equation for c_h

The next important approximation of the theory was the transition from the integro-differential equation (3.37) to the differential equation (3.40) followed by a trivial integration leading to Eq. (3.48). Substituting Eq. (3.29) for $F(\mathbf{p}, t)$ we can write Eq. (3.48) in the following form:

$$c_h(\mathbf{p}, t) = id(\mathbf{p}) \int_{-\infty}^t \exp \left[- \left(\frac{\Gamma}{2} + iE_s \right) (t - t') \right] e^{it'(p^2/2 - E_0 - \Omega)} \mathcal{E}_{x0}(t') dt'. \quad (3.74)$$

Numerical calculation of this integral does not pose any difficulties if one employs an algorithm adapted for integration of rapidly oscillating functions. The algorithm we used is described in the appendix A.4. Once $c_h(\mathbf{p}, t)$ is calculated, numerical integration of Eq. (3.50) yields the complex amplitude of the c_f state. Again, the same integration algorithm saves a lot of computational power.

As we mentioned in section 3.3.1, the only term in the expression for c_h that depends on the direction of the vector \mathbf{p} is the dipole matrix element $d(\mathbf{p})$. Therefore, it is more convenient to extract it from (3.74) and take it into account in the last step, when calculating the Auger spectrum according to Eq. (3.60). This

allows us to perform the integration over the angles analytically. So, to simplify the calculations we modify slightly the definitions of c_h and c_f , leaving the Auger spectrum $\sigma(\mathbf{k})$ intact:

$$C_h(p, t) = \int_{t_{min}}^t \exp \left[- \left(\frac{\Gamma}{2} + iE_s \right) (t - t') \right] e^{it'(p^2/2 - E_0 - \Omega)} \mathcal{E}_{x0}(t') dt', \quad (3.75)$$

$$C_f(p, \mathbf{k}) = G^*(\mathbf{k}) \int_{t_{min}}^{\infty} e^{i\Phi_I(k, t - \tau) - itW_A} C_h(p, t) dt, \quad (3.76)$$

$$\sigma(\mathbf{k}) = \int_0^{p_{max}} D(p) |C_f(p, \mathbf{k})|^2 dp, \quad (3.77)$$

where $D(p)$ is defined by Eq. (3.65) and τ stays for the delay between the laser pulse and the XUV pulse (if $\tau > 0$, then the laser pulse follows the XUV one). The new amplitudes C_h and C_f are related to the old amplitudes c_h and c_f through

$$c_h(\mathbf{p}, t) = id(\mathbf{p})C_h(p, t), \quad (3.78)$$

$$c_f(\mathbf{p}, \mathbf{k}, +\infty) = d(\mathbf{p})C_f(p, \mathbf{k}). \quad (3.79)$$

The time t_{min} , at which the integration in (3.75-3.76) starts, must precede the moment when either the XUV pulse or the laser pulse appear. The numerical integration of Eq. (3.75) should be performed only until the moment t_1 , when the XUV pulse has gone $\mathcal{E}_{x0}(t > t_1) \equiv 0$, because the following evolution of C_h is governed by

$$C_h(p, t) = \exp \left[- \left(\frac{\Gamma}{2} + iE_s \right) (t - t_1) \right] C_h(p, t_1), \quad t > t_1. \quad (3.80)$$

Similarly, the numerical integration of Eq. (3.76) may be divided into three regions:

1. the region where the XUV pulse is active: $t_{min} \leq t \leq t_1$;
2. the region, where the intensity of the XUV pulse may be considered negligible, but the laser pulse is present: $t_1 \leq t \leq t_2$;
3. the region when both pulses have gone, and there is only the decaying hole state that can make some contribution to the Auger spectrum: $t_2 \leq t < \infty$.

The contribution from the last region can be calculated analytically and Eq. (3.76) can be rewritten in the form suitable for numerical calculations:

$$\begin{aligned}
C_f(p, \mathbf{k}) = G^*(\mathbf{k}) & \left[\int_{t_{min}}^{t_1} C_h(p, t) \exp[i\Phi_l(k, t - \tau) - itW_A] dt + \right. \\
& + C_h(p, t_1) \int_{t_1}^{t_2} \exp \left[i\Phi_l(k, t - \tau) - itW_A - \left(\frac{\Gamma}{2} + iE_s \right) (t - t_1) \right] dt + \\
& \left. + C_h(p, t_1) \frac{\exp \left[- \left(\frac{\Gamma}{2} + iE_s \right) (t_2 - t_1) + i(\Phi_l(k, t - \tau) - tW_A) \right]}{\left(\frac{\Gamma}{2} + iE_s \right) - i \left(\frac{k^2}{2} - W_A \right)} \right]. \quad (3.81)
\end{aligned}$$

3.3.4 Auger spectra

Fig. 3.4 shows several Auger spectra calculated by solving either the integro-differential equation or the differential equation for c_h . The parameters for these calculations were the following:

- the binding energy of the inner-shell electron: $E_0 = -70$ eV;
- the initial energy of the electron, which later occupies the inner-shell state emptied by an XUV photon: $E_a = -15$ eV;
- the binding energy of the Auger electron: $E_b = -15$ eV;
- the energy of the XUV photon: $\hbar\Omega = 90$ eV;
- the central wavelength of the laser pulse: $\lambda_l = 750$ nm ($\hbar\omega_l = 1.65$ eV);
- the shape of the XUV pulse: bandwidth-limited Gaussian with the FWHM of 0.5 fs;
- the laser pulse: $A(t) = A_0 \exp[-t^2/(2T^2)] \sin(\omega_l t)$ with the FWHM of 6.5 fs and the peak intensity of 5×10^{11} W/cm².

As the figure demonstrates, the approximation we made in section 3.2.3, when we transformed the integro-differential equation into a differential one, works very well: both sets of plots are very similar to each other. Here we have to note that the energy shift E_s defined by Eq. (3.47) is treated differently in the integro-differential and in the differential equations for c_h . In the differential equation it

is an independent parameter, while in the integro-differential equation it does not appear explicitly, but manifests itself by shifting Auger spectra nonetheless. In order to compare the results of the two calculations, we used for the plots (d), (e), and (f) E_s equal to -2.55 , -1.02 , and -0.1 eV, respectively.

We can distinguish three main regimes of the Auger decay (the parameters for Fig. 3.4 were chosen to illustrate the regimes):

- The regime when both, the Auger decay time and the duration of the XUV pulse are significantly shorter than the period of laser oscillations. In this regime the probe pulse only shifts and broadens the Auger spectrum depending on the delay between the pump and probe pulses. We propose to call it the “streaking” regime.
- The intermediate regime when the Auger decay occurs on the same time scale as the electromagnetic oscillations of the probe pulse.
- The side-band regime, which is observed when the Auger decay time is much longer than the oscillation period of the laser field. In this case the quantum interference leads to the appearance of sidebands separated by the photon energy ω_l .

In section 3.2.4 we derived Eq. (3.59), which allows to calculate $c_f(\mathbf{p}, \mathbf{k}, +\infty)$ analytically in the case when the envelope and the frequency of the laser pulse remain constant during the Auger decay. In Fig. 3.5 three Auger spectra are compared, which were calculated 1) with the aid of the integro-differential equation (3.37) for c_h , 2) employing the differential equation (3.48) for c_h , and 3) using Eq. (3.59). The first two approximations are the same as the ones used for Fig. 3.4. As we see, there is good qualitative agreement among the spectra, and the analytical solution gives the same result as the numerical solution of the differential equation. However, the central part of the spectrum calculated with the differential equation is more strongly modulated compared to the spectrum obtained with the aid of the integro-differential equation, which represents the most precise

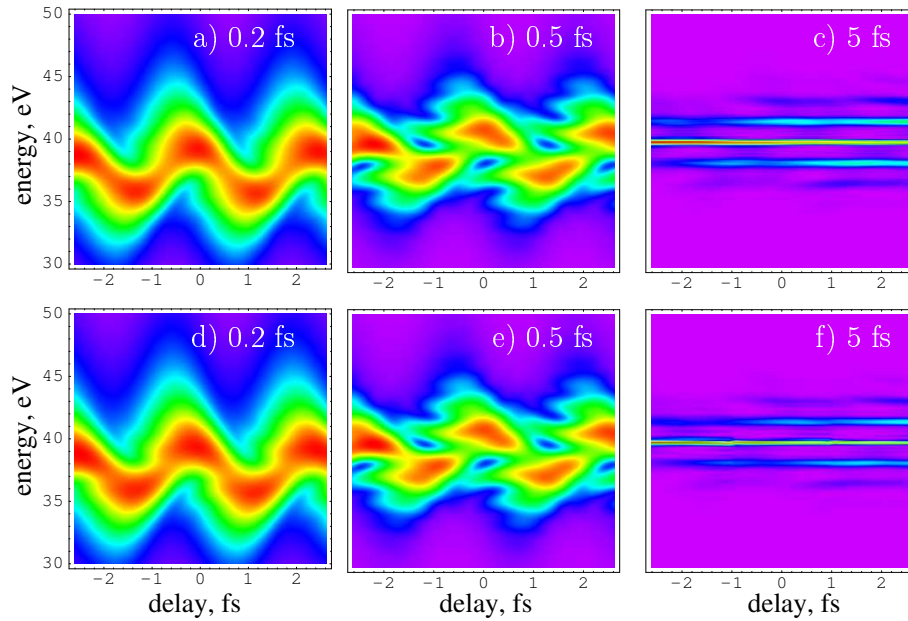


Figure 3.4: Energy distribution of Auger electrons observed in the z direction (both, the XUV pulse and the laser pulse are polarised along z). The spectral intensity is represented by the colour scheme: the intensity grows from violet to red. The probability amplitude of the hole state c_h was calculated either by solving the integral equation (3.69) [spectra (a), (b), and (c)] or by solving the differential equation (3.40) [spectra (d), (e), and (f)]. The Auger decay time for each of the spectra is written on the corresponding panels.

model that allows numerical investigation. This shows that the variation of c_h in the integral in Eq. (3.37) is not completely negligible.

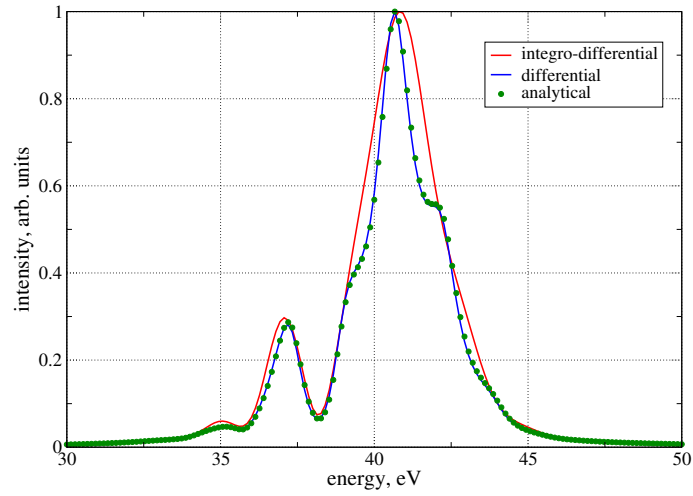


Figure 3.5: Auger spectra calculated in three different approximations: the integro-differential equation (3.37) for c_h , the differential equation (3.48) for c_h , and the analytical expression (3.59) for c_f . The Auger decay time is equal to 0.5 fs, the laser pulse is a rectangular pulse with FWHM of 20 fs, the peak of the XUV pulse coincides with the centre of the laser pulse.

Conclusions

Several aspects of generation, characterisation, and application of extremely short light pulses were discussed in this thesis. The first chapter is related to the design of chirped mirrors, which are one of the key elements in modern femtosecond laser systems and pulse compression schemes. A new efficient global optimisation algorithm was developed, which allows to significantly improve the quality of multilayer interference coatings. An emphasis was placed on the design of extremely broadband chirped mirrors. The sensitivity of multilayer coatings to random perturbations of layer thicknesses was discussed, methods to reduce the sensitivity were proposed. Based on the developed techniques, a few useful interference coatings were designed, many of which were manufactured and employed in scientific experiments: broadband (625–975 nm) chirped mirrors (Fig. 1.5 on page 22), ultrabroadband (550–1130 nm) TFI chirped mirrors (Fig. 1.8 on page 29), broadband (650–950 nm) input couplers (Fig. 1.3 on page 19), and mirrors with high positive third-order dispersion (Fig. 1.9 on page 32).

The rest of the thesis is devoted to problems of light-matter interaction. In chapter 2 an important finding is reported: it is possible to reconstruct the central part of a few-cycle laser pulse by analysing a spectrum of high-harmonic radiation generated by the pulse. In other words, it was found that there is more information about the laser pulse saved in high-harmonic spectra than it was assumed to be. The proposed method can be also regarded as a method to measure the carrier-envelope phase of laser pulses, which is more robust and has a larger range of applicability compared to the simple analysis of the cut-off region of high-harmonic spectra. Part of the results of chapter 2 was used in Ref. [A4] to

retrieve the carrier-envelope phase from high-harmonic spectra.

In the last chapter of the thesis a quantum theory of time-resolved Auger spectroscopy is presented. Based on the essential states method, closed-form expressions for probability amplitudes are derived. The model replaces the *ad hoc* model, which we introduced in Ref. [A2]. Our quantum theory can be used for more accurate interpretation of experimental data, for characterisation of sub-femtosecond extreme-ultraviolet pulses, and serve as a prototype for other theories in the field of attosecond spectroscopy.

A.1 The transfer matrix formalism

The Fresnel coefficient of reflectivity r of a thin-film multilayer structure consisting of n layers is given by

$$r = \frac{\eta_0 - Y}{\eta_0 + Y}, \text{ where} \quad (\text{A.1})$$

$$Y = C/B, \quad \begin{pmatrix} B \\ C \end{pmatrix} = \left\{ \prod_{k=1}^n M_k \right\} \begin{pmatrix} 1 \\ \eta_{n+1} \end{pmatrix}, \quad (\text{A.2})$$

$$M_k = \begin{pmatrix} \cos \delta_k & (i \sin \delta_k) / \eta_k \\ i \eta_k \sin \delta_k & \cos \delta_k \end{pmatrix}, \quad (\text{A.3})$$

$$\delta_k = \frac{2\pi N_k d_k \cos \theta_k}{\lambda}, \quad (\text{A.4})$$

$$\eta_k = \begin{cases} N_k \cos \theta_k & \text{for TE waves (s-waves),} \\ N_k / \cos \theta_k & \text{for TM waves (p-waves),} \end{cases} \quad (\text{A.5})$$

$$N_0 \sin \theta_0 = N_k \sin \theta_k \quad (\theta_0 \text{ is the angle of incidence}). \quad (\text{A.6})$$

Here d_k is the physical thickness of the k th layer, and N_k is its complex refractive index (N_0 is the index of the incidence medium and N_{n+1} is the index of the exit medium). The phase shift on reflection and the reflectance are given by $\arg(r)$ and $|r|^2$ respectively. Refractive indices N_k depend on the wavelength λ , and this determines the dispersion properties of the structure.

A.2 Numerical solution of the pulse propagation equations

Propagation of a few-cycle laser pulse and harmonic radiation generated by the pulse in a gas medium was simulated in the slowly-evolving wave approximation [67] in three dimensions of space assuming cylindrical symmetry for the transverse beam profile. Diffraction of both laser and harmonic pulses was taken into account. The equations were solved for the electric field, because the conception of pulse envelope is not useful in the case of few-cycle pulses. The equation for the laser pulse is the one derived in Ref. [68]. Written in the CGS units it has the following form:

$$\begin{aligned} \frac{\partial E_l(\rho, \xi, \tau)}{\partial \xi} = & \frac{c}{2} \nabla_{\perp}^2 \int_{-\infty}^{\tau} E_l(\rho, \xi, \tau') d\tau' - \frac{1}{2c} \int_{-\infty}^{\tau} \omega_p^2(\rho, \xi, \tau') E_l(\rho, \xi, \tau') d\tau' - \\ & \frac{2\pi W_b}{c E_l(\rho, \xi, \tau)} \frac{\partial n_e(\rho, \xi, \tau)}{\partial \tau} - \frac{1}{c} \frac{\partial}{\partial \tau} \left\{ \Delta n^{(a)}(\rho, \xi, \tau) E_l(\rho, \xi, \tau) \right\}. \end{aligned} \quad (\text{A.7})$$

The equation for the harmonic pulse in the slowly-evolving wave approximation is

$$\begin{aligned} \frac{\partial E_h(\rho, \xi, \tau)}{\partial \xi} = & -\alpha E_h(\rho, \xi, \tau) + \frac{c}{2} \nabla_{\perp}^2 \int_{-\infty}^{\tau} E_h(\rho, \xi, \tau') d\tau' - \\ & \frac{2\pi}{c} \frac{\partial}{\partial \tau} \left\{ n_a(\rho, \xi, \tau) d_h[E_l(\rho, \xi, \tau)] + \text{c.c.} \right\}. \end{aligned} \quad (\text{A.8})$$

In equations (A.7-A.8) E_l and E_h are the electric fields of laser and harmonic pulse, respectively, ρ is the distance to the beam axis, ξ and τ are the co-moving coordinates:

$$\xi = z, \quad (\text{A.9a})$$

$$\tau = t - z/c, \quad (\text{A.9b})$$

c is the vacuum speed of light, ω_p is the plasma frequency:

$$\omega_p(\rho, \xi, \tau) = \sqrt{\frac{4\pi e^2 n_e(\rho, \xi, \tau)}{m_e}}, \quad (\text{A.10})$$

W_b is the ionisation potential (equal to 21.6 eV for neon), α is the XUV absorption coefficient, d_h is the single-atom dipole response given by Eq. (2.2) n_e is the concentration of free electrons, and $\Delta n^{(a)}(\rho, \xi, \tau)$ is the contribution of neutral atoms to the refractive index of the plasma. Static-field ionisation rates $w[E_l]$ were obtained separately from quantum-mechanical calculations [54]. Using these rates the concentration of neutral atoms can be calculated as

$$n_a(\rho, \xi, \tau) = n_0 \exp\left(-\int_{-\infty}^{\tau} w[E_l(\rho, \xi, \tau')] d\tau'\right), \quad (\text{A.11})$$

where n_0 is the initial concentration of atoms (before the laser pulse appeared). The concentration of free electrons is correspondingly equal to

$$n_e(\rho, \xi, \tau) = n_0 - n_a(\rho, \xi, \tau) = n_0 \cdot \left(1 - \exp\left(-\int_{-\infty}^{\tau} w[E_l(\rho, \xi, \tau')] d\tau'\right)\right). \quad (\text{A.12})$$

The contribution of neutral atoms to the refractive index is taken to be proportional to n_a :

$$\Delta n^{(a)}(\rho, \xi, \tau) = s n_a(\rho, \xi, \tau) = s n_0 \exp\left(-\int_{-\infty}^{\tau} w[E_l(\rho, \xi, \tau')] d\tau'\right) \quad (\text{A.13})$$

with the factor s equal to $2.51 \times 10^{-24} \text{ cm}^3$ for neon.

It is convenient to solve equations (A.7-A.8) in the frequency domain. Applying the Fourier transform we obtain

$$\begin{aligned} \frac{\partial \tilde{E}_l(\rho, \xi, \omega)}{\partial \xi} &= \frac{ic}{2\omega} \frac{1}{\rho} \frac{\partial}{\partial \rho} \left(\rho \frac{\partial \tilde{E}_l(\rho, \xi, \omega)}{\partial \rho} \right) - \frac{i}{2\omega c} \mathcal{F} [\omega_p^2(\rho, \xi, \tau) E_l(\rho, \xi, \tau)] - \\ &\mathcal{F} \left[\frac{2\pi W_b}{c E_l(\rho, \xi, \tau)} \frac{\partial n_e(\rho, \xi, \tau)}{\partial \tau} \right] + \frac{i\omega}{c} \mathcal{F} [\Delta n^{(a)}(\rho, \xi, \tau) E_l(\rho, \xi, \tau)], \quad (\text{A.14}) \end{aligned}$$

$$\begin{aligned} \frac{\partial \tilde{E}_h(\rho, \xi, \omega)}{\partial \xi} &= -\alpha(\omega) \tilde{E}_h(\rho, \xi, \omega) + \frac{ic}{2\omega} \frac{1}{\rho} \frac{\partial}{\partial \rho} \left(\rho \frac{\partial \tilde{E}_h(\rho, \xi, \omega)}{\partial \rho} \right) + \\ &\frac{2\pi i \omega}{c} \mathcal{F} [n_a(\rho, \xi, \tau) d_h[E_l(\rho, \xi, \tau)] + \text{c.c.}], \quad (\text{A.15}) \end{aligned}$$

where

$$\mathcal{F}[f(\tau)] = \int_{-\infty}^{\infty} f(t) e^{i\omega t} dt, \quad (\text{A.16})$$

$$\tilde{E}_{l,h}(\rho, \xi, \omega) = \mathcal{F}[E_{l,h}(\rho, \xi, \tau)]. \quad (\text{A.17})$$

In Eq. (A.15) the absorption coefficient α is taken to be frequency-dependent, data for specific materials are available on the web-page [69].

The choice of a discretisation scheme to solve equations (A.14-A.15) is an important issue, because the diffraction terms can easily cause numerical instability. A stable scheme suitable for these equations is the Crank-Nicholson scheme [51]. Let us write the equation in a generic form. Within a single integration step different frequency components can be treated independently, so we can write the equation for a particular frequency ω :

$$\frac{\partial E(\rho, \xi)}{\partial \xi} = -\alpha E(\rho, \xi) + \frac{ic}{2\omega} \left(\frac{\partial^2 E(\rho, \xi)}{\partial \rho^2} + \frac{1}{\rho} \frac{\partial E(\rho, \xi)}{\partial \rho} \right) + f(\rho, \xi), \quad (\text{A.18})$$

where $f(\rho, \xi)$ incorporates all the terms other than linear absorption and diffraction. We adopt the following discretisation for Eq. (A.18):

$$\rho_k = h \left(k - \frac{1}{2} \right), \quad k = 1, 2, \dots, N, \quad (\text{A.19})$$

$$E_k = E(\rho_k, \xi), \quad (\text{A.20})$$

$$\tilde{E}_k = E(\rho_k, \xi + \Delta\xi), \quad (\text{A.21})$$

$$f_k = f(\rho_k, \xi), \quad (\text{A.22})$$

$$\tilde{f}_k = f(\rho_k, \xi + \Delta\xi). \quad (\text{A.23})$$

The Crank-Nicholson scheme for (A.18) can be written in the following way:

$$\begin{aligned} \frac{\tilde{E}_k - E_k}{\Delta\xi} = \frac{1}{2} \left[-\alpha E_k + \frac{ic}{2\omega} \left(\frac{E_{k+1} - 2E_k + E_{k-1}}{h^2} + \frac{1}{\rho_k} \frac{E_{k+1} - E_{k-1}}{2h} \right) + f_k \right] + \\ \frac{1}{2} \left[-\alpha \tilde{E}_k + \frac{ic}{2\omega} \left(\frac{\tilde{E}_{k+1} - 2\tilde{E}_k + \tilde{E}_{k-1}}{h^2} + \frac{1}{\rho_k} \frac{\tilde{E}_{k+1} - \tilde{E}_{k-1}}{2h} \right) + \tilde{f}_k \right]. \end{aligned} \quad (\text{A.24})$$

This is an implicit scheme. In order to find \tilde{E}_k a tridiagonal system of linear equations has to be solved, which can be written as

$$a_k \tilde{E}_{k-1} - b \tilde{E}_k + c_k \tilde{E}_{k+1} = d_k \quad (\text{A.25})$$

with

$$a_k = \left(1 - \frac{h}{2\rho_k}\right) \Delta\xi, \quad (\text{A.26a})$$

$$b = 2 \left(\Delta\xi - i \frac{2\omega h^2}{c} \left(1 + \frac{\alpha}{2} \Delta\xi\right) \right), \quad (\text{A.26b})$$

$$c_k = \left(1 + \frac{h}{2\rho_k}\right) \Delta\xi \text{ for } k < N, \quad (\text{A.26c})$$

$$c_N = 0, \quad (\text{A.26d})$$

$$d_k = - \left(E_{k+1} - 2E_k + E_{k-1} + \frac{h}{2\rho_k} (E_{k+1} - E_{k-1}) \right) \Delta\xi + i \frac{2\omega h^2}{c} \left((2 - \alpha \Delta\xi) E_k + (f_k + \tilde{f}_k) \Delta\xi \right) \text{ for } 1 < k < N, \quad (\text{A.26e})$$

$$d_1 = -2(E_2 - E_1) \Delta\xi + i \frac{2\omega h^2}{c} \left((2 - \alpha \Delta\xi) E_1 + (f_1 + \tilde{f}_1) \Delta\xi \right), \quad (\text{A.26f})$$

$$d_N = \left(2E_N - \left(1 - \frac{h}{2\rho_N}\right) E_{N-1} \right) \Delta\xi + i \frac{2\omega h^2}{c} \left((2 - \alpha \Delta\xi) E_N + (f_N + \tilde{f}_N) \Delta\xi \right). \quad (\text{A.26g})$$

The system (A.25) is diagonally dominant ($|b| > |a_k| + |c_k|$) and it can be easily solved with the sweep method.

An important issue is the \tilde{f}_k term. It cannot be found exactly when solving Eq. (A.14) for the laser field $\tilde{E}_l(\rho, \xi, \omega)$, because it depends on $\tilde{E}_l(\rho, \xi + \Delta\xi, \omega)$ in a non-linear manner. So we have to make an additional approximation. The first attempt was to neglect the variation of \tilde{E}_l during one integration step when calculating \tilde{f}_k , but such a scheme was found to be unstable. The source of the instability was identified to be the term in Eq. (A.14) responsible for the refractive index of neutral atoms:

$$\frac{i\omega}{c} \mathcal{F} \left[\Delta n^{(a)}(\rho, \xi, \tau) E_l(\rho, \xi, \tau) \right] = \frac{i\omega}{c} \mathcal{F} \left[E_l(\rho, \xi, \tau) s n_0 \exp \left(- \int_{-\infty}^{\tau} w[E_l(\rho, \xi, \tau')] d\tau' \right) \right]. \quad (\text{A.27})$$

A rigorous solution to this problem would be to use a kind of the split-step method, because this term can be properly handled in the time domain. However, there is a much simpler solution suitable for a small degree of ionisation: the contribution of

the neutral atoms to the refractive index of plasma may be considered independent of time:

$$\Delta n^{(a)}(\rho, \xi, \tau) \approx \Delta n^{(a)}(\rho, \xi, -\infty) = sn_0. \quad (\text{A.28})$$

With this approximation

$$\mathcal{F} \left[\Delta n^{(a)}(\rho, \xi, \tau) E_l(\rho, \xi, \tau) \right] = sn_0 \tilde{E}_l(\rho, \xi, \omega)$$

so that term (A.27) can be excluded from $f(\rho, \xi)$ and accounted by α in Eq. (A.18):

$$\alpha = \frac{i\omega sn_0}{c}, \quad (\text{A.29})$$

$$f_k(\omega) = -\frac{i}{2\omega c} \mathcal{F} \left[\omega_p^2(\rho_k, \xi, \tau) E_l(\rho_k, \xi, \tau) \right] - \mathcal{F} \left[\frac{2\pi W_b}{c E_l(\rho_k, \xi, \tau)} \frac{\partial n_e(\rho_k, \xi, \tau)}{\partial \tau} \right], \quad (\text{A.30})$$

$$\tilde{f}_k(\omega) = f_k(\omega). \quad (\text{A.31})$$

For the harmonic pulse the \tilde{f}_k term does not pose any problems, because it does not depend on E_h . The α term of Eq. (A.18) is simply equal to the XUV absorption coefficient $\alpha(\omega)$ introduced in Eq. (A.15), while f_k and \tilde{f}_k are defined as

$$f_k(\omega) = \frac{2\pi i \omega}{c} \mathcal{F} [n_a(\rho_k, \xi, \tau) d_h[E_l(\rho_k, \xi, \tau)] + \text{c.c.}], \quad (\text{A.32})$$

$$\tilde{f}_k(\omega) = \frac{2\pi i \omega}{c} \mathcal{F} [n_a(\rho_k, \xi + \Delta\xi, \tau) d_h[E_l(\rho_k, \xi + \Delta\xi, \tau)] + \text{c.c.}]. \quad (\text{A.33})$$

All the HHG simulations presented in the thesis were performed for neon. Typical parameters for the simulations were the following: $n_0 = 2 \times 10^{18} \div 5 \times 10^{18} \text{ cm}^{-3}$ (corresponds to the pressure $100 \div 200 \text{ mbar}$ at $T = 300 \text{ K}$), a 5-fs 200- μJ laser pulse with the central wavelength $\lambda_0 = 800 \text{ nm}$ and the beam waist of $50 \div 100 \mu\text{m}$. Such a pulse ionises less than 10% of atoms, which justifies the approximation (A.28). Simulations with different discretisation parameters showed that the discretisation errors are negligible if $\Delta\rho = h \lesssim 1 \mu\text{m}$ and $\Delta\xi \lesssim 50 \mu\text{m}$.

A.3 Optimal focusing of the laser beam for high-harmonic imaging

The information about the laser pulse contained in high-harmonic spectra can be destroyed by the phase mismatch between the laser and harmonic pulses. So, the gas pressure, the laser beam waist, the focus position, and the thickness of the gas target must be chosen such that the coherence length is maximised, keeping at the same time the effectiveness of HHG at an acceptable level. For the typical parameters listed at the end of section A.2 (short pulse, low ionisation rate) there are two major effects contributing to phase matching: the refractive index of neutral atoms and the geometrical (Gouy) phase shift of the laser pulse. Fortunately, these two effects can be made to compensate each other to a certain degree.

In the model described in section A.2 harmonics propagate with the vacuum velocity of light c , while the laser pulse is delayed by the refractive index of the plasma, which is close to the refractive index of the neutral gas as long as the degree of ionisation is small ($\lesssim 10\%$). If the propagation distance is equal to L , the delay is equal to $\Delta t = \Delta n^{(a)}L/c$. If the electric field of a laser pulse prior to propagation is $E_I(t) = A(t) \cos(\omega_0 t + \varphi_0)$, then the delayed pulse is described by $E_I(t - \Delta t) = A(t - \Delta t) \cos(\omega_0(t - \Delta t) + \varphi_0)$. Thus, the delay shifts the phase of the pulse by $\Delta\varphi_1 = -\omega_0 \Delta n^{(a)}L/c$.

The geometrical phase shift can be approximated assuming the Gaussian beam profile. The phase of a Gaussian beam is equal to

$$\omega_0 \left(t - \frac{\rho^2}{2cz(1 + (z/z_0)^2)} \right) + \arctan \frac{z}{z_0} + \varphi_0,$$

where $z_0 = \pi w_0^2/\lambda_0$ is the confocal parameter. Near the axis ($\rho = 0$) the phase is approximately equal to

$$\omega_0 t + \frac{z}{z_0} + \varphi_0,$$

where the assumption $z \ll z_0$ was used to replace the arc tangent with z/z_0 . Thus, the Gouy shift over the propagation distance L is $\Delta\varphi_2 = L/z_0$.

The maximal coherence length is reached when $\Delta\varphi_1 + \Delta\varphi_2 = 0$, what means

$$L/z_0 - \omega_0 \Delta n^{(a)} L/c = 0.$$

This yields the optimal confocal parameter

$$z_0 = \frac{c}{\omega_0 \Delta n^{(a)}}. \quad (\text{A.34})$$

The beam waist in the focus w_0 corresponding to the optimal z_0 is equal to

$$w_0 = \sqrt{\frac{\lambda_0 z_0}{\pi}} = \frac{\lambda_0}{\pi \sqrt{2 \Delta n^{(a)}}}. \quad (\text{A.35})$$

For example, for $\lambda_0 = 800$ nm, neon pressure $p = 100$ mbar, and temperature $T = 295$ K Eq. (A.35) gives the optimal beam waist $w_0 = 72$ μm .

A.4 Integration of rapidly oscillating functions

There is a very simple and elegant method to calculate integrals of rapidly oscillating functions, which is surprisingly rarely mentioned in literature. Let us consider the integral

$$I = \int_a^b f(x)e^{i\varphi(x)} dx, \quad (\text{A.36})$$

where both $f(x)$ and $\varphi(x)$ are smooth functions of x . If the function $\varphi(x)$ varies by many times 2π within the interval $[a, b]$, then the integrand makes many oscillations in the interval, even if the function $\varphi(x)$ is as simple as a linear function. Integration methods like the Simpson rule or Gaussian quadratures demand that the integration interval be divided in so many parts, that the length of each subinterval is a fraction of the integrand's period of oscillations. Dealing with rapidly oscillating functions these methods require a large number of integration steps, which means a long computational time and loss of precision due to round-off errors.

Let us divide the integration interval $[a, b]$ to such subintervals that the functions $f(x)$ and $\varphi(x)$ are almost linear within each of the subintervals. Let $[x_1, x_2]$ be one of such subintervals, then for $x_1 \leq x \leq x_2$

$$f(x) \approx f_1 + \frac{f_2 - f_1}{x_2 - x_1}(x - x_1), \quad (\text{A.37})$$

$$\varphi(x) \approx \varphi_1 + \frac{\varphi_2 - \varphi_1}{x_2 - x_1}(x - x_1), \quad (\text{A.38})$$

where $f_1 = f(x_1)$, $f_2 = f(x_2)$, $\varphi_1 = \varphi(x_1)$, $\varphi_2 = \varphi(x_2)$. The function $f(x) \exp[i\varphi(x)]$ may still make many oscillations between x_1 and x_2 , but the contribution from the interval $[x_1, x_2]$ to the integral (A.36) is with a good precision equal to

$$\int_{x_1}^{x_2} \left[f_1 + \frac{f_2 - f_1}{x_2 - x_1}(x - x_1) \right] \exp \left\{ i \left(\varphi_1 + \frac{\varphi_2 - \varphi_1}{x_2 - x_1}(x - x_1) \right) \right\} dx = e^{\frac{\varphi_1 + \varphi_2}{2}} \Delta x \left(e^{i\frac{\Delta\varphi}{2}} (\Delta f - i f_2 \Delta\varphi) - e^{-i\frac{\Delta\varphi}{2}} (\Delta f - i f_1 \Delta\varphi) \right) / (\Delta\varphi)^2, \quad (\text{A.39})$$

where $\Delta x = x_2 - x_1$, $\Delta f = f_2 - f_1$, and $\Delta\varphi = \varphi_2 - \varphi_1$. The right-hand side of this expression cannot be evaluated directly when $\Delta\varphi = 0$. Using the Taylor expansion

we can obtain an approximate expression for Eq. (A.39), which can be used for small values of $|\Delta\varphi|$:

$$\frac{f_1 + f_2}{2} + i\Delta\varphi \frac{f_2 - f_1}{8}. \quad (\text{A.40})$$

To calculate the integral (A.36) we just have to sum the contributions from all the subintervals:

$$\int_a^b f(x) \exp[i\varphi(x)] dx \approx \sum_k e^{\frac{\varphi_k + \varphi_{k+1}}{2}} \Delta x_k \cdot \begin{cases} \left(e^{i\frac{\Delta\varphi_k}{2}} (\Delta f_k - i f_{k+1} \Delta\varphi_k) - e^{-i\frac{\Delta\varphi_k}{2}} (\Delta f_k - i f_k \Delta\varphi_k) \right) / (\Delta\varphi_k)^2, & |\Delta\varphi_k| > \varepsilon; \\ \left(\frac{f_k + f_{k+1}}{2} + i\Delta\varphi_k \frac{\Delta f_k}{8} \right), & |\Delta\varphi_k| \leq \varepsilon, \end{cases} \quad (\text{A.41})$$

where

$$\Delta x_k = x_{k+1} - x_k, \quad (\text{A.42})$$

$$\Delta f_k = f_{k+1} - f_k, \quad (\text{A.43})$$

$$\Delta\varphi_k = \varphi_{k+1} - \varphi_k. \quad (\text{A.44})$$

The choice for the parameter ε depends on the machine precision: it should be small enough, so that the approximate expression (A.40) can be applied, but large enough for round-off errors in Eq. (A.39) to be negligible. Usually $\varepsilon = 10^{-3}$ is a reasonable choice.

Bibliography

- [A1] N. Kaiser, H. K. Pulker (Eds.), *Optical Interference Coatings*. Springer-Verlag Berlin Heidelberg 2003, chapter “Interference coatings for ultrafast optics”, Gabriel Tempea, Vladislav Yakovlev, Ferenc Krausz, p. 393-422.
- [A2] M. Drescher, M. Hentschel, R. Kienberger, M. Uiberacker, V. Yakovlev, A. Scrinzi, Th. Westerwalbesloh, U. Kleineberg, U. Heinzmann, and F. Krausz. Time-resolved atomic inner-shell spectroscopy. *Nature (London)*, 419:803, 2002.
- [A3] G. Tempea, V. Yakovlev, B. Bacovic, and F. Krausz. Tilted-front-interface chirped mirrors. *J. Opt. Soc. Am. B*, 18:1747–1750, 2001.
- [A4] A. Baltuška, Th. Udem, M. Uiberacker, M. Hentschel, Ch. Gohle, R. Holzwarth, V. S. Yakovlev, A. Scrinzi, T. W. Hänsch, and F. Krausz. Attosecond control of electronic processes by intense light fields. *Nature (London)*, 421:611–615, 2003.
- [A5] Vladislav Yakovlev, Gabriel Tempea. Optimization of chirped mirrors. *Applied Optics-LP*, 41:6514–20, 2002.
- [A6] V. S. Yakovlev, P. Dombi, G. Tempea, C. Lemell, J. Burgdörfer, T. Udem, A. Apolonski. Phase-stabilized 4-fs pulses at the full oscillator repetition rate for a photoemission experiment. *Applied Physics B*, 76:329–332, 2003.

- [A7] G. Tempea, V. Yakovlev, Ferenc Krausz, Kárpát Ferencz. Novel thin-film interference components for ultrafast optics. *Optical Interference Coatings*, July 15-20, 2001, ThC1-1.
- [A8] G. Tempea, A. Apolonskii, V. Yakovlev, F. Krausz. Stabilizing the carrier-envelope phase of few-cycle pulses with sub-cycle precision: Optical waveform synthesis. *OSA Annual Meeting and Exhibit 2001*, October 14-18, ThP2.
- [A9] G. Tempea, A. Apolonskii, V. Yakovlev, A. Poppe, F. Krausz, R. Holzwarth, T. W. Hänsch. Towards strong-field interactions with phase-controlled few-cycle light. *Applications of High Field and Short Wavelength Sources IX*, October 21-24, 2001, MB1.
- [A10] V. Yakovlev, A. Apolonski, G. Tempea, F. Krausz. 4-fs pulses at megahertz repetition rate: approaching the single-cycle regime. *International Quantum Electronics Conference*, June 22-27, 2002 (Moscow), JsuB2.
- [A11] Vladislav Yakovlev and Armin Scrinzi. High harmonic imaging of few-cycle laser pulses. *Ultrafast Optics IV*, June 29–July 3, 2003 (Vienna), Mo2.
- [A12] Olga Smirnova, Vladislav Yakovlev, and Armin Scrinzi. Quantum theory of the time-resolved Auger measurement. *Ultrafast Optics IV*, June 29–July 3, 2003 (Vienna), Tu3 (poster).
- [1] A. E. Kaplan. Subfemtosecond pulses in mode-locked 2π solitons of the cascade stimulated raman scattering. *Phys. Rev. Lett.*, 73:1243–1246, 1994.
- [2] G. Farkas and G. Tóth. Proposal for attosecond light pulse generation using laser induced multiple-harmonic conversion processes in rare gases. *Physics Letters A*, 168:447–450, 1992.

- [3] Philippe Antoine, Anne L'Huillier, and Maciej Lewenstein. Attosecond pulse trains using high-order harmonics. *Phys. Rev. Lett.*, 77:1234, 1996.
- [4] M. Hentschel, R. Kienberger, C. Spielmann, G. A. Reider, N. Milosevic, T. Brabec, P. Corkum, U. Heinzmann, M. Drescher, and F. Krausz. Attosecond metrology. *Nature (London)*, 414:509, 2001.
- [5] R. Szipőcs, K. Ferencz, Ch. Spielmann, and F. Krausz. Chirped multi-layer coatings for broadband dispersion control in femtosecond lasers. *Opt. Lett.*, 19:201–203, 1994.
- [6] A. Rundquist, C. Durfee, Z. Chang, G. Taft, E. Zeek, S. Backus, M. M. Murnane, H. C. Kapteyn, I. Christov, and V. Stoev. Ultrafast laser and amplifier sources. *Appl. Phys. B*, 65:161–174, 1997.
- [7] D. H. Sutter, I. D. Jung, F. X. Kärtner, N. Matuschek, F. Morier-Genoud, V. Schreuer, M. Tilsch, T. Tschudi, and U. Keller. Self-starting 6.5-fs pulses from a Ti:Sapphire laser using a SESAM and double-chirped mirrors. *IEEE J. Select. Topics in Quantum Electronics.*, 4:169–178, 1998.
- [8] U. Morgner, F. X. Kärtner, S. H. Cho, Y. Chen, H. A. Haus, J. G. Fujimoto, E. P. Ippen, V. Scheuer, G. Angelow, and T. Tschudi. Sub-two-cycle pulses from a Kerr-lens mode-locked Ti:sapphire laser. *Opt. Lett.*, 24:411–413, 1999.
- [9] R. Ell, U. Morgner, F. X. Kärtner, J. G. Fujimoto, E. P. Ippen, V. Scheuer, G. Angelow, T. Tschudi, M. J. Lederer, A. Boiko, and B. Luther-Davies. Generation of 5-fs pulses and octave-spanning spectra directly from a Ti:sapphire laser. *Opt. Lett.*, 26:373–375, 2001.
- [10] M. Nisoli, S. Stagira, S. de Silvestri, O. Svelto, S. Sartania, Z. Cheng, G. Tempea, Ch. Spielmann, and F. Krausz. Toward a terawatt-scale sub-10-fs laser technology. *IEEE J. Select. Topics in Quantum Electronics*, 4:414–420, 1998.

- [11] J. K. Ranka, R. S. Windeler, and A. J. Stentz. Visible continuum generation in air-silica microstructure optical fibers with anomalous dispersion at 800 nm. *Opt. Lett.*, 25:25–27, 2000.
- [12] L. Xu, W. M. Kimmel, P. O’Shea, R. Trebino, J. K. Ranka, R. S. Windeler, and A. J. Stentz. Measuring the intensity and phase of ultrabroadband continuum. In Elsässer et al. [70], pages 129–131. Proceedings of the 12th International Conference, Charleston, SC, USA.
- [13] Z. Cheng, G. Tempea, T. Brabec, K. Ferencz, Ch. Spielmann, and F. Krausz. Generation of intense diffraction-limited white light and 4-fs pulses. pages 8–10. Springer-Verlag, Berlin, July 12-17 1998. Proceedings of the 11th International Conference, Garmisch-Partenkirchen, Germany.
- [14] A. Baltuška, Z. Wei, M. S. Pshenichnikov, D. A. Wiersma, and Robert Szipőcs. All-solid-state cavity-dumped sub-5-fs laser. *Appl. Phys. B*, 65:175–188, 1997.
- [15] A. Apolonski, A. Poppe, G. Tempea, Ch. Spielmann, Th. Udem, R. Holzwarth, T. W. Hänsch, and F. Krausz. Controlling the phase evolution of few-cycle light pulses. *Phys. Rev. Lett.*, 85:740–743, 2000.
- [16] F. X. Kärtner, N. Matuscheck, T. Tschibili, U. Keller, H. A. Haus, C. Heine, R. Morf, V. Scheuer, M. Tilsch, and T. Tschudi. Design and fabrication of double-chirped mirrors. *Opt. Lett.*, 22:831–833, 1997.
- [17] R. Szipőcs and A. Kőházi-Kis. Theory and design of chirped dielectric laser mirrors. *Appl. Phys. B*, 65:115–135, 1997.
- [18] G. Tempea, F. Krausz, Ch. Spielmann, and K. Ferencz. Dispersion control over 150 THz with chirped dielectric mirrors. *IEEE J. Select. Topics in Quantum Electronics*, 4:193–196, 1998.

- [19] Gabriel Tempea. *Generation and Applications of Few-Cycle Laser Pulses*. PhD thesis, Vienna University of Technology, Gusshausstr. 27/387, 1040 Wien, November 1999.
- [20] N. Matuschek, F. X. Kärtner, and U. Keller. Theory of double-chirped mirrors. *IEEE J. of Select. Topics in Quantum Electron.*, 4:197–208, 1998.
- [21] N. Matuschek, F. X. Kärtner, and U. Keller. Analytical design of double-chirped mirrors with custom-tailored dispersion characteristics. *IEEE J. Quantum Electron.*, 35:129–137, 1999.
- [22] N. Matuschek, F. X. Kärtner, and U. Keller. Exact coupled-mode theories for multilayer interference coatings with arbitrary strong index modulations. *IEEE J. Quantum Electron.*, 33:295–302, 1997.
- [23] G. Tempea and F. Krausz. Dispersion management over one octave with tilted-front-interface chirped mirrors. In *The Twelfth International Conference on Ultrafast Phenomena*, pages 106–108, Charleston, South Carolina, USA, July 9-13 2000. paper MF5.
- [24] L. Gallmann, N. Matuschek, D. H. Sutter, V. Scheuer, G. Angelow, T. Tschudi, G. Steinmeyer, and U. Keller. Smooth dispersion compensation: novel chirped mirrors with suppressed dispersion oscillations. In Elsässer et al. [70], pages 62–64. Proceedings of the 12th International Conference, Charleston, SC, USA.
- [25] N. Matuschek, L. Gallmann, D. H. Sutter, G. Steinmeyer, and U. Keller. Back-side-coated chirped mirrors with ultra-smooth broadband dispersion characteristics. *Appl. Phys. B*, 71:509–522, 2000.
- [26] T. Boudet, P. Chaton, L. Herault, G. Gonon, L. Jouanet, and P. Keller. Thin-film designs by simulated annealing. *Appl. Opt.*, 35:6219–6226, 1996.

- [27] J. A. Dobrowolski and R. A. Kemp. Refinement of optical multilayer systems with different optimization procedures. *Appl. Opt.*, 29:2876–2893, 1990.
- [28] E. Michielssen, S. Ranjithan, and R. Mittra. Optimal multilayer filter design using real coded genetic algorithms. *IEE Proceedings J*, 139:413–420, 1992.
- [29] N. J. Radcliffe and P. D. Surry. Formal memetic algorithms. In T. Fogarty, editor, *Evolutionary computing: AISB Workshop*, pages 1–14. Springer-Verlag, 1994.
- [30] Memetic algorithms’ home page.
http://www.denssis.fee.unicamp.br/~moscato/memetic_home.html
 or http://www.ing.unlp.edu.ar/cetad/mos/memetic_home.html
- [31] H. A. Macleod. *Thin-Film Optical Filters*, chapter 2.4, pages 40–41. Institute of Physics Publishing, Bristol, UK, third edition, 2001.
- [32] R. Szipőcs, A. Kőházi-Kis, S. Lakó, P. Apai, A. P. Kovács, G. DeBell, L. Mott, and A. W. Louderback. Negative dispersion mirrors for dispersion control in femtosecond lasers: chirped dielectric mirrors and multi-cavity gires-tournois interferometers. *Appl. Phys. B*, 70:51–57, 2000.
- [33] F. X. Kärtner, U. Morgner, R. Ell, T. Schibli, J. G. Fujimoto, E. P. Ippen, V. Scheuer, G. Angelow, and T. Tschudi. Ultrabroadband double-chirped mirror pairs for generation of octave spectra. *J. Opt. Soc. Am. B*, 18:882–885, 2001.
- [34] TFCalc™, thin film design software for windows. Version 3.0, <http://www.sspectra.com>.
- [35] Yu. Ermoliev and R. J-B Wets, editors. *Numerical techniques for stochastic optimization*. Springer-Verlag, 1988.

- [36] M. A. Vorontsov, G. W. Carhart, M. Cohen, and G. Cauwenberghs. Adaptive optics based on analog parallel stochastic optimization: analysis and experimental demonstration. *J. Opt. Soc. Am. A*, 17:1440–1453, 2000.
- [37] James C. Spall. Multivariate stochastic approximation using a simultaneous perturbation gradient approximation. *IEEE Trans. on Automatic Control*, 37:332–341, 1992.
- [38] L. Xu, Ch. Spielmann, A. Poppe, T. Brabec, F. Krausz, and T. W. Hänsch. Route to phase control of ultrashort light pulses. *Opt. Lett.*, 21:2008–2010, 1996.
- [39] F. Krausz, T. Brabec, T. Schnürer, and C. Spielmann. Extreme nonlinear optics: Exploring matter to a few periods of light. *Opt. Photon. News*, 9:46–51, 1998.
- [40] A. de Bohan, L. P. Antoine, D. B. Milosevic, and B. Piraux. Phase-dependent harmonic emission with ultrashort laser pulses. *Phys. Rev. Lett.*, 81:1837, 1998.
- [41] E. Cormier and P. Lambropoulos. Effect of the initial phase of the field in ionization by ultrashort laser pulses. *Eur. Phys. J. D*, 2:15–20, 1998.
- [42] G. Tempea, M. Geissler, and T. Brabec. Phase sensitivity of high-order harmonic generation with few-cycle laser pulses. *J. Opt. Soc. Am. B*, 16:669–73, 1999.
- [43] P. Dietrich, F. Krausz, and P.-B. Corkum. Determining the absolute carrier phase of a few-cycle laser pulse. *Opt. Lett.*, 25:16–18, 2000.
- [44] G. G. Paulus, F. Grasbon, H. Walther, P. Villorosi, M. Nisoli, S. Stagira, E. Priori, and S. de Silvestri. Absolute-phase phenomena in photoionization with few-cycle laser pulses. *Nature (London)*, 414:182, 2001.

- [45] A. L’Huillier, K. J. Schafer, and K. C. Kulander. High-order harmonic generation in xenon at 1064 nm: The role of phase matching. *Phys. Rev. Lett.*, 66:2200–2203, 1991.
- [46] J. L. Krause, K. J. Schafer, and K. C. Kulander. High-order harmonic generation from atoms and ions in the high intensity regime. *Phys. Rev. Lett.*, 68:3535–3538, 1992.
- [47] M. Lewenstein, P. Balcou, M. Y. Ivanov, A. L’Huillier, and P. B. Corkum. Theory of high-harmonic generation by low-frequency laser fields. *Phys. Rev. A*, 49:2117, 1994.
- [48] C. Kan, N. H. Burnett, C. E. Capjack, and R. Rankin. Coherent XUV generation from gases ionized by several cycle optical pulses. *Phys. Rev. Lett.*, 79:2971–2974, 1997.
- [49] Pascal Salières, Philippe Antoine, Armelle de Bohan, and Maciej Lewenstein. Temporal and spectral tailoring of high-order harmonics. *Phys. Rev. Lett.*, 81:5544–5547, 1998.
- [50] G. Tempea and T. Brabec. Optimization of high-harmonic generation. *Appl. Phys. B*, 70:S197–S202, 2000.
- [51] E. Priori, G. Cerullo, M. Nisoli, S. Stagira, S. De-Silvestri, P. Villoresi, L. Poletto, P. Ceccherini, C. Altucci, R. Bruzzese, and C. de Lisio. Nonadiabatic three-dimensional model of high-order harmonic generation in the few-optical-cycle regime. *Phys. Rev. A*, 61:063801, 2000.
- [52] G. Tempea, Michael Geissler, Matthias Schnürer, and T. Brabec. Self-phase-matched high harmonic generation. *Phys. Rev. Lett.*, 84:4329–4332, 2000.
- [53] N. Milosevic, A. Scrinzi, and T. Brabec. Numerical characterization of high harmonic attosecond pulses. *Phys. Rev. Lett.*, 88:093905, 2002.

- [54] A. Scrinzi. Ionization of multielectron atoms by strong static electric fields. *Phys. Rev. A*, 61:041402(R), 2000.
- [55] Nenad Milosevic. *Attosecond Physics*. PhD thesis, Vienna University of Technology, Gusshausstr. 27/387, 1040 Wien, Juni 2003.
- [56] A. Scrinzi and B. Piraux. Two-electron atoms in short intense laser pulses. *Phys. Rev. A*, 58:1310, 1998.
- [57] F. Krausz and T. Brabec. Intense few-cycle laser fields: frontiers of non-linear optics. *Rev. Mod. Phys.*, 72:545, 2000.
- [58] M. B. Gaarde, F. Salin, E. Constant, Ph. Balcou, K. J. Schafer, K. C. Kulander, and A. L’Huillier. Spatiotemporal separation of high harmonic radiation into two quantum path components. *Phys. Rev. A*, 59:1367–1373, 1999.
- [59] Pascal Salières, Anne L’Huillier, and Maciej Lewenstein. Coherence control of high-order harmonics. *Phys. Rev. Lett.*, 74:3776, 1995.
- [60] R. Kienberger, M. Hentschel, M. Uiberacker, Ch. Spielmann, M. Kitzler, A. Scrinzi, M. Wieland, Th. Westerwalbesloh, U. Kleineberg, U. Heinzmann, M. Drescher, and F. Krausz. Steering attosecond electron wave packets with light. *Science*, 297:1144, 2002.
- [61] T. Aberg. Unified theory of auger electron emission. *Physica Scripta*, T41, 1992.
- [62] M. V. Fedorov and A. E. Kazakov. Resonances and saturation in multiphoton bound-free transitions. *Progr. in Quant. Electr.*, 13:1–106, 1989.
- [63] P. Lambropoulos and P. Zoller. Autoionizing states in strong laser fields. *Phys. Rev. A*, 24:379, 1981.
- [64] J. Itatani, F. Quéré, G. L. Yudin, M. Yu. Ivanov, F. Krausz, and P. B. Corkum. Attosecond streak camera. *Phys. Rev. Lett.*, 88:173903, 2002.

- [65] M. Kitzler, N. Milosevic, A. Scrinzi, F. Krausz, and T. Brabec. Quantum theory of attosecond XUV pulse measurement by laser dressed photoionization. *Phys. Rev. Lett.*, 88:173904, 2002.
- [66] Mikhail V. Fedorov. *Atomic and Free Electrons in a Strong Light Field*, chapter 7.3. The model of essential states, pages 332–343. World Scientific Publishing Co. Pte. Ltd., 1997.
- [67] T. Brabec and F. Krausz. Nonlinear optical pulse propagation in the single-cycle regime. *Phys. Rev. Lett.*, 78:3282–3285, 1997.
- [68] M. Geissler, G. Tempea, A. Scrinzi, M. Schnürer, and F. Krausz. Light propagation in field-ionizing media: Extreme nonlinear optics. *Phys. Rev. Lett.*, 83:2930, 1999.
- [69] Center for X-ray optics. materials sciences division, E. O. Lawrence Berkeley national lab. <http://cindy.lbl.gov>
- [70] T. Elsässer, S. Mukamel, M. M. Murnane, and N. F. Scherer, editors. *Ultrafast Phenomena XII*. Springer-Verlag, Berlin, July 9-13 2000. Proceedings of the 12th International Conference, Charleston, SC, USA.

Acknowledgements

The investigations presented in this thesis appeared as a result of close collaboration with my colleagues, whose help and contribution I would like to acknowledge. I am grateful to Alexander Apolonski for his constant support. The research on chirped mirrors was done with invaluable help of Gabriel Tempea. Many important ideas appeared in discussions with Armin Scrinzi. A crucial role in the development of the Auger theory was played by Olga Smirnova, where my own contribution was mainly in verifying the numerous approximations of the theory, developing computer codes, performing and analysing numerical simulations. Last, but not least, I acknowledge the support and guidance of Prof. Ferenc Krausz.

Curriculum Vitae

Vladislav Sergeevich Yakovlev

Personal Data

date of birth: 2.5.1977

place of birth: Kaltan, Kemerovskaja Oblast, USSR

nationality: Russian

Education

- | | |
|-----------|--|
| 1993-1997 | bachelor study at the Novosibirsk State University, Russia |
| 1997-1999 | master study at the Novosibirsk State University, Russia |
| 2000-2001 | invited researcher at the Vienna University of Technology in the
Institute of Photonics |
| 2001-2003 | Ph. D. student at the Vienna University of Technology |

Research Interests

Theoretical investigations in nonlinear light-matter interactions, strong-field physics, computational methods, optimisation algorithms.

Publications

5 reviewed publications in scientific journals, 6 conference contributions, a co-author of one book chapter